JSCSEN 86(5)445–545(2021)

ISSN 1820-7421(Online)

Journal of the Serbian Chemical Society

Electronic version

VOLUME 86

No 5

BELGRADE 2021

Available on line at

www.shd.org.rs/JSCS/

The full search of JSCS is available through

DOAJ DIRECTORY OF OPEN ACCESS JOURNALS

www.doaj.org

Journal of the Serbian Chemical Society
JSCS-info@shd.org.rs • www.shd.org.rs/JSCS

J. Serb. Chem. Soc. Vol. 86, No. 5 (2021)

CONTENTS*

Published by the Serbian Chemical Society
Karnegijeva 4/III, P.O. Box 36, 11120 Belgrade, Serbia
Printed by the Faculty of Technology and Metallurgy
Karnegijeva 4, P.O. Box 35-03, 11120 Belgrade, Serbia

* For colored figures in this issue please see electronic version at the Journal Home Page: http://www.shd.org.rs/JSCS/

Journal of the Serbian Chemical Society
JSCS-info@shd.org.rs • www.shd.org.rs/JSCS
J. Serb. Chem. Soc. 86 (5) 445–457 (2021)
JSCS–5433
Survey

SURVEY

Chemical applicability of Sombor indices

IZUDIN REDŽEPOVIĆ*

Department of Chemistry, Faculty of Science, University of Kragujevac, P. O. Box 60, 34000 Kragujevac, Serbia

(Received 15 December 2020, revised 10 January, accepted 30 January 2021)

Abstract: Recently, a novel class of degree-based topological molecular descriptors was proposed, the so-called Sombor indices. Within this study, the predictive and discriminative potentials of the Sombor index, the reduced Sombor index, and the average Sombor index were examined. All three topological molecular descriptors showed good predictive potential. The statistical data indicate that the reduced Sombor index preforms with a slightly better predictive potential. An external validation confirmed this finding. It was found that these degree-based indices exert modest discriminative potential, when tested on a large group of isomers.

Keywords: graph invariants; molecular descriptors; degree of a vertex; physicochemical properties; predictive models; discriminative potential.

INTRODUCTION

A proper quantification of a molecule, more precisely its structure, may be accomplished by using molecular descriptors.[1,2] These quantities are derived from molecular structure, and they have found various applications in chemistry.[3,4] Their most important use is in QSPR/QSAR modeling[5–8] and in virtual screening.[9,10] The complexity of the obtained chemical information varies with the computational algorithm of the chosen molecular descriptor. Namely, the more detailed description of a molecule is obtained, the more computing resources have to be invested. On the other hand, a vague structural depiction is often computationally very efficient. Thus, the selection of an adequate molecular descriptor depends on the chemical problem on which it will be applied.

Encoding information on molecular structure through the utilization of topological molecular descriptors represents an efficient technique. Due to the low computational cost and quite simple identification with the structural details, the number of these molecular descriptors is huge. Topological molecular descriptors

* E-mail: izudin.redzepovic@pmf.kg.ac.rs
https://doi.org/10.2298/JSC201215006R

are mathematical values calculated from a graph representation of a molecule.[11–13] Therefore, they are also called graph invariants and have proved to be useful in chemistry.[14–19] Topological molecular descriptors were also found to be valuable in drug discovery. Namely, the advantages of graph invariants arises from the fact that receptor structure or mechanism of action of drugs is not necessary for QSAR development, also the conformation and alignment problems related with 3D QSAR (as in CoMFA applications) are completely avoided.[20] A vertex set, and edge set of a graph G, denoted by $V(G)$ and $E(G)$, corresponds to the non-hydrogen atoms and bonds of a molecule, respectively. Graph invariants can be computed from the molecular graph by using various algorithms. Thus, depending on which parameters are used in their definitions, degree-, distance-, and eigenvalue-based graph invariants can be differentiated.

The very first degree-based graph invariant is the first Zagreb index (Zg_1), which was introduced in 1972.[21] The first Zagreb index was defined as follows:

$$Zg_1(G) = \sum_{v \in V(G)} \deg(v)^2 \tag{1}$$

where deg(v) is degree, *i.e.*, number of first neighbors, of the vertex v. This quantity was developed during the investigation of dependence of π-electron energy on molecular structure. Since its introduction, this index has gained a lot of attention, especially among mathematicians.[22–26] It is interesting to point out that Zg_1 can also be calculated in this way:[27]

$$Zg_1(G) = \sum_{e_{i,j} \in E(G)} \left(\deg(v_i) + \deg(v_j)\right) \tag{2}$$

Recently, the author of the paper "Geometric approach to degree-based topological indices: Sombor indices"[28] being inspired by Euclidean metric, proposed novel graph invariants based on degree of a vertex. Namely, Sombor index (SO), reduced Sombor index (SO_{red}), and average Sombor index (SO_{avg}) were introduced. These quantities are defined as follows:

$$SO(G) = \sum_{e_{i,j} \in E(G)} \sqrt{\deg(v_i)^2 + \deg(v_j)^2} \tag{3}$$

$$SO_{\text{red}}(G) = \sum_{e_{i,j} \in E(G)} \sqrt{(\deg(v_i) - 1)^2 + (\deg(v_j) - 1)^2} \tag{4}$$

$$SO_{\text{avg}}(G) = \sum_{e_{i,j} \in E(G)} \sqrt{\left(\deg(v_i) - \frac{2m}{n}\right)^2 + \left(\deg(v_j) - \frac{2m}{n}\right)^2} \tag{5}$$

where m in Eq. (5) is the number of edges, while n denotes the number of vertices. The summation in the above equations goes over all edges. This novel class of indices was developed as the geometric representation of degree-based graph invariants.

As previously mentioned, the number of topological molecular descriptors is huge and is still increasing. Many of them are introduced as modifications of previously well-known indices and some of them have never been applied on solving chemical problems. Therefore, to filter a useful molecular descriptor from a pool of others, a list of desirable properties was compiled.[29] Within several listed features, sufficient predictive potential of physico-chemical properties of molecules and a low degeneracy level are among the most important ones. Since Sombor indices have recently been introduced and there is not much information about them, it is interesting to test their potential chemical applicability. More precisely, within this study the predictive and discriminative potentials of Sombor indices are analyzed.

COMPUTATIONAL METHODOLOGY

Construction of predictive models

In order to investigate predictive capability of Sombor indices, models for predicting the entropy ($S°$) and enthalpy change of vaporization ($\Delta H°_{vap}$) of compounds were developed. The models were constructed using an octane set of isomers and they are based on multiple linear regression. With the utilization of isomers, the influence of molecular size on a predictive model is eliminated. The experimental data used for the construction of the models were collected from www.moleculardescriptors.eu[30] and they are presented in Table I. The

TABLE I. The experimental data used for the development of the linear models

Molecule	$S°$ / J mol^{-1} K^{-1}	$\Delta H°_{vap}$ / kJ mol^{-1}
N-Octane	467.23	41.48
2-Methylheptane	459.57	39.68
3-Methylheptane	465.51	39.84
4-Methylheptane	457.39	39.68
3-Ethylhexane	457.86	39.65
2,2-Dimethylhexane	432.71	37.30
2,3-Dimethylhexane	451.96	38.79
2,4-Dimethylhexane	447.60	37.78
2,5-Dimethylhexane	442.33	37.87
3,3-Dimethylhexane	438.23	37.54
3,4-Dimethylhexane	445.97	38.98
2-Methyl-3-ethylpentane	443.76	38.53
3-Methyl-3-ethylpentane	424.59	37.99
2,2,3-Trimethylpentane	423.88	36.93
2,2,4-Trimethylpentane	435.51	35.15
2,3,3-Trimethylpentane	427.02	37.23
2,3,4-Trimethylpentane	428.40	37.71
2,2,3,3-Tetramethylbutane	389.36	35.19

coefficients occurring in the regression models were calculated by means of an in-house Python script with the implementation of a scikit-learn machine-learning module using least square fitting.[31]

Degeneracy calculation

The degeneracy of the Sombor index, the reduced Sombor index and the average Sombor index was determined using a measure proposed by Konstantinova.[32] This quantity was named sensitivity of a topological molecular descriptor and it is defined as follows:

$$\text{Sensitivity} = \frac{N - N_{TI}}{N} \tag{6}$$

where N is the number of isomers and N_{TI} denotes the number of isomers that cannot be distinguished by topological index (TI). Nowadays, this feature is commonly presented as the degeneracy of a topological index:

$$D = 100(1 - \text{Sensitivity}) \tag{7}$$

Within this study, two molecules (A and B) are considered to have the same value of TI if the following condition is fulfilled:

$$|TI(\text{A}) - TI(\text{B})| < 10^{-13} \tag{8}$$

This threshold was chosen because of the precision of common Python computations, which is 10^{-15}.

RESULTS AND DISCUSSION

Predictive potential of Sombor indices

The initial step for developing a linear model for predicting the entropy of molecules was to correlate the calculated values of SO, SO_{red} and SO_{avg} with the experimental data of octanes. With this, it was checked whether SO, SO_{red} and SO_{avg} contain information that may be used to model entropy. The entropy values are plotted in Fig. 1 against the SO values of the octane isomers.

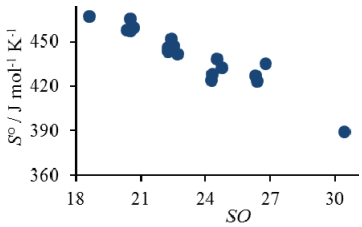

Fig. 1. The correlation between the Sombor index and entropy of octane isomers.

The scatter plot depicted in Fig. 1 shows a reasonable correlation between the Sombor index and entropy. Such a correlation indicates that a linear model for predicting the entropy of octanes could be developed using the Sombor index. A deeper insight into this correlation reveals that the data points are assembled into six clusters. Such grouping suggests that the data points within the same group have some parameter(s) in common. Namely, by direct checking, it was discovered that the points within one group have the same value of Zg_1. The correlations between reduced Sombor index and average Sombor index and entropy

are available in the Supplementary material to this paper (Figs. S-1 and S-2). The grouping of the data points is also present in these correlations, and it was revealed that Zg_1 also directs this clustering.

Since the Sombor indices showed satisfactory correlation with the entropy of octanes, the correlation between these descriptors and the enthalpy of vaporization was tested (Table I). The correlation between the Sombor index and $\Delta H°_{vap}$ is depicted in Fig. 2.

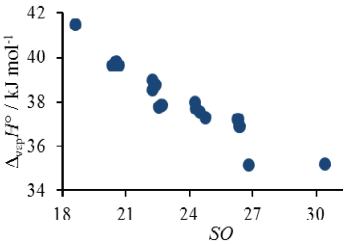

Fig. 2. The correlation between the Sombor index and enthalpy of vaporization of octane isomers.

The scatter plot presented in Fig. 2 shows that a linear dependence between Sombor index and enthalpy of vaporization exists. In addition, Fig. 2 illustrates that the data points are grouped, as in the previous case. Namely, it is obvious that the *SO* values are clustered into six different groups. Again, by direct checking, it was found that the data points within one group have the same values of Zg_1. The correlations between reduced and average Sombor indices and enthalpy of vaporization are depicted in Figs. S-3 and S-4 of the Supplementary material. The same groupation of the SO_{red} and SO_{avg} values is noticed.

As all examined correlations show linear relationships between the Sombor indices and these two physico-chemical properties, two types of linear models were constructed, (Eqs. (9) and (10)). Namely, in the model based on Eq. (9), the entropy or the enthalpy of vaporization is predicted only by one of the Sombor indices, while in the other model physicochemical property is predicted by one of the Sombor indices and the first Zagreb index:

$$S°, \Delta H°_{vap} \approx ATI + B \quad (9)$$

$$S°, \Delta H°_{vap} \approx ATI + BZg_1 + C \quad (10)$$

In these equations *TI* stands for the *SO*, SO_{red} and SO_{avg}, whereas *A*, *B* and *C* are the fitting coefficients. The values for the fitting parameters are presented in Table II.

The entropy and the enthalpy of vaporization of octanes were calculated using these models. The results of the evaluation of the models are presented in Table III.

In Table III, R^2, R_{adj}^2 and *RMSE* denote the coefficient of determination, adjusted coefficient of determination, and root mean square error, respectively. *F* denotes the value obtained by partial *F*-test and *p* stands for the *p*-value.

TABLE II. The values for the fitting parameters occurring in the models

Parameter	*TI*	Models based on Eq. (9)		Models based on Eq. (10)		
		A	*B*	*A*	*B*	*C*
$S°$ / J mol^{-1} K^{-1}	*SO*	–6.16	584.94	11.43	–17.47	713.82
	SO_{red}	–5.51	520.98	11.05	–18.36	847.94
	SO_{avg}	–5.22	491.66	3.45	–10.17	721.85
$\Delta H°_{vap}$ / kJ mol^{-1}	*SO*	–0.52	50.40	–1.97	1.44	39.77
	SO_{red}	–0.47	45.02	–2.17	1.88	11.49
	SO_{avg}	–0.44	42.49	–0.94	0.59	29.20

TABLE III. The results of evaluation of the linear regression models

TI	Models based on Eq. (9)			Models based on Eq. (10)				
	R^2 / %	R^2_{adj} / %	*RMSE* / J mol^{-1} K^{-1}	R^2 / %	R^2_{adj} / %	*RMSE* / J mol^{-1} K^{-1}	*F*	*p*
				$S°$				
SO	89.59	88.94	5.93	92.14	91.65	5.15	4.87	0.043
SO_{red}	89.23	88.56	6.03	92.53	92.06	5.02	6.63	0.021
SO_{avg}	89.48	88.82	5.96	91.36	90.82	5.40	3.27	0.091
				$\Delta_{vap}H°$				
SO	89.67	89.03	0.50	92.09	91.59	0.44	4.57	0.049
SO_{red}	90.65	90.07	0.48	95.47	95.19	0.33	15.96	0.001
SO_{avg}	89.84	89.21	0.50	90.71	90.13	0.47	1.41	0.254

The evaluation results presented in Table III show that the entropy and the enthalpy of vaporization of alkanes could be satisfactorily predicted using simple models based on Eq. (9). Namely, almost 90 % of data variance of $S°$ and $\Delta H°_{vap}$ may be explained by linear model where one of the Sombor indices is the only predictor. Furthermore, the errors that these models produce are small, especially for the enthalpy of vaporization. Among all these models, the model for predicting $\Delta H°_{vap}$ that uses reduced Sombor index showed the best performance. Namely, its R^2 value amounts 90.65 % and this model also yields smallest error.

To obtain better insight into the models, the predictive potential of Sombor indices were compared with predictive capability of other degree-based indices. Namely, for this purpose, the Randić index[33] and two Adriatic indices[34] (misbalance lodeg index and misbalance rodeg index) were used. It was found that Sombor indices demonstrate better prediction of entropy, since Randić and Adriatic indices explain around 80 % of data variance. Considering the enthalpy of vaporization, the Adriatic indices performed somewhat better. Namely, these indices describe around 96 % of data variance. Since the Randić and Adriatic indices showed similar predictive potential, it was supposed that a correlation might exist between these indices and the Sombor indices. To test this assumption, the correlations between the reduced Sombor index and these indices were checked. The correlations between the reduced Sombor index and Randić index and Adriatic indices are depicted in Figs. 3–5.

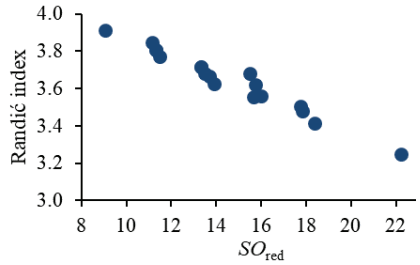

Fig. 3. The correlation between reduced Sombor index and Randić index. The correlation coefficient is –0.9815.

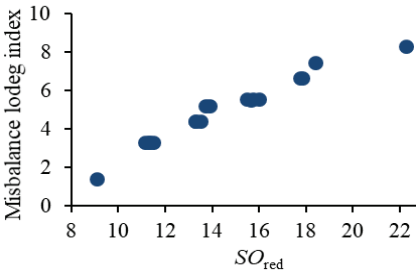

Fig. 4. The correlation between reduced Sombor index and misbalance lodeg index. The correlation coefficient is 0.9790.

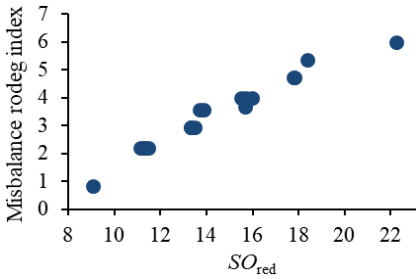

Fig. 5. The correlation between reduced Sombor index and the misbalance rodeg index. The correlation coefficient is equal to 0.9812.

The reduced Sombor index showed good correlations with the Randić and Adriatic indices. These findings indicate that mathematical relations between these indices may be established.

With the introduction of first Zagreb index as a second predictor, the performance of the present models is improved. Now, most of the models explain a huge amount of the data variance. The statistical justification of the introduction of Zg_1 was examined using the partial F-test with 95 % of confidence. Namely, F-value from Table III represents the result of this statistical procedure. A null hypothesis was that Zg_1 does not contribute to the explanation of the data variation. The results show that introduction of Zg_1 in the Sombor index and the reduced Sombor index models is statistically justified (see F and p values). Since F-value associated with the average Sombor index is lower than the critical value, the introduction of Zg_1 is not supported. Therefore, models based on Eq. (10) with the average Sombor index are omitted from further consideration.

In the case of entropy, the reduced Sombor index shows slightly better performance (R^2 = 92.53 %) over the Sombor index. Considering the enthalpy of

vaporization, the reduced Sombor index exerts a noticeably better predictive potential than Sombor index. Namely, its R^2 value amounts 95.47 %, and the error is quite small (0.33 kJ mol^{-1}).

In Figs. 6 and 7, correlations between the experimental values and those predicted by the reduced Sombor index and the first Zagreb index are illustrated. As may be seen, these figures illustrate that there is very good agreement between experimental and predicted data. The correlations for the other models are presented in the Supplementary material (Figs. S-5–S-8).

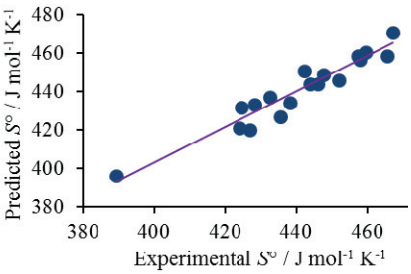

Fig. 6. The correlation between experimental and predicted values for the entropy.

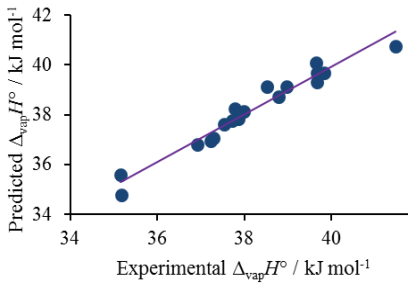

Fig. 7. The correlation between experimental and predicted values for the enthalpy of vaporization.

An external validation of the model for predicting enthalpy of vaporization by SO_{red} and Zg_1 was realized using the data set from Table IV. This data set consists of 35 values for $\Delta H°_{vap}$ of nonanes. This data set was randomly split, using scikit-learn module, into a training set and a test set (80:20). The training set was used to fit the model.

The values for the fitting parameters and the coefficients of determination are given in Table V. With 91.98 % of explained variance in the test set, the presented model showed excellent predictive potential. The correlation between experimental and predicted enthalpy of vaporization is depicted in Fig. 8.

Discriminative potential of Sombor indices

In order to test the discriminative potential of the Sombor indices, a series of chemical tree isomers were constructed. Namely, the number of vertices in these series ranged from 10 up to 20. The results of this investigation are tabulated in Table VI.

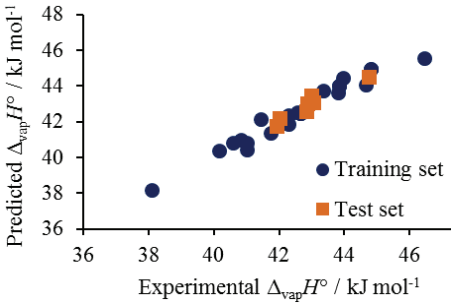

Fig. 8. The correlation between experimental and predicted values.

TABLE IV. The data used for the external validation

Molecule	$\Delta H°_{vap}$ / kJ mol^{-1}
n-Nonane	46.44
2-Methyloctane	44.65
3-Methyloctane	44.75
4-Methyloctane	44.75
2,2-Dimethylheptane	42.28
2,3-Dimethylheptane	43.79
2,4-Dimethylheptane	42.87
2,5-Dimethylheptane	42.87
2,6-Dimethylheptane	42.82
3,3-Dimethylheptane	42.66
3,4-Dimethylheptane	43.84
3,5-Dimethylheptane	42.98
4,4-Dimethylheptane	42.66
3-Ethylheptane	44.81
4-Ethylheptane	44.81
2,2,3-Trimethylhexane	41.91
2,2,4-Trimethylhexane	40.57
2,2,5-Trimethylhexane	40.17
2,3,3-Trimethylhexane	42.23
2,3,4-Trimethylhexane	42.93
2,3,5-Trimethylhexane	41.42
2,4,4-Trimethylhexane	40.84
3,3,4-Trimethylhexane	42.28
2-Methyl-3-ethylhexane	43.84
2-Methyl-4-ethylhexane	42.98
3-Methyl-3-ethylhexane	43.04
3-Methyl-4-ethylhexane	43.95
2,2,3,3-Tetramethylpentane	41.00
2,2,3,4-Tetramethylpentane	41.00
2,2,4,4-Tetramethylpentane	38.10
2,3,3,4-Tetramethylpentane	41.75
2,2-Dimethyl-3-ethylpentane	42.02
2,3-Dimethyl-3-ethylpentane	42.55
2,4-Dimethyl-3-ethylpentane	42.93
3,3-Diethylpentane	43.36

TABLE V. The values for the fitting parameters and the coefficients of determination

Parameter	Value	R^2 / %
A / kJ mol^{-1}	–2.44	Training set: 95.68
B / kJ mol^{-1}	2.20	Test set: 91.98
C / kJ mol^{-1}	5.16	

TABLE VI. The degeneracy of the Sombor indices

n	# of chemical trees	D (SO) / %	D (SO_{red}) / %	D (SO_{avg}) / %
10	75	33.33	34.67	34.67
11	159	47.80	45.91	47.80
12	355	60.56	60.56	61.41
13	802	71.32	71.57	71.82
14	1858	80.36	81.00	81.05
15	4347	87.12	87.69	87.35
16	10359	91.71	92.47	92.88
17	24894	94.85	95.49	94.97
18	60523	96.92	97.37	97.06
19	148284	98.14	98.49	98.25
20	366319	98.92	99.15	99.03

The percentages presented in Table VI show that the Sombor index, reduced Sombor index, and average Sombor index exert modest discriminative potential. All three descriptors show similar sensitivity. For example, within 355 chemical trees (n = 12), more than 60 % of the molecules cannot be distinguished by these topological molecular descriptors. Such degeneracy of the Sombor indices is in accordance with the degeneracy of other degree-based graph invariants. Namely, this class of indices show lower discriminative potential compared to eigenvalue-based descriptors. The degeneracy is plotted against the number of vertices in Fig. 9, which demonstrates that the degeneracy of the Sombor indices increases with the increasing number of molecules.

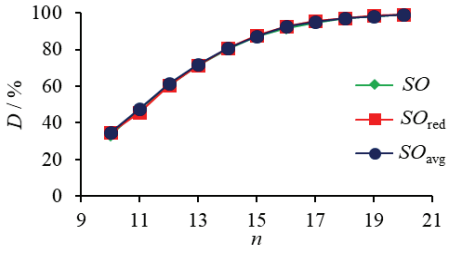

Fig. 9. Percentage of the degeneracy of the Sombor index, the reduced Sombor index, and the average Sombor index. Note that all three curves almost fully overlap.

CONCLUSIONS

Within this study, the chemical applicability of the Sombor indices was examined. More precisely, their predictive and discriminative potentials. The Sombor index, the reduced Sombor index, and the average Sombor index were

used to model the entropy and enthalpy of vaporization of alkanes. Simple linear models that use one of these indices as the only predictor showed satisfactory predictive potential. The performance of these models was improved with the introduction of the first Zagreb index as a second predictor. Among these three topological molecular descriptors, the reduced Sombor index showed the best performance. An external validation of the derived model was applied, and the reduced Sombor index showed up well. The results of the testing of the predictive potential of the Sombor indices indicate that these descriptors may be successfully applied for the modeling of thermodynamic properties of compounds.

The discriminative potential of the Sombor indices was tested on several groups of chemical trees. All three descriptors exhibit modest sensitivity. In a large class of isomers, a great number of molecules cannot be distinguished by these indices. This result is in accordance with the degeneracy of other degree-based graph invariants.

SUPPLEMENTARY MATERIAL

Additional data are available electronically at the pages of journal website: https://www.shd-pub.org.rs/index.php/JSCS/index, or from the corresponding author on request.

Acknowledgment. This work was supported by the Ministry of Education, Science and Technological Development of the Republic of Serbia (Agreement No. 451-03-68/2020-14/200122).

ИЗВОД

ХЕМИЈСКА ПРИМЕЊИВОСТ СОМБОР ИНДЕКСА

ИЗУДИН РЕЦЕПОВИЋ

Институт за хемију, Природно–математички факултет, Универзитет у Крагујевцу, Радоја Домановића 12, 34000 Крагујевац

Недавно је предложена нова класа тополошких молекулских дескриптора заснованих на степену чвора, тзв. Сомбор индекси. У оквиру ове студије испитивани су предикциони и дискриминативни потенцијал Сомбор индекса, редукованог Сомбор индекса и просечног Сомбор индекса. Сва три тополошка молекулска дескриптора показала су добар предикциони потенцијал. Статистички подаци указују на то да редуковани Сомбор индекс има нешто бољи предикциони потенцијал у односу на друга два индекса. Спољном валидацијом модела потврђен је овај резултат. Такође, тестирањем на великој групи изомера утврђено је да ови индекси имају умерен дискриминативни потенцијал.

(Примљено 15. децембра 2020, ревидирано 10. јануара, прихваћено 30. јануара 2021)

REFERENCES

1. X. Ling, J. Bajorath, *Comb. Chem. High Throughput Screen.* **3** (2000) 363 (https://doi.org/10.2174/1386207003331454)
2. R. Todeschini, V. Consonni, *Molecular Descriptors for Chemoinformatics*, Wiley, Weinheim, 2009 (https://doi.org/10.1002/9783527628766)
3. H. Hong, Q. Xie, W. Ge, F. Qian, H. Fang, L. Shi, Z. Su, R. Perkins, W. Tong, *J. Chem. Inf. Model.* **48** (2008) 1337 (https://doi.org/10.1021/ci800038f)

4. S. Sahoo, C. Adhikari, M. Kuanar, B. K. Mishra, *Curr. Comput. Aided Drug Des.* **12** (2016) 181 (https://doi.org/10.2174/1573409912666160525112114)
5. A. R. Katritzky, E. V. Gordeeva, *J. Chem. Inf. Comput. Sci.* **33** (1993) 835 (https://doi.org/10.1021/ci00016a005)
6. M. Karelson, *Molecular Descriptors in QSAR/QSPR*, Interscience, New York, 2000 (ISBN: 978-0-471-35168-9)
7. M. Dehmer, K. Varmuza, D. Bonchev, *Statistical Modelling of Molecular Descriptors in QSAR/QSPR*, John Wiley & Sons, Weinheim, 2012 (https://doi.org/10.1002/9783527645121)
8. K. Roy, S. Kar, R. N. Das, *A Primer on QSAR/QSPR Modeling-Fundamental Concepts*, Springer, Cham, 2015 (https://doi.org/10.1007/978-3-319-17281-1)
9. J. Bajorath, *J. Chem. Inf. Comput. Sci*. **41** (2001) 233 (https://doi.org/10.1021/ci0001482)
10. F. Grisoni, D. Reker, P. Schneider, L. Friedrich, V. Consonni, R. Todeschini, A. Koeberle, O. Werz, G. Schneider, *Mol. Inform.* **36** (2017) 1600091 (https://doi.org/10.1002/minf.201600091)
11. N. Trinajstić, *Chemical Graph Theory*, Routledge, New York, 2018 (https://doi.org/10.1201/9781315139111)
12. D. Bonchev, *Chemical Graph Theory: Introduction and Fundamentals*, CRC Press, Boca Raton, FL, 1991 (ISBN: 978-0856264542)
13. I. Gutman, *Selected Theorems in Chemical Graph Theory,* University of Kragujevac, Kragujevac, 2017 (ISBN: 978-86-6009-039-5)
14. E. Estrada, G. Patlewicz, E. Uriarte, *Indian J. Chem., A* **42** (2003) 1315 (http://hdl.handle.net/123456789/20663)
15. R. Zanni, M. Galvez-Llompart, R. Garcia-Domenech, J. Galvez, *Expert Opin. Drug Discov.* **10** (2015) 945 (https://doi.org/10.1517/17460441.2015.1062751)
16. O. Ivanciuc, *Curr. Comput. Aided Drug Des.* **9** (2013) 153 (https://doi.org/10.2174/1573409911309020002)
17. I. Redžepović, B. Furtula, *J. Comput. Aided Mol. Des.* **34** (2020) 975 (https://doi.org/10.1007/s10822-020-00320-2)
18. I. Redžepović, Y. Mao, Z. Wang, B. Furtula, *Int. J. Quantum Chem.* **120** (2020) e26209 (https://doi.org/10.1002/qua.26209)
19. I. Redžepović, B. Furtula, *J. Serb. Soc. Comput. Mech.* Special Issue (2020) 37 (https://doi.org/10.24874/jsscm.2020.01.04)
20. R. Gozalbes, J. P. Doucet, F. Derouin, *Curr. Drug Targets Infect. Disord*. **2** (2002) 93 (https://doi.org/10.2174/1568005024605909)
21. I. Gutman, N. Trinajstić, *Chem. Phys. Lett.* **17** (1972) 535 (https://doi.org/10.1016/0009-2614(72)85099-1)
22. S. Nikolić, G. Kovačević, A. Miličević, N. Trinajstić, *Croat. Chem. Acta* **76** (2003) 113 (https://hrcak.srce.hr/103086)
23. I. Gutman, K. C. Das, *MATCH Commun. Math. Comput. Chem.* **50** (2004) 83 (http://match.pmf.kg.ac.rs/electronic_versions/Match50/match50_83-92.pdf)
24. M. Eliasi, A. Iranmanesh, I. Gutman, *MATCH Commun. Math. Comput. Chem.* **68** (2012) 217 (http://match.pmf.kg.ac.rs/electronic_versions/Match68/n1/match68n1_217-230.pdf)
25. A. Ali, N. Trinajstić, *Mol. Inform.* **37** (2018) 1800008 (https://doi.org/10.1002/minf.201800008)

26. Z. Raza, A. Ali, *Int. J. Quantum Chem*. **120** (2020) e26333 (https://doi.org/10.1002/qua.26333)
27. T. Došlić, B. Furtula, A. Graovac, I. Gutman, S. Moradi, Z. Yarahmadi, *MATCH Commun. Math. Comput. Chem.* **66** (2011) 613 (http://match.pmf.kg.ac.rs/electronic_versions/Match66/n2/match66n2_613-626.pdf**)**
28. I. Gutman, *MATCH Commun. Math. Comput. Chem.* **86** (2021) 11 (http://match.pmf.kg.ac.rs/content86n1.htm)
29. M. Randić, *J. Math. Chem.* **7** (1991) 155 (https://doi.org/10.1007/BF01200821)
30. www.moleculardecriptors.eu (accessed February 15, 2020)
31. F. Pedregosa, G. Varoquaux, A. Gramfort, V. Michel, B. Thirion, O. Grisel, M. Blondel, P. Prettenhofer, R. Weiss, V. Dubourg, J. Vanderplas, A. Passos, D. Cournapeau, M. Brucher, M. Perrot, E. Duchesnay, *J. Mach. Learn. Res.* **12** (2011) 2825 (https://www.jmlr.org/papers/volume12/pedregosa11a/pedregosa11a.pdf)
32. E. V. Konstantinova, *J. Chem. Inf. Comput. Sci.* **36** (1996) 54 (https://doi.org/10.1021/ci9502461)
33. M. Randić, *J. Am. Chem. Soc.* **97** (1975) 6609 (https://doi.org/10.1021/ja00856a001)
34. D. Vukičević, M. Gašperov, *Croat. Chem. Acta* **83** (2010) 243 (https://hrcak.srce.hr/62202).

Journal of the Serbian Chemical Society
JSCS-info@shd.org.rs • www.shd.org.rs/JSCS
J. Serb. Chem. Soc. 86 (5) S98–S100 (2021) *Supplementary material*

SUPPLEMENTARY MATERIAL TO

Chemical applicability of Sombor indices

IZUDIN REDŽEPOVIĆ*

Department of Chemistry, Faculty of Science, University of Kragujevac, P. O. Box 60, 34000 Kragujevac, Serbia

J. Serb. Chem. Soc. 86 (5) (2021) 445–457

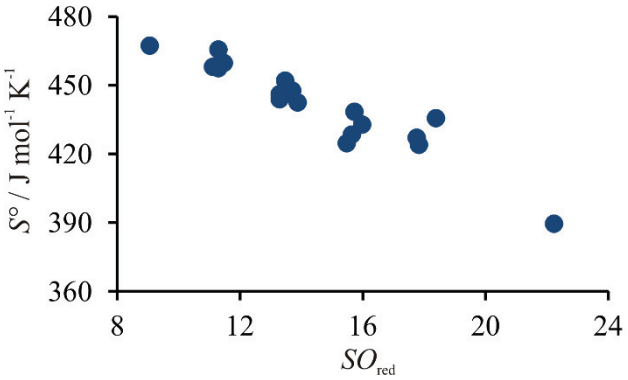

Fig. S-1. The correlation between the reduced Sombor index and entropy of octane isomers.

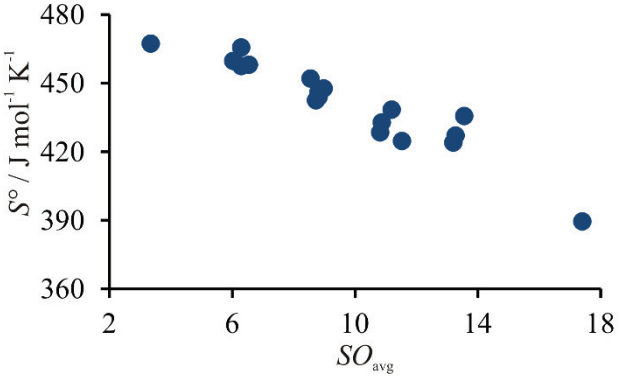

Fig. S-2. The correlation between the average Sombor index and the entropy of octane isomers.

* E-mail: izudin.redzepovic@pmf.kg.ac.rs

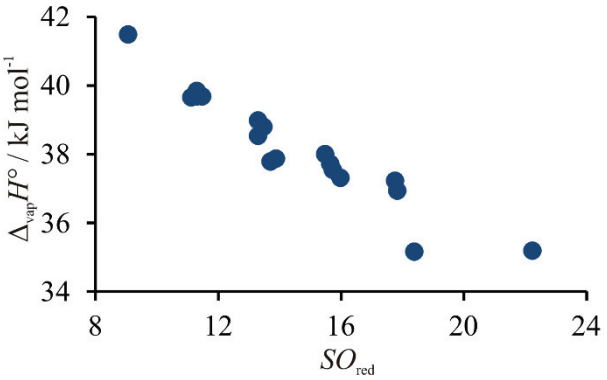

Fig. S-3. The correlation between the reduced Sombor index and the enthalpy of vaporization of octane isomers.

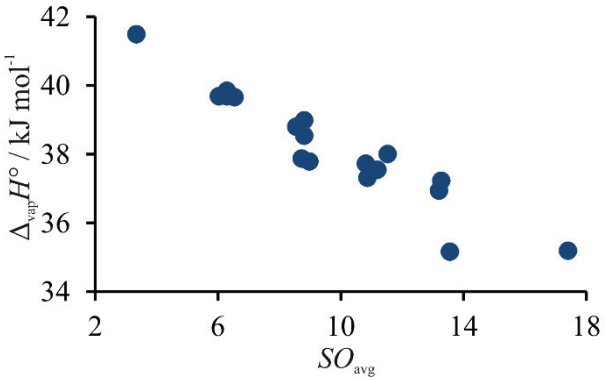

Fig. S-4. The correlation between the average Sombor index and the enthalpy of vaporization of octane isomers.

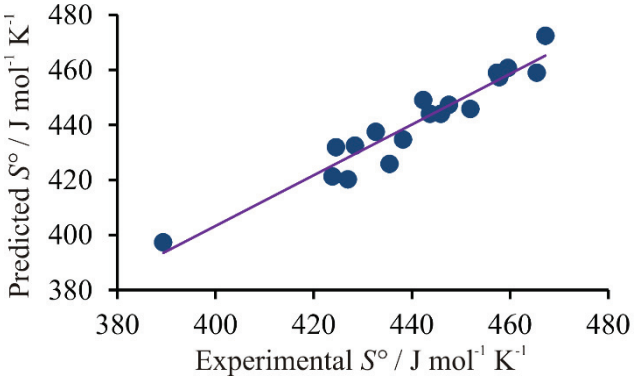

Fig. S-5. The correlation between the experimental and predicted data using the Sombor index and the first Zagreb index.

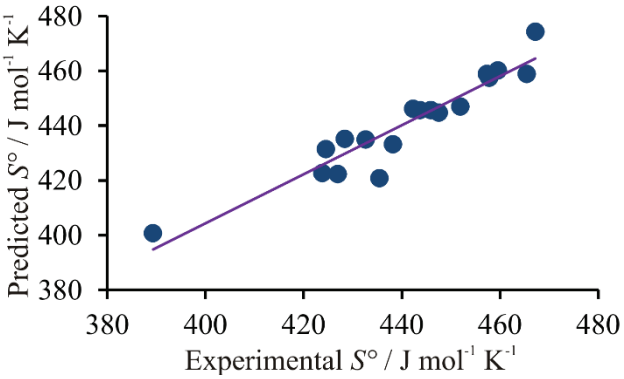

Fig. S-6. The correlation between the experimental and predicted data using the average Sombor index.

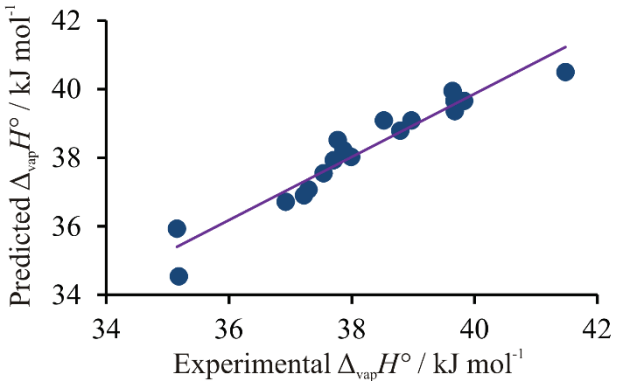

Fig. S-7. The correlation between the experimental and predicted data using the Sombor index and the first Zagreb index.

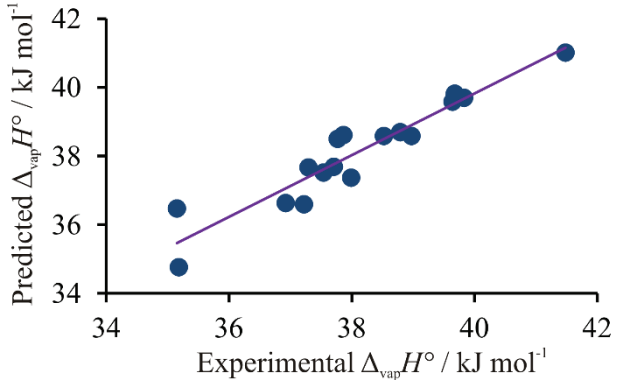

Fig. S-8. The correlation between the experimental and predicted data using the average Sombor index and the first Zagreb index.

Journal of the Serbian Chemical Society
JSCS-info@shd.org.rs • www.shd.org.rs/JSCS
J. Serb. Chem. Soc. *86* (5) 459–468 (2021)
JSCS–5434
Original scientific paper

Synthesis, characterization and biological activity of Pt(II) complexes with steroidal thiosemicarbazones

BOŽIDAR R. ČOBELJIĆ[1]*#, MARIJANA B. ŽIVKOVIĆ[2#], IVANA Z. MATIĆ[3], IRENA T. NOVAKOVIĆ[2#], DUŠAN M. SLADIĆ[1#], KATARINA K. ANĐELKOVIĆ[1#] and NATALIJA M. KRSTIĆ[2#]

[1]*University of Belgrade, Faculty of Chemistry, Studentski trg 12–16, P. O. Box 158, Belgrade, Serbia,* [2]*University of Belgrade-Institute of Chemistry, Technology and Metallurgy, Department of Chemistry, Njegoševa 12, 11000 Belgrade, Serbia and* [3]*Institute of Oncology and Radiology of Serbia, Pasterova 14, Belgrade, Serbia*

(Received 11 December, revised and accepted 14 December 2020)

Abstract: In this work, Pt(II) complexes of previously synthesized steroidal thiosemicarbazones were synthesized and characterized. The ligands and their metal complexes were studied by analytical and spectroscopic data (elemental analysis, IR, 1D-NMR and 2D-NMR, HSQC, HMBC, NOESY, COSY), the analysis of which enabled complete ^{1}H and ^{13}C assignments of each compound including *E* and *Z* isomers. All the synthesized ligands and complexes were screened for their cytotoxic and antimicrobial activity. The results demonstrate that the new steroidal thiosemicarbazone complexes were significantly less cytotoxic than the corresponding steroidal thiosemicarbazones. In addition, complexes showed lower antimicrobial activity than the standard drugs, similar to the activity of the starting thiosemicarbazones.

Keywords: 3-oxo-*α*,*β*-unsaturated steroids; hydrazones; square–planar complexes; cytotoxicity; antimicrobial activity.

INTRODUCTION

Steroids are a group of biologically active molecules widespread in nature that play a very important role in biological systems. In addition, steroid-based chemotherapeutics are widely used in medicine. Therefore, certain functional and structural modifications of the steroid core by the addition of new functional groups or heterocyclic systems could be very useful, giving compounds with new and more pronounced biological activity.[1] Likewise, substituted thiosemicarbazone derivatives have proven to be very useful because of their interesting biological behaviour.[2] These compounds may act as antidepressants,[3] muscle relax-

* Corresponding author. E-mail: bozidar@chem.bg.ac.rs
# Serbian Chemical Society member.
https://doi.org/10.2298/JSC201211083C

ants, psychoeptic, hypnotics,[4–7] and also show antimicrobial,[2,8,9] antiamoebic,[10] anti-inflammatory,[11,12] and cytotoxic activities.[13] Thiosemicarbazones are compounds that could be used as possible ligands for metal complexes and for the syntheses of heterocyclic compounds.[14–20]

Taking all this into consideration, new steroidal mono- (**2a**,**b**) and bis(thiosemicarbazones) (**3a**,**b**), obtained from 19-norandrost-4-ene-3,17-dione (**1a**) and androsta-4,9(11)-diene-3,17-dione (**1b**), have recently been synthesized[21] (Scheme 1). All these compounds were fully characterized and their biological activity was examined. It was found that 3-thiosemicarbazones **2a** and **2b** exhibit very high cytotoxic actions against all examined cancer cell lines, much higher than the corresponding starting steroids **1a** and **1b** or thiosemicarbazide itself.

In the late 1960s, Rosenberg[22–25] discovered the anticancer activity of cisplatin which began to be used in the treatment of cancer. Since the discovery of cisplatin, to this day, a large number of metal complexes have been synthesized in order to find potential chemotherapeutics with better antitumor potential, higher selectivity in killing cancer cells and fewer side effects.[26]

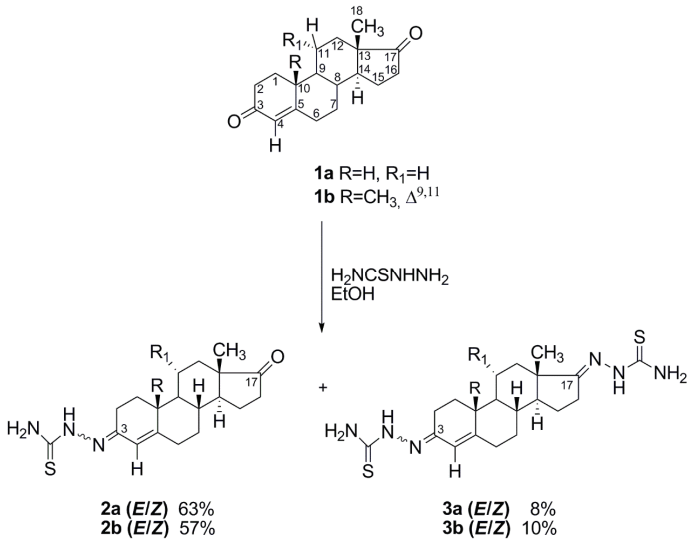

Scheme 1. Synthesis of steroidal thiosemicarbazones.

Motivated by the aforementioned issues and as a continuation of our work on new hetero-steroid derivatives as biologically active molecules,[1,21,27–30] it was decided to prepare new steroidal complexes with platinum, in the reaction of previously synthesized 3-thiosemicarbazones **2a** and **2b** with cisplatin, and to examine their biological activity and compare the results with the activity of those reported earlier.[21] To the best of our knowledge, very few Pt steroidal complexes have been prepared to date.[31,32]

EXPERIMENTAL

Chemistry

The melting points were determined on a Digital melting point WRS-1B apparatus and are uncorrected. The IR spectra were recorded on a Perkin–Elmer FT-IR 1725X spectrophotometer. The NMR spectra were recorded on a Bruker Avance 500 MHz spectrometer (^{1}H at 500 MHz and ^{13}C at 125 MHz) in DMSO-d_6 at room temperature using $SiMe_4$ as the internal standard, δ/ppm, J/Hz. The HRMS spectra were recorded on an Agilent 6210 LC ESI-MS TOF spectrometer. The elemental analyses (C, H, N and S) were performed by standard micro-methods on a Vario EL III analyzer. The molar conductivities were measured at room temperature (25 °C) on a digital Cond 330i conductivity meter. Thin-layer chromatography (TLC) was performed using aluminum plates coated with Merck silica gel 60 F_{254} and flash column chromatography (FCC) was performed on silica gel Merck 0.040–0.063 mm. The TLC spots were detected with 50 % aq. H_2SO_4 followed by heating. 19-Norandrost-4-ene-3,17-dione and androsta-4,9(11)-diene-3,17-dione were purchased from Galenika AD ($_{Belgrade}$) and recrystallized from a suitable solvent. c*is*-Diaminedichloridoplatinum(II) ($[Pt(NH_3)_2Cl_2]$) was obtained from Sigma–Aldrich.

General procedure for the synthesis of thiosemicarbazones

Thiosemicarbazones **2a** and **2b** were prepared as described earlier.[21] To a solution of steroid (**1a**,**b**, 1 mmol) in dried ethanol (50 mL), thiosemicarbazide (1 mmol) was added. The solution was then allowed to reflux for 5 h under stirring. The pH of the mixture was adjusted to ≈4.5 with CH_3COOH (about 3 mL). After completion of the reaction (monitored by TLC), the solvent was removed under reduced pressure. The residue was chromatographed by FCC using the indicated solvent system. In both cases the products were obtained as inseparable mixtures of *E* and *Z* diastereoisomers.

*19-Norandrost-4-ene-3,17-dione 3-thiosemicarbazone (**2a**) (E/Z=7:3)*

Starting with 270 mg 19-norandrost-4-en-3,17-dione (**la**), elution with toluene/EtOAc (8/2) afforded compound **2a** (217 mg, 63 %).

*Androsta-4,9(11)-diene-3,17-dione 3-thiosemicarbazone (**2b**) (E/Z=8:2)*

Starting with 285 mg androsta-4,9(11)-diene-3,17-dione (**1b**), elution with toluene/ /EtOAc (85/15) afforded compound **2b** (189 mg, 53 %).

*Synthesis of complexes **4** and **5***

*Complex **4** (Pt(II) with ligand **2a**).* Into a solution of 19-norandrost-4-ene-3,17-dione 3-thiosemicarbazone (**2a**, 0.1 mmol, 34.5 mg) in dichloromethane (10 mL) was added cisplatin ($[Pt(NH_3)_2Cl_2]$, 0.1 mmol, 30 mg). The mixture was stirred under reflux for 3 h and filtered. The solution was then allowed to cool slowly to room temperature and then placed in a refrigerator. After six days, a solid yellow precipitate was obtained. The precipitate was filtered off, washed with a small amount of methanol and dried over silica gel to give 16.9 mg (19.4 %) of complex **4.**

*Complex **5** (Pt(II) with ligand **2b**).* Into a solution of androsta-4,9(11)-diene-3,17-dione 3-thiosemicarbazone (**2b**) (0.1 mmol, 35.7 mg) in methanol (10 mL), cisplatin ($[Pt(NH_3)_2Cl_2]$, 0.1 mmol, 30 mg) was added. The reaction mixture was stirred with heating for 3 h at 65 °C and filtered. The solution was then allowed to cool slowly to room temperature and then placed in the refrigerator. After slow evaporation of the solvent in the refrigerator (≈ 7 °C) during six days yellow solid precipitate was obtained. The precipitate was filtered off, washed with a small amount of methanol and dried over silica gel to give 14.8 mg (23.9%) of complex **5**.

The analytic and spectral data for ligands **2a** and **b** and complexes **4** and **5** are given in the Supplementary material to this paper.

Biology

Cytotoxicity assay. The cytotoxic activity of the compounds was evaluated against three human malignant cell lines: cervical adenocarcinoma (HeLa), chronic myelogenous leukemia (K562), and acute T-cell leukemia Jurkat cell line. The cytotoxicity assay procedure has been described elsewhere.[1,21,30] The positive control was the chemotherapy drug cisplatin. Survival of cells was determined by the MTT assay after 72 h of continuous action, according to the method of Mosmann,[33] which was modified by Ohno and Abe,[34] and described in detail in previous studies.[28–30] All tested cell lines were obtained from the American Type Culture Collection (Manassas, VA, USA).

Antimicrobial activity. The antibacterial activity was evaluated using two different strains of bacteria, one Gram-positive bacteria: *Clostridium sporogenes* (ATCC 19404), and one Gram-negative bacteria: *Pseudomonas aeruginosa* (ATCC 9027). Amikacin (30 μg/100 μL H_2O) was used as the positive control, while water and DMSO served as negative controls. Antibacterial activity was determined by the well diffusion method,[35] as described in detail in a previous study.[1] The fungus tested was *Aspergillus brasiliensis* (ATCC 16404). Nystatin (30 μg/100 μL DMSO) was used as the positive control, while DMSO served as the negative control. The antifungal activity was determined according to the method described in detail in a previous study.[1]

The brine shrimp test. The brine shrimp test of toxicity was performed against freshly hatched nauplii of *Artemia salina*.[36] The method was slightly modified as described earlier.[29] The compounds were dissolved in DMSO and diluted by artificial seawater until the concentration range of 0.01–0.50 mg mL^{-1} was obtained. The final concentration of DMSO was 1 % and did not cause changes of viability of nauplii. The number of nauplii was approximately 20. Surviving nauplii were counted after 24 h, and LC_{50} (concentration lethal to 50 % of the nauplii) were determined after statistical analysis. All the tests were performed in triplicate.

RESULTS AND DISCUSSION

Steroidal thiosemicarbazones **2a** and **b** were prepared as described earlier,[21] starting from 19-norandrost-4-ene-3,17-dione (**1a**) or androsta-4,9(11)-diene--3,17-dione (**1b**) and thiosemicarbazide in EtOH in the presence of CH_3COOH. As the *α*,*β*-unsaturated 3-carbonyl group is more active than the 17-carbonyl group, the reaction was conducted by controlling an equimolar ratio of **1a**,**b** and thiosemicarbazide (1:1) to give **2a**,**b** in the yields of 63 and 57 %, respectively. Nevertheless, bis(thiosemicarbazones) **3a**,**b** were obtained as well in a small amount (8 and 10 %), even under such conditions (Scheme 1).

All synthesized compounds were fully characterized by their analytical and spectroscopic data (HRMS, IR, 1D-NMR and 2D-NMR, HSQC, HMBC, NOESY, COSY). The ^{1}H- and ^{13}C-NMR analysis revealed the presence of two diastereoisomers, which could not be separated.[21] Therefore, compounds **2a** and **b** were used as ligands for complexation reactions with $[Pt(NH_3)_2Cl_2]$ in the form of mixtures of both isomers (*E* and *Z*).

Reaction of 19-norandrost-4-ene-3,17-dione 3-thiosemicarbazone **2a** with $[Pt(NH_3)_2Cl_2]$ (mole ratio 1:1) in dichloromethane (CH_2Cl_2) gave amorphous solid compound **4** soluble in DMSO. Elemental analysis showed that complex **4** contains two molecules of the ligand (Scheme 2).

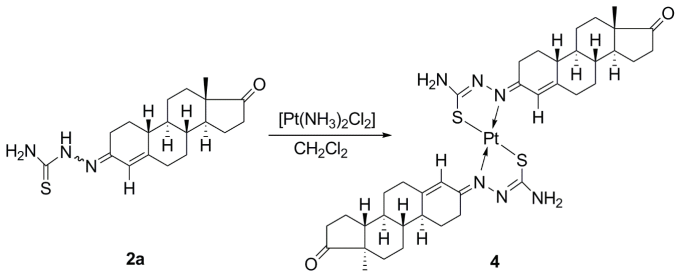

Scheme 2. Synthesis of complex **4**.

In the IR spectrum of **4**, the absorption band at 1736 cm^{-1} for the C(17)=O carbonyl was unchanged as well as sharp bands in the region 3246–3422 cm^{-1}, originating from the ν(N–H) stretching. On the other hand, the absorption bands attributed to the ν(C=N) stretching vibration appeared at higher frequencies (1528 and 1607 cm^{-1}) compared to the ones for the ligand (1497 and 1586 cm^{-1}), indicating an interaction between the azomethine nitrogen and platinum. The ^{1}H--NMR spectrum of complex **4** contained only one set of signals even though the reaction was performed with a mixture of the diastereomers (*E* and *Z*). The signal for Hα-2 proton was shifted to a lower field and was now at about 3.40 ppm, partially covered by a signal from DMSO in which the spectra were recorded. The singlet for the olefin H-4 proton occurs at δ = 6.52 ppm and the signal for H_2N protons at 6.70 ppm as an extended singlet. Besides, there is a noticeable lack of signal for the H-N proton, which in the ligand was at δ = 10.07 ppm for (*E*)- and at 10.32 ppm for (*Z*)-isomer.

In the ^{13}C-NMR spectrum, again only one set of signals was observed, indicating that the newly formed complex was symmetric. The characteristic signals were at δ / ppm = 24.8 (C-2), 25.7 (C-1), 41.4 (*d*, C-10), 122.1 (C-4), 153.3 (C-5), 161.3 (C-3), 172.3 (C=S) and 219.3 (C-17). Furthermore, the values for C-4 and C-10 suggest that the ligand in complex **4** is the (*E*)-isomer.

Complex **5** was obtained in the direct reaction of androsta-4,9(11)-diene--3,17-dione 3-thiosemicarbazone (**2b**) and cisplatin (mole ratio 1:1) in methanol (CH_3OH). The reaction mixture was stirred for 3 h at 65 °C. After filtration and slow evaporation of the solvent in a refrigerator (≈7 °C) during six days, yellow solid precipitate, complex **5**, soluble in DMSO was obtained (Scheme 3).

The band at 1739 cm^{-1} corresponding to the carbonyl group at C-17 is still visible in the IR spectrum of the synthesized complex. Moreover, the sharp bands in the 3289–3455 cm^{-1} region remain unchanged and are attributed to ν(NH_2)

vibrations. In addition, the absorption bands attributed to the ν(C=N) vibrations appeared at higher frequencies (1518 and 1608 cm^{-1}) compared to those in the corresponding ligand (1502 and 1585 cm^{-1}), indicating an interaction between the azomethine nitrogen and platinum.

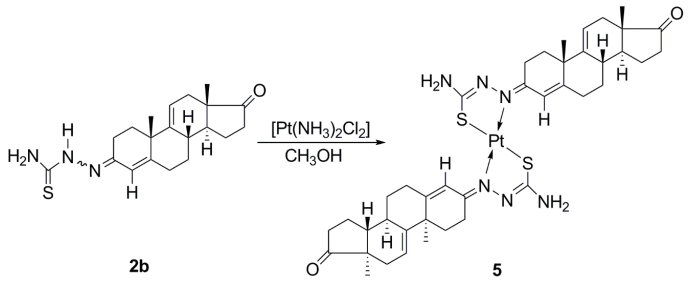

Scheme 3. Synthesis of complex **5**.

The ^{1}H-NMR spectrum of complex **5** also contains only one set of signals. The spectrum showed doublet for the H-11 olefinic proton at 5.31 ppm (J = 5 Hz), the singlet for H-4 proton at δ 6.38 ppm and an extended singlet at 6.78 ppm for the NH_2 protons. The signal for Hα-2 proton was shifted to a lower field and was now at 3.36 ppm, partially covered by a signal from DMSO in which the spectra were recorded. There is also a noticeable lack of a signal for the H-N proton, which in the ligand was at δ 10.09 ppm for the (*E*)- and 10.36 ppm for the (*Z*)-isomer.

In accordance with the above, the ^{13}C-NMR spectrum also showed only one set of signals indicating that, regardless of the fact that the reaction was performed with a mixture of isomers, in the complex **5** formation only one, probably (*E*)-isomer, participates. The characteristic signals were at δ/ppm: 24.3 (C-2), 40.4 (C-10), 121.3 (C-4), 160.6 (C-3), 156.6 (C-5), 172.9 (C=S) and 220.2 (C-17).

The molar conductivity values of **4** and **5** in DMSO were 3.4 and 1.9 μS cm^{-1}, respectively, indicating that both complexes are non-electrolytes and are stable in DMSO. Bearing all these facts in mind, as well as the results of elemental analysis, the square–planar complexes **4** and **5** consist of two deprotonated semicarbazone ligands coordinated to the metal ion *via* two thiolate sulfur atoms in the *trans* position and two azomethine nitrogen atoms.

In vitro *cytotoxic activity*

The cytotoxic activities of steroidal thiosemicarbazones **2a** and **2b**, and their Pt(II) metal complexes **4** and **5** were examined against cervical adenocarcinoma (HeLa), chronic myelogenous leukemia (K562) and acute T-cell leukemia Jurkat cell line with cisplatin used as the positive control. As shown in Table I, the steroidal platinum(II) complexes **4** and **5** were almost inactive against HeLa and K562 cells, while both complexes exhibited low cytotoxicity against the Jurkat

cell line. These results demonstrate that new steroidal thiosemicarbazone complexes were significantly less active than the corresponding steroidal thiosemicarbazones **2a** and **2b**.

TABLE I. The *in vitro* cytotoxic activity of compounds **2a**, **2b**, **4** and **5** (concentration which induced 50 % decrease (IC_{50}±*SD*, μM) in malignant cell survival); CDDP: c*is*-diamine-dichloridoplatinum(II)

Compound	HeLa	K562	Jurkat
4	>200	187.99±16.98	139.91±9.48
5	>200	>200	164.60±22.50
2a	18.1±3.3	11.3±2.2	n.a.
2b	17.3±6.8	6.7±0.3	n.a.
CDDP	4.60±0.07	6.00±0.59	3.44±0.19

In vitro *antimicrobial activity*

The *in vitro* antimicrobial activity of steroidal thiosemicarbazones and their metal complexes were assayed by the agar well diffusion method using cultures of *C. sporogenes*, *P. aeruginosa* and *A. brasiliensis*. The results (Table II) showed that only complex **5** had a very weak antibacterial activity, similar to the activity of the starting thiosemicarbazones, while neither of the complexes exhibited any antifungal activity.

TABLE II. Antimicrobial activity (Inhibition zone, mm) of the investigated compounds tested by the agar well diffusion method

Compound	Culture		
	C. sporogenes	*P. aeruginosa*	*A. brasiliensis*
4	–	–	–
5	10	10	–
2a	10	10	10
2b	10	10	10
Amikacin	22	20	–
Nystatin	–	–	30

The brine shrimp test

The LC_{50} values obtained for the ligands and newly synthesized complexes are given in Table III. All the examined compounds were found to be less toxic

TABLE III. Results of the Brine shrimp test for the investigated compounds; CDDP: c*is*-diaminedichloridoplatinum(II)

Compound	LC_{50} / mM
4	0.079
5	0.035
2a	0.597
2b	0.663
CDDP	0.006

when compared to cisplatin. However, the complexes were found to be ten times more active in the brine shrimp assay compared to the ligands.

CONCLUSION

The reactions of 19-norandrost-4-ene-3,17-dione 3-thiosemicarbazone and androsta-4,9(11)-diene-3,17-dione 3-thiosemicarbazone with cisplatin gave neutral square–planar Pt(II) complexes that consist of two deprotonated hydrazone ligands coordinated to metal ion *via* two thiolate sulfur and two azomethine nitrogen atoms.

The new steroidal thiosemicarbazone complexes were almost inactive against HeLa and K562 cells, while both complexes exhibited some cytotoxicity against the Jurkat cell line. Complex **5** showed a very weak antibacterial activity, similar to the activity of the starting thiosemicarbazones, while neither of the complexes had any antifungal activity.

Platinum complexes mostly exert their activity by covalent modification of DNA. The relatively low activity of the complexes synthesized in this work might be attributed to the absence of a good leaving group and/or high stability of the chelate complexes. Since it is excepted that platinum steroidal complexes can readily pass through cell membranes, bind to cytosolic steroid receptors and migrate to the cell nucleus, further research will be directed to the synthesis of platinum steroid complexes with enhanced reactivity with DNA.

Acknowledgment. This work was financially supported by the Ministry of Education, Science and Technological Development of the Republic of Serbia (Grant Nos. 451-03-68/ /2020-14/200168 and 451-03-68/2020-14/200026).

ИЗВОД

СИНТЕЗА, КАРАКТЕРИЗАЦИЈА И БИОЛОШКА АКТИВНОСТ КОМПЛЕКСА Pt(II) СА СТЕРОИДНИМ ТИОСЕМИКАРБАЗОНИМА

БОЖИДАР Р. ЧОБЕЉИЋ[1], МАРИЈАНА Б. ЖИВКОВИЋ[2], ИВАНА З. МАТИЋ[3], ИРЕНА Т. НОВАКОВИЋ[2], ДУШАН М. СЛАДИЋ[1], КАТАРИНА К. АНЂЕЛКОВИЋ[1] и НАТАЛИЈА М. КРСТИЋ[2]

[1]Универзитет у Београду, Хемијски факултет, Студентски трг 12–16, 11000 Београд, [2]Универзитет у Београду-Институт за хемију, технологију и металургију, Центар за хемију, Његошева 12, 11000 Београд и [3]Институт за онкологију и радиологију Србије, Пастерова 14, 11000 Београд

Почевши од претходно синтетисаних стероидних тиосемикарбазона, у овом раду су синтетисани и окарактерисани комплекси платине(II). Лиганди и њихови метални комплекси проучавани су аналитичким и спектроскопским методама (елементална анализа, ИЦ, 1D NMR и 2D NMR, HSQC, HMBC, NOESY, COSY). Анализом добијених података омогућена је потпуна ^{1}H и ^{13}C асигнација свих једињења укључујући *E* и *Z* изомере. За синтетисане лиганде, као и њихове комплексе испитивана је цитотоксична и антимикробна активност. Резултати указују на то да нови стероидни тиосемикарбазонски комплекси испољавају значајно нижу цитотоксичност од одговарајућих стероидних тиосемикарбазона. Поред тога, комплекси поседују антимикробну активност сличну активности полазних тиосемикарбазона, а нижу од стандардних лекова.

(Примљено 11. децембра, ревидирано и прихваћено 14. децембра 2020)

REFERENCES

1. M. B. Živković, I. T. Novaković, I. Z. Matić, D. M. Sladić, N. M. Krstić, *Steroids* **148** (2019) 36 (https://doi.org/10.1016/j.steroids.2019.04.010)
2. S. A. Khan, P. Kumar, R. Joshi, P. F. Iqbal, K. Saleem, *Eur. J. Med. Chem.* **43** (2008) 2029 (https://doi.org/10.1016/j.ejmech.2007.12.004)
3. N. Ergenç, N. S. Günaya, R. Demirdamar, *Eur. J. Med. Chem.* **33** (1998) 143 (https://doi.org/10.1016/S0223-5234(98)80039-1)
4. T. A. Voronina, N. M. Tozhanova, *Farmakol. Toksikol.* **44** (1981) 155 (https://www.ncbi.nlm.nih.gov › pubmed)
5. K. Swathi, M. Sarangapani, *World J. Pharm. Pharm. Sci.* **3** (2014) 2720 (https://www.wjpps.com/wjpps_controller/archive_show/2014/VOLUME%203,%20FEBRUARY,%20ISSUE%202)
6. V. Mishra, S. N. Pandeya, *Acta Pharm.* **51** (2001) 183 (http://acta.pharmaceutica.farmaceut.org/18301.html)
7. N. Ergenç, G. Çapana, N. S. Günaya, S. Özkırımlı, M. Güngör, S. Özbey, E. Kendic, *Arch. Pharm. (Weinheim, Ger.)* **332** (1999) 343 (https://doi.org/10.1002/(SICI)1521-4184(199910)332:10<343::AID-ARDP343>3.0.CO;2-0)
8. S. A. Khan, A. M. Asiri, *Chin. J. Chem.* **30** (2012) 1901 (https://doi.org/10.1002/cjoc.201200126)
9. E. Bermejo, R. Carballo, A. Castiñeiras, R. Domínguez, A. E. Liberta, C. Maichle-Mössmer, D. X. West, *Z. Naturforsch.* **54b** (1999) 777 (https://doi.org/10.1515/znb-1999-0613)
10. S. Singh, F. Athar, M. R. Maurya, A. Azam, *Eur. J. Med. Chem.* **41** (2006) 592 (https://doi.org/10.1016/j.ejmech.2006.01.014)
11. M. Asif, A. Husain, *J. Appl. Chem. (London, U. K.)* **2013** (2013), Article ID 247203 (http://dx.doi.org/10.1155/2013/247203)
12. K. Verma, S. N. Pandeya, U. K. Singh, S. Gupta, P. Prashant, Anurag, G. Bhardwaj, *Int. J. Pharm. Sci. Nanotech.* **1** (2008) 357 (https://doi.org/10.37285/ijpsn.2008.1.4.7)
13. J. A. Lessa, I. C. Mendes, P. R. O. da Silva, M. A. Soares, R. G. dos Santos, N. L. Speziali, N. C. Romeiro, E. J. Barreiro, H. Beraldo, *Eur. J. Med. Chem.* **45** (2010) 5671 (https://doi.org/10.1016/j.ejmech.2010.09.021)
14. J. M. Pérez, A. I. Matesanz, A. Martín-Ambite, P. Navarro, C. Alonso, P. Souza, *J. Inorg. Biochem.* **75** (1999) 255 (https://doi.org/10.1016/S0162-0134(99)00096-3)
15. L. H. Hall, S. Y. Cheen, J. B. Barnes, D. X. West, *Met.-Based Drugs* **6** (1999) 143 (http://dx.doi.org/10.1155/MBD.1999.143)
16. K. H. Reddy, P. S. Reddy, P. R. Babu, *J. Inorg. Biochem.* **77** (1999) 169 (https://doi.org/10.1016/S0162-0134(99)00188-9)
17. P. F. Kelly, A. M. Z. Slawin, A. Soriano-Rama, *J. Chem. Soc. Dalton Trans. (1972––1999)* (1996) 53 (https://doi.org/10.1039/DT9960000053)
18. D. X. West, S. B. Pardhye, P. B. Sonawane, *Struct. Bonding (Berlin, Ger.)* **76** (1991) 1 (https://doi.org/10.1007/3-540-53499-7_1)
19. A. E. Liberta, D. X. West, *BioMetals* **5** (1992) 121 (https://doi.org/10.1007/BF01062223)
20. D. X. West, A. E. Liberta, S. B. Padhye, R. C. Chikate, P. B. Sonawane, A. S. Kumbhar, R. G. Yerande, *Coord. Chem. Rev.* **123** (1993) 49 (https://doi.org/10.1016/0010-8545(93)85052-6)
21. M. B. Živković, I. Z. Matić, M. V. Rodić, I. T. Novaković, D. M. Sladić, N. M. Krstić, *RSC Adv.* **6** (2016) 34312 (https://doi.org/10.1039/c6ra01516f)

22. B. Rosenberg, L. Van Camp, T. Krigas, *Nature* **205** (1965) 698 (https://doi.org/10.1038/205698a0)
23. B. Rosenberg, L. Van Camp, J. E. Trosko, V. H. Mansour, *Nature* **222** (1969) 385 (https://doi.org/10.1038/222385a0)
24. P. J. Loehrer, L. H. Einhorn, *Ann. Intern. Med.* **100** (1984) 704 (https://doi.org/10.7326/0003-4819-100-5-704)
25. Z. Guo, P. J. Sadler, *Angew. Chem. Int. Ed.* **38** (1999) 1512 (https://doi.org/10.1002/(SICI)1521-3773(19990601)38:11<1512::AID-ANIE1512>3.0.CO;2-Y)
26. A. R. Savić, *PhD Thesis*, University of Belgrade, Faculty of Chemistry, 2014 (in Serbian) (https://cherry.chem.bg.ac.rs/handle/123456789/2703)
27. N. M. Krstić, M. S. Bjelaković, M. M. Dabović, V. D. Pavlović, *Molecules* **15** (2010) 3462 (https://doi:10.3390/molecules15053462)
28. N. M. Krstić, M. S. Bjelaković, V. D. Pavlović, K. Robeyns, Z. D. Juranić, I. Matić, I. Novaković, D. M. Sladić, *Steroids* **77** (2012) 558 (https://doi.org/10.1016/j.steroids.2012.02.001)
29. N. M. Krstić, V. D. Pavlović, I. T. Novaković, I. Z. Matić, D. M. Sladić, *Mol. Diversity* **17** (2013) 547 (https://doi.org/10.1007/s11030-013-9455-9)
30. N. M. Krstić, I. Z. Matić, Z. D. Juranić, I. T. Novaković, D. M. Sladić, *J. Steroid. Biochem. Mol. Biol.* **143** (2014) 365 (http://dx.doi.org/10.1016/j.jsbmb.2014.06.005)
31. A. Murugkar, B. Unnikrishnan, S. Padhye, R. Bhonde, S. Teat, E.Triantafillou, E. Sinn, *Met.-Based Drugs* **6** (1999) 177 (http://dx.doi.org/10.1155/MBD.1999.177)
32. Y. Huang, E. Kong, C. Gan, Z. Liu, Q. Lin, J. Cui, *Bioinorg. Chem. Appl.* (2015), Article ID 742592 (http://dx.doi.org/10.1155/2015/742592)
33. T. Mosmann, *J. Immunol. Methods* **65** (1983) 55 (https://doi:org/10.1016/0022-1759(83)90303-4)
34. M. Ohno, T. Abe, *J. Immunol. Methods* **145** (1991) 199 (https://doi:org/10.1016/0022-1759(91)90327-C)
35. C. Perez, M. Pauli, P. Bazerque, *Acta Biol. Med. Exp*. **15** (1990) 113
36. B. N. Meyer, N. R. Ferrigni, J. E. Putnam, L. B. Jacobsen, D. E. Nichols, J. L. McLaughlin, *Planta Med.* **45** (1982) 31 (http://dx.doi.org/10.1055/s-2007-971236).

Journal of the Serbian Chemical Society
JSCS-info@shd.org.rs • www.shd.org.rs/JSCS
J. Serb. Chem. Soc. 86 (5) S101–S103 (2021)
Supplementary material

SUPPLEMENTARY MATERIAL TO

Synthesis, characterization and biological activity of Pt(II) complexes with steroidal thiosemicarbazones

BOŽIDAR R. ČOBELJIĆ[1]*, MARIJANA B. ŽIVKOVIĆ[2], IVANA Z. MATIĆ[3], IRENA T. NOVAKOVIĆ[2], DUŠAN M. SLADIĆ[1], KATARINA K. ANĐELKOVIĆ[1] and NATALIJA M. KRSTIĆ[2]

[1]*University of Belgrade, Faculty of Chemistry, Studentski trg 12–16, P. O. Box 158, Belgrade, Serbia,* [2]*University of Belgrade-Institute of Chemistry, Technology and Metallurgy, Department of Chemistry, Njegoševa 12, 11000 Belgrade, Serbia and* [3]*Institute of Oncology and Radiology of Serbia, Pasterova 14, Belgrade, Serbia*

J. Serb. Chem. Soc. 86 (5) (2021) 459–468

ISOLATED YIELDS AND SPECTROSCOPIC DATA OF SYNTHESIZED COMPOUNDS

19-Norandrost-4-ene-3,17-dione 3-thiosemicarbazone ***(2a)*** *(E/Z=7:3)*. Yield: 63 %; R_f = 0.66 (toluene/EtOAc, 6:4, double development); m.p.: > 219 °C (decomp.); IR (ATR, cm^{-1}): 3422 & 3246 (NH), 1732 (C=O), 1586, 1497 (C=N), 1285 (C=S), 754 (C–S). ESI-TOF-MS (*m/z*): calcd. for $C_{19}H_{27}N_3OS$ $[M + H]^+$: 346.19476. Found: 346.19388.

(2a-E). ^{1}H-NMR (500 MHz, DMSO-d_6,): 0.72 (1H, *m*, H-9), 0.86 (3H, *s*, H_3C-18), 0.98 (1H, *qd*, *J* = 12.4 Hz, Hα-7), 1.12–1.33 (4H, *m*, Hα-1, Hα-11, Hα-12 & H-14), 1.42–1.56 (2H, *m*, H-8 & Hβ-15), 1.64 (1H, *d*, *J* = 11.5 Hz, Hβ-12), 1.76–1.92 (3H, *m*, Hβ-1, Hβ-7 & Hα-15), 1.96–2.09 (3H, *m*, H-10, Hβ-11 & Hα-16), 2.21 (1H, *td*, *J* = 11 & 4 Hz, Hα-6), 2.25 (1H, *m*, Hβ-2), 2.37–2.45 (2H, *m*, Hβ-6 & Hβ-16), 2.82 (1H, *dt*, *J* = 16.5 & 3.5 Hz, Hα-2), 5.87 (1H, *s*, H-4), 7.51 & 8.03 (2H, 2*brs*, NH_2), 10.07 (1H, *s*, NH); ^{13}C-NMR (125 MHz, DMSO-d_6, δ / ppm): 219.7 (*s*, C-17), 178.2 (*s*, C=S), 152.0 (*s*, C-5), 150.9 (*s*, C-3), 121.6 (*s*, C-4), 49.5 (*d*, C-14), 49.1 (*d*, C-9), 47.2 (*s*, C-13), 40.9 (*d*, C-10), 39.2 (*d*, C-8, overlapped with DMSO), 35.3 (*t*, C-16), 34.3 (*t*, C-6), 31.2 (*t*, C-12), 29.7 (*t*, C-7), 25.8 (*t*, C-11), 25.3 (*t*, C-1), 23.3 (*t*, C-2), 21.3 (*t*, C-15), 13.5 (*q*, C-18).

(2a-Z). ^{1}H-NMR (500 MHz, DMSO-d_6, δ / ppm): 0.72 (1H, *m*, H-9), 0.86 (3H, *s*, H_3C-18), 0.98 (1H, *qd*, *J* = 12 & 4 Hz, Hα-7), 1.12–1.33 (4H, *m*, Hα-1, Hα-11, Hα-12 & H-14), 1.42–1.56 (2H, *m*, H-8 & Hβ-15), 1.64 (1H, *d*, *J* = 11.5 Hz, Hβ-12), 1.76–1.92 (3H, *m*, Hβ-1, Hβ-7 & Hα-15), 1.96–2.09 (3H, *m*, H-10,

* Corresponding author. E-mail: bozidar@chem.bg.ac.rs

Hβ-11 & Hα-16), 2.21 (1H, *td*, *J* = 11 & 4 Hz, Hα-6), 2.25 (1H, *m*, Hβ-2), 2.31 (1H, *dt*, *J* = 15 & 3.5 Hz, Hα-2), 2.37–2.45 (2H, *m*, Hβ-6 & Hβ-16), 6.70 (1H, *s*, H-4), 7.51 & 7.95 (2H, 2*brs*, NH_2), 10.32 (1H, *s*, NH); ^{13}C-NMR (125 MHz, DMSO-d_6, δ / ppm): 219.7 (*s*, C-17), 178.0 (*s*, C=S), 156.2 (*s*, C-5), 148.2 (*s*, C-3), 113.2 (*s*, C-4), 49.4 (*d*, C-14), 48.9 (*d*, C-9), 47.2 (*s*, C-13), 42.1 (*d*, C-10), 39.2 (*d*, C-8, overlapped with DMSO), 35.3 (*t*, C-16), 34.9 (*t*, C-6), 31.2 (*t*, C-12), 30.0 (*t*, C-7), 27.1 (*t*, C-2), 25.8 (*t*, C-11), 25.1 (*t*, C-1), 21.3 (*t*, C-15), 13.5 (*q*, C-18).

*Androsta-4,9(11)-diene-3,17-dione 3-thiosemicarbazone (**2b**) (E/Z=8:2).* Yield: 53 %, R_f = 0.44 (toluene/EtOAc, 6:4, double development), m.p.: > 198 °C (decomp.); IR (ATR, cm^{-1}): 3425 & 3256 (NH), 3142, 2928, 1737 (C=O), 1585, 1502 (C=N), 1297 (C=S), 1087, 877; ESI-TOF-MS (*m/z*): calcd. for $C_{20}H_{27}N_3OS$ $[M + H]^+$: 358.19476. Found 358.19350.

(2b-E). ^{1}H-NMR (500 MHz, DMSO-d_6, δ / ppm): 0.79 (3H, *s*, H_3C-18), 0.98 (1H, *qd*, *J* = 13, 3 Hz, Hα-7), 1.20 (3H, *s*, H_3C-19), 1.45 (1H, *m*, H-14), 1.58 (1H, *d*, *brs*, *d*, *J* = 11 Hz, Hα-15), 1.69 (1H, *td*, *J* = 13.5 & 4.5 Hz, Hβ-1), 1.91 (1H, *dd*, *J* = 17 & 5 Hz, Hα-12), 1.96–2.05 (4H, *m*, Hα-1, Hβ-7, Hβ-12 & Hβ-15), 2.11 (1H, *dd*, *J* = 19 & 9.5 Hz, Hβ-16), 2.20–2.37 (3H, *m*, Hβ-2, Hβ-6 & H-8), 2.41 (1H, *dd*, *J* = 20 & 11 Hz, Hα-16), 2.51 (1H, *m*, Hα-6), 2.88 (1H, *dt*, *J* = 17.4 & 3.5 Hz, Hα-2), 5.49 (1H, *d*, *J* = 5.5 Hz, H-11), 5.81 (1H, *s*, H-4), 7.54 & 8.07 (2H, *brs* & *m*, NH_2), 10.09 (1H, *s*, NH); ^{13}C-NMR (125 MHz, DMSO-d_6, δ / ppm): 220.3 (*s*, C-17), 178.3 (*s*, C=S), 154.5 (*s*, C-5), 150.0 (*s*, C-3), 146.1 (*s*, C-9), 121.0 (*d*, C-4), 116.5 (*d*, C-11), 47.3 (*d*, C-14), 45.2 (*s*, C-13), 39.9 (*s*, C-10, overlapped with DMSO), 36.5 (*d*, C-8), 35.8 (*t*, C-16), 33.1 (*t*, C-12), 32.6 (*t*, C-1), 31.6 (*t*, C-6), 31.1 (*t*, C-7), 26.2 (*q*, C-19), 22.3 (*t*, C-15), 21.2 (*t*, C-2), 13.6 (*q*, C-18).

(2b-Z). ^{1}H-NMR (500 MHz, DMSO-d_6,): 0.79 (3H, *s*, H_3C-18), 0.98 (1H, *qd*, *J* = 13 & 3 Hz, Hα-7), 1.20 (3H, *s*, H_3C-19), 1.56 (1H, *m*, H-14), 1.58 (1H, *d*, *brs*, *d*, *J* = 11 Hz, Hα-15), 1.80 (1H, *td*, *J* = 13.5 & 4 Hz, Hβ-1), 1.91 (1H, *dd*, *J* = 17 & 5 Hz, Hα-12), 1.96–2.05 (4H, *m*, Hα-1, Hβ-7, Hβ-12 & Hβ-15), 2.11 (*dd*, *J* = 19, 9.5 Hz, 1H, Hβ-16), 2.20–2.35 (*m*, 3H, Hβ-2, Hβ-6, H-8), 2.41 (1H, *dd*, *J* = 20 & 11 Hz, Hα-16), 2.47 (1H, *m*, Hα-2), 2.51 (1H, *m*, Hα-6), 5.47 (1H, *m*, H-11), 6.65 (1H, *s*, H-4), 7.53 & 7.98 (2H, *brs* & *s*, NH_2), 10.36 (1H, *s*, NH); ^{13}C-NMR (125 MHz, DMSO-d_6, δ / ppm): 220.3 (*s*, C-17), 178.3 (*s*, C=S), 158.7 (*s*, C-5), 147.5 (*s*, C-3), 146.1 (*s*, C-9), 116.6 (*d*, C-11), 112.6 (*d*, C-4), 47.3 (*d*, C-14), 45.2 (*s*, C-13), 41.1 (*s*, C-10), 36.2 (*d*, C-8), 35.8 (*t*, C-16), 34.2 (*t*, C-1), 33.1 (*t*, C-12), 32.0 (*t*, C-6), 31.5 (*t*, C-7), 27.5 (*t*, C-2), 26.5 (*q*, C-19), 22.3 (*t*, C-15), 13.8 (*q*, C-18).

*Complex **4** [Pt(**2a**)$_2$]*. Yield: 19.4 %; m.p.: >200 °C (decomp.); IR (ATR, cm^{-1}): 3448, 3306, 3116, 2922, 2852, 1736, 1607, 1528, 1447, 1419, 1320, 1006, 879; Anal. calcd. for $C_{38}H_{52}N_6O_2PtS_2$: C, 51.63; H, 5.93; N, 9.51; S, 7.25 %.

Found: C, 50.96; H, 6.16; N, 10.24; S 7.52 %; Λ_M (DMSO, μS cm^{-1}): 3.4; ^{1}H-NMR (500 MHz, DMSO-d_6, δ / ppm): 0.62 (1H, *qd*, *J* = 10 & 4 Hz, H-9), 0.83 (3H, *s*, CH_3-18), 0.87–0.99 (2H, *m*, Hα-7 & Hα-12), 1.00–1.12 (2H, *m*, Hα-1 & H-14), 1.25 (1H, *qd*, *J* = 13 & 2.5 Hz, Hα-11), 1.49–1.58 (2H, *m*, H-8 & Hβ-15), 1.65 (1H, *dt*, *J* = 12.5 & 2.5 Hz, Hβ-12), 1.73 (1H, *brd*, *J* = 11.5 Hz, Hβ-11), 1.81–1.90 (3H, *m*, Hβ-2, Hβ-7 & Hα-15), 1.95 (1H, *m*, Hα-16), 2.02 (1H, *m*, Hβ-1), 2.07 (1H, *m*, H-10), 2.20–2.30 (2H, *m*, Hα-6 & Hβ-6), 2.39 (1H, *dd*, *J* = 19 & 10 Hz, Hβ-16), 3.40 (1H, *m*, Hα-2, overlapped with DMSO), 6.52 (1H, *s*, H-4), 6.70 (2H, *brs*, NH_2); ^{13}C-NMR (125 MHz, DMSO-d_6, δ / ppm): 219.3 (*s*, C-17), 172.3 (*s*, C=S), 161.3 (*s*, C-3), 153.3 (*s*, C-5), 122.1 (*d*, C-4) 50.4 (*d*, C-14), 49.7 (*d*, C-9), 47.1 (*s*, C-13), 41.4 (*d*, C-10), 38.8 (*d*, C-8), 35.1 (*t*, C-16), 34.9 (*t*, C-6), 31.4 (*t*, C-12), 29.8 (*t*, C-7), 26.3 (*t*, C-11), 25.7 (*t*, C-1), 24.8 (*t*, C-2), 21.2 (*t*, C-15), 13.5 (*q*, C-18).

Complex ***5*** *[Pt(**2b**)$_2$]*. Yield: 23.9%; m.p.; >200 °C (decomp.); IR (ATR, cm^{-1}): 3455, 3343, 3289, 3197, 2931, 2900, 2843, 1739, 1720, 1608, 1518, 1322, 1017, 826; Anal. calcd. for $C_{40}H_{52}N_6O_2PtS_2$: C, 52.91; H, 5.77; N, 9.25; S, 7.06 %. Found: C, 52.83; H, 5.80; N, 9.21; S, 7.01 %; Λ_M (DMSO. μS cm^{-1}): 1.9; ^{1}H-NMR (500 MHz, DMSO-d_6, δ / ppm): 0.75 (3H, *s*, H_3C-18), 0.85 (1H, *qd*, *J* = 13 & 2.5 Hz, Hα-7), 1.16 (3H, *s*, H_3C-19), 1.24 (1H, *m*, H-14), 1.49–1.63 (2H, *m*, Hβ-1 & Hα-15), 1.79 (1H, *brd*, *J* = 18 Hz, Hα-12), 1.84–1.92 (2H, *m*, Hα-1 & Hβ-12), 1.95–2.09 (4H, *m*, Hβ-6, Hβ-7, Hβ-15 & Hβ-16), 2.24 (1H, *td*, *J* = 16.5 & 4.5 Hz, Hβ-2), 2.34 (1H, *m*, H-8), 2.44 (1H, *dd*, *J* = 17.5 & 9 Hz, Hα-16), 2.55 (1H, *m*, Hα-6, overlapped with DMSO), 3.36 (1H, *m*, Hα-2, partially overlapped with H_2O from DMSO), 5.31 (1H, *d*, *J* = 5 Hz, H-11), 6.38 (1H, *s*, H-4), 6.78 (2H, *brs*, NH_2); ^{13}C-NMR (125 MHz, DMSO-d_6, δ / ppm): 220.0 (*s*, C-17), 172.9 (*s*, C=S), 160.6 (*s*, C-3), 156.5 (*s*, C-5); 146.1 (*s*, C-9), 121.3 (*d*, C-4), 116.1 (*d*, C-11), 47.7 (*d*, C-14), 45.1 (*s*, C-13), 40.4 (*s*, C-10), 36.2 (*d*, C-8), 35.6 (*t*, C-16), 33.5 (*t*, C-12), 32.6 (*t*, C-6), 32.5 (*t*, C-1), 30.9 (*t*, C-7), 25.9 (*q*, C-19), 24.3 (*t*, C-2), 22.1 (*t*, C-15), 13.7 (*q*, C-18).

Journal of the Serbian Chemical Society
JSCS-info@shd.org.rs • www.shd.org.rs/JSCS
J. Serb. Chem. Soc. *86* (5) 469–482 (2021)
JSCS–5435
Original scientific paper

QSAR studies of angiotensin converting enzyme inhibitors using CoMFA, CoMSIA and molecular docking

JIAN-BO TONG*, TIAN-HAO WANG, YI FENG and GUO-YAN JIANG

Shaanxi Key Laboratory of Chemical Additives for Industry, Shaanxi University of Science and Technology, Xi'an 710021, China

(Received 15 June, revised 31 July, accepted 4 November 2020)

Abstract: In order to better understand the biochemical interactions governing their activities in lowering blood pressure, multiple quantitative structure-activity relationship (QSAR) models were developed from a data set of 58 angiotensin converting enzyme (ACE) inhibitors. The models were built by using comparative molecular field analysis (CoMFA) and comparative molecular similarity indices analysis (CoMSIA) techniques. The best CoMFA model had a cross-validation q^2 value of 0.940, a non cross-validation r^2 value of 0.952 and an external validation statistic Q_{ext}^2 value of 0.920. For the best CoMSIA model the values were with $q^2 = 0.872$, $r^2 = 0.926$ and $Q_{ext}^2 = 0.868$. Based on the contour maps, eight new ACE inhibitors were designed. Molecular docking was employed to further explore the binding requirements between the ligands and the receptor protein which included several hydrogen bonds between the ACE inhibitors and active site residues. This study showed extensive interactions between ACE inhibitors and residues of HIS383, GLU384, HIS513, TYR520 and LYS511 in the active site of ACE. The design of potent new inhibitors of ACE can get useful insights from these results.

Keywords: ACE inhibitors; 3D-QSAR; new drug design; molecular docking.

INTRODUCTION

Angiotensin converting enzyme (ACE) inhibitors play a key role in the regulation of peripheral blood pressure, mainly through the renin-angiotensin and kallikrein-kinin system.[1] ACE has been considered as a target in the prevention and treatment of hypertensive diseases.[2] It is generally believed that the absorption of 2-3 peptides from the gastro-intestinal tract of single stomach mammals is an important physiological phenomenon.[3] Therefore, ACE inhibitors peptides obtained more attention from researchers.

The explosive growth of information has resulted from a diversity of peptide studies. It has been difficult for scientists to identify the target molecule from

* Corresponding author. E-mail: jianbotong@aliyun.com
https://doi.org/10.2298/JSC200615072T

among the thousands of candidate compounds.[4] Although the traditional experimental method is relatively accurate, it is labor-intensive, time-consuming and costly. Therefore, scientists have sought new ways to address this problem.

QSAR is a method that is used to investigate the quantitative relationship between a series of compounds of related structure (including 2D/3D molecular and electronic structures) and biological activity (such as pharmaceutical activity, toxicity, and pharmacodynamics properties) by using theoretical calculations and statistical analytic tools.[5] The CoMFA and CoMSIA are especially effective methods based on statistical techniques. The CoMFA method was introduced by Cramer in 1987 and is widely used in the present practice of drug discovery. The advantage of CoMFA is its use in predicting the biological activity of molecules, taking into account the steric/electrostatic properties and biological activities and displaying the results in the form of contour maps.[6] CoMSIA is a more recently developed technique introduced by Klebe in 1994 and considers five different physicochemical properties: steric, electrostatic, hydrophobic, hydrogen bond donor (H bond donor) and hydrogen bond acceptor (H bond acceptor). The advantage of this method is that it considers more types of interactions, particularly hydrophobicity of compounds, than does CoMFA.[7] The two methods sample the potential fields surrounding a set of ligands and construct QSAR models by correlating these 3D fields with a common target receptor.

There were some papers studying the related issues of ACE inhibitors. Compared with references,[8–11] this study chose a new system consisting of 58 ACE inhibitors dipeptides for research, compared with reference,[12] this study used a new QSAR method for research. The present study aimed to develop predictive models and evaluate what structural features (hydrogen bond donor/acceptor, hydrophobic, steric and electrostatic) were responsible for the bioactivity of peptides.[13,14] These fields were mapped onto the inhibitors' binding pocket of ACE protease in order to better understand these interactions. Eight analogs of ACE inhibitors were designed as ACE protease inhibitors based on the molecular modeling candidates that had the highest biological activity. Molecular docking was selected to illustrate the binding mode between the ligands and the protein receptor. Surflex-dock results showed extensive interactions between ACE inhibitors and residues.

MATERIALS AND METHODS

Preparation of data set

A total of 58 ACE inhibitors peptides were selected from the published literature.[15] Each peptide was listed in Table I with a reported in vitro IC_{50} (the peptide concentration required to produce 50 % inhibition of ACE) value that was less than 1 mM. Before building the model, all IC_{50} values were converted to pIC_{50} values (–log (IC_{50}/mmol L^{-1})). The structure and pIC_{50} values are shown in Table I. The whole data set was divided into two parts, a train-

ing set of 47 compounds that was used to construct the 3D-QSAR model and a test set of 11 compounds, that was used to evaluate capability of the model.

TABLE I. Amino acid sequences of 58 ACE inhibitors and their observed and predicted activities

No.	Peptide	pIC_{50}			No.	Peptide	pIC_{50}		
		Observed	Predicred				Observed	Predicted	
			CoMFA	CoMSIA				CoMFA	CoMSIA
1	VW	5.80	5.71	5.51	30	KG	2.49	2.38	2.54
2	IW	5.70	5.59	5.64	31	FG	2.43	2.40	2.50
3	IY	5.43	5.35	4.79	32	GS	2.42	2.35	2.25
4	AW	5.00	5.05	5.01	33	GV	2.34	2.61	2.54
5	RW	4.80	5.01	4.83	34	MG	2.32	2.20	2.28
6	VY	4.66	4.42	4.76	35	GK	2.27	2.28	2.11
7	GW	4.52	4.65	4.78	36	GE	2.27	2.31	2.16
8	VF	4.28	4.17	4.00	37	GT	2.24	2.47	2.39
9	AY	4.06	3.93	4.22	38	WG	2.23	2.21	2.22
10	IP	3.89	3.76	3.72	39	HG	2.20	2.28	2.23
11	RP	3.74	3.82	3.63	40	GQ	2.15	2.31	2.19
12	AF	3.72	3.69	3.55	41	GG	2.14	2.18	2.17
13	GY	3.68	3.58	3.95	42	QG	2.13	2.11	2.12
14	AP	3.64	3.68	3.39	43	SG	2.07	2.38	2.09
15	RF	3.64	3.46	3.36	44	LG	2.06	2.03	2.38
16	VP	3.38	3.76	3.68	45	GD	2.04	1.90	2.06
17	GP	3.35	3.57	3.46	46	TG	2.00	2.28	2.09
18	GF	3.20	3.34	3.21	47	EG	2.00	1.90	1.97
19	IF	3.03	3.09	4.02	48[a]	DG	1.85	2.05	1.93
20	VG	2.96	2.90	2.98	49[a]	PG	1.77	1.95	2.07
21	IG	2.92	2.80	3.00	50[a]	LA	3.51	3.15	2.53
22	GI	2.92	2.72	2.56	51[a]	KA	3.42	3.54	2.68
23	GM	2.85	2.91	2.73	52[a]	RA	3.34	3.50	2.41
24	GA	2.70	2.32	2.31	53[a]	YA	3.34	3.60	2.69
25	YG	2.70	2.45	2.54	54[a]	AA	3.21	3.56	2.64
26	GL	2.60	2.73	2.71	55[a]	FR	3.04	3.49	2.77
27	AG	2.60	2.44	2.49	56[a]	HL	2.49	2.90	2.80
28	GH	2.51	2.60	2.69	57[a]	DA	2.42	2.12	2.08
29	GR	2.49	2.26	2.53	58[a]	EA	2.00	2.00	2.13

[a]Test set

Molecular modeling and alignment

The 3D-QSAR study was performed on SYBYL X-2.0. The 3D structures of all molecules were constructed using the Build Protein function. Partial atomic charges of all compounds were calculated by the Gasteiger–Huckel method, and then optimized for their geometry using Tripos field with a distance-dependent dielectric function and energy convergence criterion of 0.005 kcal*/(mol Å) using the maximum iterations set to 1000.[16,17] The

* 1 kcal = 4184 J

predictive accuracy and the reliability of the associated contour maps of such CoMFA and CoMSIA models are directly dependent on the molecular alignment.

Generally speaking, the lowest energy conformer of the most active peptide was selected as a template peptide. Based on the common structure, the residual peptides were aligned. In general, geometric similarity exists between the structure and the bioactive conformation for 3D-QSAR. Since the predictive capability of the model is directly dependent on alignment of molecules, selecting the common molecule structure is one of the important steps in performing 3D-QSAR analyses.[18]

CoMFA and CoMSIA analysis

The CoMFA and CoMSIA methods were employed to construct the predictive 3D-QSAR model based on aligned peptide drugs. In the CoMFA analysis, steric and electrostatic fields were calculated on a 3D grid with a spacing of 2.0 Å in *x*, *y*, and *z* directions for each of the alignments[19]. A sp^3 carbon probe atom with a Lennard–Jones Coulomb radius of 1.52 Å and a charge of +1.00 was used as a probe to calculate the steric and electrostatic fields energy, respectively.[20] The cut-off value of steric and electrostatic fields was set to 30.0 kcal/mol. The St Dev* coefficients values as different weighing factors were performed to derive appropriate results. The model was used to get precise activity predictions of the untested compounds. The Lennard–Jones formula (1) and Coulomb formula (2) are as follows:

$$E_{\mathrm{vdW}} = \sum_{i=1}^{n} (A_j r_{ij}^{-12} - C_j r_{ij}^{-6}) \tag{1}$$

$$E_{\mathrm{C}} = \sum_{i=1}^{n} \frac{q_i q_j}{D r_{ij}} \tag{2}$$

For the CoMSIA analysis, similarity is expressed in terms of steric occupancy, electrostatic interactions, the standard settings of others at probe with charge +1, radius 1 Å, +1.0 for hydrophobic, hydrogen-bond donor and acceptor descriptors respectively.[21] CoMSIA can provide smooth and explicable contour maps using Gaussian-type distance dependence. In CoMFA and CoMSIA two or five descriptor fields are not totally independent of each other. CoMSIA calculates the similarity descriptors by way of a grid lattice. For a molecule *j* with atoms *i* at the grid point *q*, the CoMSIA similarity index AF is calculated by the equation (3):[22]

$$A_{\mathrm{F,K}}^{\mathrm{q}}(j) = -\sum_{i=1}^{n} w_{\mathrm{probe,k}} w_{i\mathrm{k}} e^{-a r_{i\mathrm{q}}^2} \tag{3}$$

where $w_{i\mathrm{k}}$ is the actual value of the physicochemical property k of atom *i*; $w_{\mathrm{probe,k}}$ is the property of the probe atom with a preset charge (+1 in this case), a radius (1.53 Å), and a hydrophobicity of 1; and $r_{i\mathrm{q}}$ is the mutual distance between the probe atom at grid point q and atom *i* of the molecule. In the CoMSIA calculations, five physicochemical properties (steric, electrostatic, hydrophobic, hydrogen bond donor, and hydrogen bond acceptor) were determined for all of the molecules.

Regression analysis by PLS method

In the present work, a partial least-squares (PLS) method, which is an extension of multiple regression analysis, was used to calculate the minimal set of grid points. And to correlate the CoMFA and CoMSIA fields to the experimental pIC_{50} values in order to generate the 3D--QSAR models. The leave-one-out (LOO) cross-validation was used to acquire the optimal number of components (*NC*) and the correlation coefficient (q^2).[23,24] The *NC* was then used to

produce the final QSAR model and to obtain the non-cross-validation correlation coefficient (r^2), standard error of estimate (*SEE*), the Fischer ratio value (F) and the contribution of steric (S) and electrostatic (E) fields. The CoMSIA model also can predict the contributions of hydrophobic (H), hydrogen bond donor (D) and hydrogen bond acceptor (A) fields. The CoMFA and CoMSIA results were then visually displayed in field contribution maps. Q_{ext}^2 indicates external validation statistics of the model. The q^2, formula (4), r^2, formula (5) and Q_{ext}^2, formula (6), are as follows:[25,26]

$$q^2 = 1 - \frac{\sum(Y_{obs} - Y_{pred})^2}{\sum(Y_{obs} - Y_{mean})^2} \quad (4)$$

$$r^2 = 1 - \frac{\sum(Y_{obs} - Y_{CVpred})^2}{\sum(Y_{obs} - Y_{mean})^2} \quad (5)$$

$$Q_{ext}^2 = 1 - \frac{\sum_{i=1}^{test}(Y_i - Y_{test})^2}{\sum_{i=1}^{test}(Y_i - Y_{trave})^2} \quad (6)$$

where Y_{mean} is the average activity value of the entire data set, while Y_{obs}, Y_{pred}, Y_{CVpred}, Y_{test} and Y_{trave} represent the observed values, predicted values, cross-validated activity values, test predicted activity values and training predicted activity values, respectively. High q^2, Q_{ext}^2 and r^2 values are considered to be indicators of the high predictive ability of the model.[27]

Molecular docking analysis

The research of the bonding between the enzyme and the ligands is meaningful for designing new drugs. The molecular docking investigations can explore the binding relationship between the ligands and the receptor protein.[28] In this paper, molecular docking was studied using Surflex-dock. The binding site was developed using the ACE X-ray with crystal structure (PDB ID: 1O86, www.rcsb.org) obtained from the RCSB Protein Data Bank. First, we analyzed the protein and fixed the side chains, and the terminal ends of the main chain. Then, 1O86 was prepared by adding hydrogen, adding charges, treating the terminal residues, and extracting the ligand.[29-31] Finally, the prototype molecule was generated. The molecule was docked into the active pocket.[32] The number of the maximum output poses was set as 20, and other set parameters were defaulted by SYBYL-X 2.0. The output poses were mainly evaluated by the total score.

RESULT AND DISCUSSION

CoMFA analysis of ACE inhibitors

The CoMFA and CoMSIA models were developed based on the set of 58 ACE inhibitors. The test set of 11 di-peptides (Table I) was employed to evaluate the reliability and applicability of the models. The most active peptide in the dataset was chosen as the template, *i.e.*, compound No. 1. The final superpositions of all peptides are displayed in Fig. 1.

Statistical parameters derived from the CoMFA model are summarized in Table II. The CoMFA model illustrates a cross-validated q^2 of 0.940, when using six components. The non-cross-validated PLS analysis resulted in a conventional r^2 = 0.952, Q_{ext}^2 = 0.920, F = 91.363, and *SEE* = 0.296. The values of pIC_{50}

predicted by CoMFA model are listed in Table I. A plot of calculated *versus* experimental activities for this model is shown in Fig. 2, which indicates the satisfactory predictive capability of the model. These data show that the performance of the model is moderately successful. The contributions of steric and electrostatic fields calculated by the CoMFA model are 74.4 and 25.6 % of variance, respectively, which indicates that steric fields make a slightly greater contribution in this model than do electrostatic.

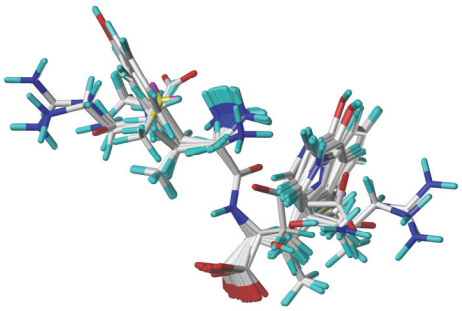

Fig. 1. The superpositions of peptides in the training and test sets of ACE inhibitors.

TABLE II. The statistical parameters for best 3D-QSAR models

Field	Parameter					Contribution				
	q^2	*NC*	r^2	*SEE*	*F*	*S*	*E*	*H*	*D*	*A*
					CoMFA					
SE	0.940	6	0.952	0.296	91.363	0.744	0.256	–	–	–
					CoMSIA					
SEHDA	0.825	6	0.946	0.263	117.074	0.184	0.122	0.291	0.251	0.152
SEHD	0.872	6	0.926	0.260	120.728	0.217	0.161	0.327	0.295	–

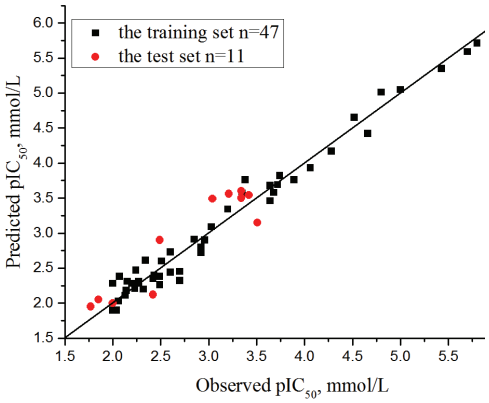

Fig. 2. Linear regression between experimental and predicted pIC_{50} values of ACE inhibitors.

The CoMFA analysis also gives contour plots of steric and electrostatic interactions. The steric interactions are represented by green-and yellow-colored contours in Fig. 3a. Bulky substituents in the regions shaded yellow are likely to

decrease biological activity, while bulky group substitutions in the green-colored regions are likely to enhance the activity. This is illustrated by the progressive reduction of activities of di-peptides in the series 25, 30 and 46 which have progressively smaller substituent volumes at the N-region. The same situation occurs in two other series of di-peptides, *i.e.*, 3, 6 and 13and 51, 53 and 24.

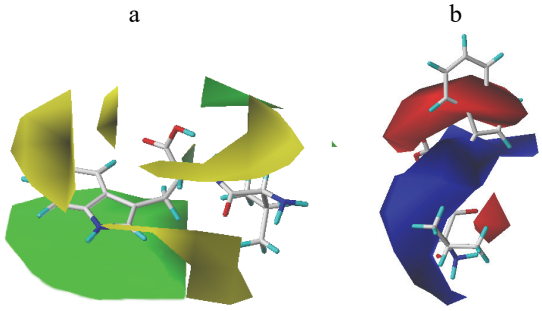

Fig. 3. CoMFA steric counter map (a) and electrostatic counter map (b).

Blue and red-colored contours in Fig. 3b represent the CoMFA electrostatic fields. Positively charged favorable blue regions are found around the N-terminal, while negatively charged favorable red regions are observed near the C-terminal, which could not indicate for its malposition. By comparing di-peptides 28, 29, 35 and 22, we see that the positive charge on the guanidino or ε-amino group of C-terminal Arg and His, as well as Lys side-chains, result in large reductions of potency. Overall, the CoMFA contour maps not only explain the QSAR of molecules, as reported, but also provide useful guidelines toward designing compounds for increased activity.

CoMSIA analysis for ACE peptides

The CoMSIA model was used to predict the activity of 58 ACE inhibitors. The best CoMSIA model was generated employing two alignment methods and different field combinations. There is no significant difference between the CoMSIA models developed by the database and field fit alignment methods. Therefore, the model generated by the database alignment that had a slightly higher cross-validated r^2 value was used for the final analysis. Based on this model, the correlation between experimental and predicted activity of all peptides is presented in Fig. 4, which indicate that there is no systematic error in the method. From Table II, the PLS analysis of the CoMSIA model was generated using steric, electrostatic, hydrophobic and hydrogen bond donor fields. It produced a cross-validated q^2 of 0.872 with an optimum number of six components and the corresponding non cross-validated r^2 = 0.926 with the *SEE* value = 0.260 and F =120.728.

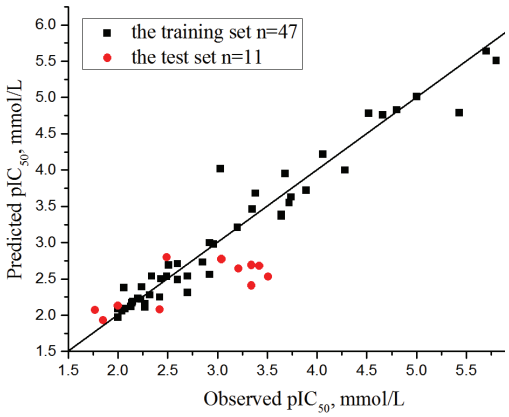

Fig. 4. Linear regression between experimental and predicted pIC_{50} values of ACE inhibitors by the best CoMSIA model.

The CoMSIA steric and electrostatic contour maps are shown in Fig. 5a and b.

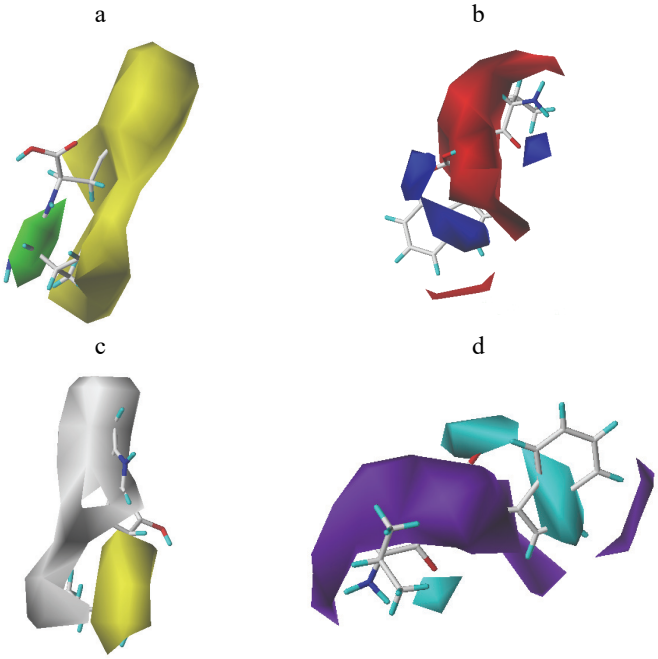

Fig. 5. CoMSIA contour maps: a) steric contour; b) electrostatic contour; c) hydrophobic contour; d) H-bond donor contour.

The contours are similar to the CoMFA steric and electrostatic contour maps. The CoMSIA hydrophobic contour map is shown in Fig. 5c. The yellow and gray contours indicate the regions where hydrophobic and hydrophilic groups are favored by the model, respectively. A large gray contour in the template molecule indicates that a change to a more a hydrophobic group will inc-

rease the activity, whereas the small yellow contour at the benzene ring indicates a position where a more hydrophilic group at this position will lead to increased activity. This trend is illustrated in the following series: 13 > 24; 51 > 52 > 24.

The CoMSIA hydrogen bond donor contour map is shown in Fig. 5d. The cyan contours represent the regions where hydrogen bond-donating groups increase the activity, whereas the purple contours represent the regions where hydrogen bond-donating groups decrease the activity. Fig. 5d shows purple contours around the C-terminal and N-terminal positions, indicating that a strong non-H bond donor group might increase the activity.

Drug molecular design

Based on the CoMFA and CoMSIA contour maps, we have designed 8 new compounds and predicted their activities using the CoMFA model. The structures and predicted activities (pIC_{50}) of 8 new compounds are displayed in Table III. The predicted activities of all the new compounds are higher than those of the training set molecules. This greater predicted activity may result from the fact that there is no bulky and electropositive substituent at the C-terminal position and a bulky substituent occupies the N-terminal of the molecules.

Table III. Structures and predicted pIC_{50} of newly designed molecules

No.	Structure	Predicted pIC_{50}
N1	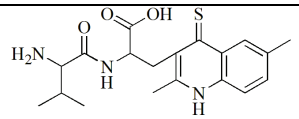	5.990
N2	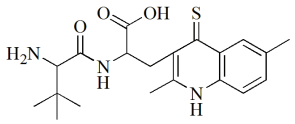	6.000
N3	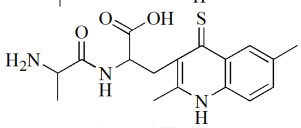	5.840
N4	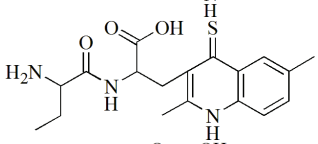	5.850
N5	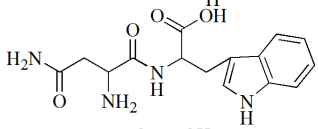	6.210
N6	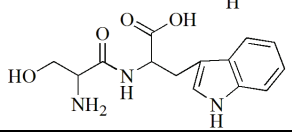	6.250

Table III. Continued

No.	Structure	Predicted pIC_{50}
N7	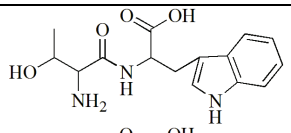	6.590
N8	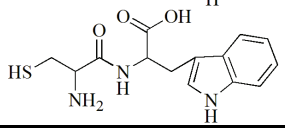	6.220

Docking study

Molecular docking study widely used to predict the potential binding mechanisms between the bioactive molecule and the target. In this study, Surflex--Dock was used to simulate the docking of ligands into the active site of target protein – renin. During this procedure, firstly, the selected ligand, A/LPR702, is extracted then all water molecules are removed, and finally the protein is hydrogenated. Aftar that the protomol (Fig. 6) is generated when the binding pocket is full of 3 molecular probes, *i.e.*, N–H, CH_4 and C=O, which represent hydrogen bond donor, hydrogen bond receptor, and hydrophobic sites, respectively.

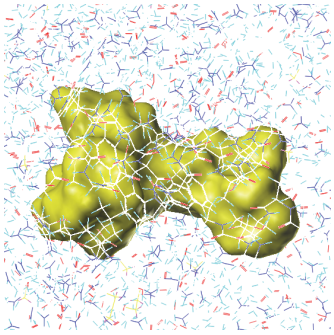

Fig. 6. Protomol (prototype molecule), which is generated when the binding pocket is full of 3 molecular probes, *i.e.*, N–H, CH_4 and C=O, respectively.

As shown in Fig. 7, compound No. 1 was selected to dock into the binding site of 1O86. The ligand is represented by sticks, the amino acid residues are represented by green lines, and the hydrogen bonds are represented by purple dotted lines. The compound No. 1 was the closest to these residues: ALA354, GLU384, HIS513, GLN281, TYR520 and LYS511. The distance between the hydrogen bonds formed by ALA354 is 1.588 Å (–O···H–), the distance between the hydrogen bonds formed by GLU384 is 2.065 Å (–O···H–), the distance between the hydrogen bonds formed by HIS513 is 2.065 Å (–N···H–), the distance between the hydrogen bonds formed by GLN281 is 2.053 Å (–H···O–), the distance between the hydrogen bonds formed by TYR520 is 1.876 Å (–H···O–),

the distance between the hydrogen bonds formed by LYS511 is 1.952 Å (–H···O–), respectively.

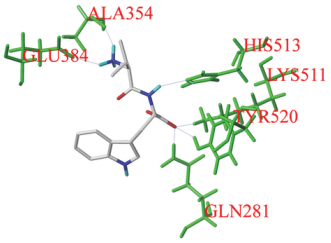

Fig. 7. The hydrogen-bond interaction between compound 1 and 1O86.

The total score containing crash score and polar score was total scoring function for the output pose of the molecules. In conclusion, the output pose was excellent when total score was more than 6.0. In this work, we used the total score method to screen the optimal pose. We have conducted molecular docking for the newly designed compounds and 1O86, then selected the results with the higher total score for analysis. The total-scores are shown in the Table IV. As shown in Fig. 8a–d, compounds N1, N5, N6 and N7 were docked into the active binding cavity of the ACE receptor.

Table IV. The results of molecular docking

No.	Total-score	Crash	Polar
N1	7.5498	–1.0749	4.4554
N2	6.8850	–2.2892	3.4409
N3	5.6833	–1.7477	3.4902
N4	6.9544	–1.3880	4.1844
N5	8.4445	–1.3372	7.0787
N6	7.5438	–0.8306	7.1443
N7	9.5820	–0.7493	7.4919
N8	7.0570	–0.6571	5.3465

In Fig. 8a, the designed new compound N1 has hydrogen-bonding interactions with HIS353, TYR523, GLU411, HIS387, HIS383 and GLU384. In Fig. 8b, the designed new compound N5 has hydrogen-bonding interactions with HIS513, TYR520, LYS511, GLN281, HIS353, ALA354, HIS387, HIS383 and GLU384. In Fig. 8c, the designed new compound N6 forms hydrogen-bonding interactions with GLN281, LYS511, HIS513, TYR520, ASP415, HIS383 and GLU384. In Fig. 8d, the designed new compound N7 forms hydrogen-bonding interactions with GLU384, GLN281, LYS511, TYR520, TYR523 and HIS513. Compound N7 has a high predicted activity (6.590) and high total-score value (9.5820), demonstrating that the compound is designed successfully.

The results showed that the ligand molecule has hydrogen bonding with the HIS383 residue, such as molecules N1, N5 and N6; the ligand molecule has hyd-

rogen bonding with the GLU384 residue, such as molecules N1, N5, N6 and N7; The ligand molecule has hydrogen bonding with the HIS513 residue, TYR520 residue and LYS511 residue, such as molecules N5, N6 and N7.

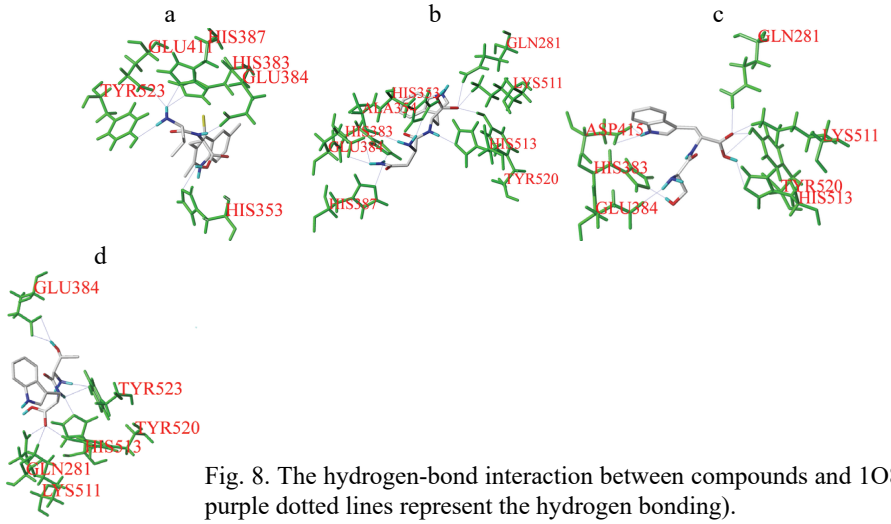

Fig. 8. The hydrogen-bond interaction between compounds and 1O86 (the purple dotted lines represent the hydrogen bonding).

All the newly designed compounds were docked in to 1O86, N3 had relatively low score value, so this compound is likely to be inappropriate. The docking results of the remaining new compounds N2, N4, and N8 with 1O86 were excellent, with the total score of 6.8850, 6.9544 and 7.0570, respectively, which showed that these docking conformations were useful to analyze as possible drug models.

CONCLUSION

In this study, 58 ACE inhibitors were studied using CoMFA and CoMSIA methods to generate 3D-QSAR models. Statistical parameters demonstrated that the established models are reliable and have a good internal and external predictive ability. The contour maps provide important relationships between structural features and inhibitory activities. Based on these contour maps, we designed new ACE inhibitors, all of which had higher activities than the training molecules. Finally, these new peptides and template molecules were used to simulate molecular docking. The results further indicated that the models are reliable and can be used to guide the development of new ACE inhibitor peptides.

Acknowledgements. This work was supported by the National Natural Science Foundation of China (21475081), the Natural Science Foundation of Shaanxi Province of China (2019JM-237), and the Graduate Innovation Fund of Shaanxi University of Science and Technology.

ИЗВОД

QSAR СТУДИЈЕ ИНХИБИТОРА АНГИОТЕНЗИН КОНВЕРТУЈУЋЕГ ЕНЗИМА КОРИСТЕЋИ CoMFA, CoMSIA И МОЛЕКУЛСКИ ДОКИНГ

JIAN-BO TONG, TIAN-HAO WANG, YI FENG и GUO-YAN JIANG

Shaanxi Key Laboratory of Chemical Additives for Industry, Shaanxi University of Science and Technology, Xi'an 710021, China

Да би се боље разумеле биохемијске интеракције које управљају њиховом активношћу у снижавању крвног притиска, развијен је модел вишеструке квантитативне релације сруктуре и активности (QSAR) на скупу података о 58 инхибитора ангиотензин конвертујућег ензима (ACE). Модели су изграђени користећи технике анализе компаративних молекулских поља (CoMFA) и индекса компаративне молекулске сличности (CoMSIA). Најбољи CoMFA модел има унакрсно валидацијску q^2 вредност 0,940, неунакрсно валидацијску r^2 вредност 0,952 и спољашњу статистичку ${Q_{\text{ext}}}^2$ вредност 0,920. За најбољи CoMSIA модел вредности су биле са q^2 = 0,872, r^2 = 0,926 и ${Q_{\text{ext}}}^2$ = 0,868. На основу контурних мапа дизајнирано је осам нових ACE инхибитора. Молекулски докинг је примењен да се даље истраже захтеви за везивање између лиганада и рецепторског протеина које укључују неколико водоничних веза између ACE инибитора и остатака везивног места. Ова студија је показала значајне интеракције између ACE инхибитора и остатака HIS383, GLU384, HIS513, TYR520 и LYS511 у активном месту ACE. Резултати могу пружити корисне увиде за синтезу снажних нових инхибитора ACE.

(Примљено 16. јуна, ревидирано 31. јула, прихваћено 4. новембра 2020)

REFERENCES

1. B. L. Wang, D. Q. Pan, K. L. Zhou, Y. Y. Lou, J. H. Shi, *Spectrochim. Acta, A* **212** (2019) 15 (https://doi.org/10.1016/j.saa.2018.12.040)
2. M. F. Sperry, H. L. A. Silva, C. F. Balthazar, E. A. Esmerino, S. Verruck, E. S. Prudencio, R. P. C. Neto, M. I. B. Tavares, J. C. Peixoto, F. Nazzaro, R. S. Rocha, J. Moraes, A. S. G. Gomes, R. S. L. Raices, M. C. Silva, D. Granato, T. C. Pimentel, M. Q. Freitas, A. G. Cruz, *J. Funct. Foods* **45** (2018) 435 (https://doi.org/10.1016/j.jff.2018.04.015)
3. M. Yamaguchi, S. Hirai, T. Sumi, Y. Tanaka, M. Tada, Y. Nishii, T. Hasegawa, H. Uchida, G. Yamada, A. Watanabe, H. Takahashi, Y. Sakuma, *Biochem. Biophys. Res. Commun.* **487** (2017) 613 (https://doi.org/10.1016/j.bbrc.2017.04.102)
4. Z. I. Abu Hasan, H. Williams, N. M. Ismail, H. Othman, G. E. Cozier, K. R. Acharya, R. E. Isaac, *Sci. Rep*. **7** (2017) 45409 (https://doi.org/10.1038/srep45409)
5. P. Patel, H. Rajak, *Med. Chem. Res.* **27** (2018) 2100 (https://doi.org/10.1007/s00044-018-2219-4)
6. J. B. Tong, S. S. Qin, S. Lei, Y. Wang, *J. Serb. Chem. Soc.* **84** (2019) 303 (https://doi.org/10.2298/JSC180904098T)
7. S. Avram, D. Duda-Seiman, F. Borcan, P. Wolschann, *J. Serb. Chem. Soc.* **76** (2011) 263 (https://doi.org/10.2298/JSC100806022A)
8. T. Potter, H. Matter, *J. Med. Chem.* **41** (1998) 478 (https://doi.org/10.1021/jm9700878)
9. F. F. Wang, B. Zhou, *Mol. Divers.* (2019) (https://doi.org/10.1007/s11030-019-10005-0)
10. W. L. Yan, G. M. Lin, R. Zhang, Z. Liang, L. X. Wu, W. J. Wu, *J. Mol. Liq.* **304** (2020) 112702 (https://doi.org/10.1016/j.molliq.2020.112702)
11. A. A. S. Juan, S. J. Cho, *Bull. Korean Chem. Soc.* **26** (2005) 952 (https://doi.org/10.5012/bkcs.2005.26.6.952)

12. S. S. Liu, C. S. Yin, Z. L. Li, S. X. Cai, *J. Chem. Inf. Comput. Sci.* **41** (2001) 321 (https://doi.org/10.1021/ci0003350)
13. W. L. Jiang, Q. H. Chen, B. Zhou, F. F. Wang, *Med. Chem. Res.* **28** (2019) 1974 (https://doi.org/10.1007/s00044-019-02428-z)
14. M. Shu, T. Wu, B. W. Wang, J. Li, C. M. Xu, Z. H. Lin, *Chin. J. Struct. Chem.* **38** (2019) 7 (https://doi.org/10.14102/j.cnki.0254-5861.2011-1917)
15. E. R. Collantes, W. J. Dunn, *J. Med. Chem*. **38** (1995) 2705 (https://doi.org/10.1021/jm00014a022)
16. H. Zhi, J. X. Zheng, Y. Q. Chang, Q. G. Li, G. C. Liao, Q. Wang, P. H. Sun, *J. Mol. Struct*. **1098** (2015) 199 (https://doi.org/10.1016/j.molstruc.2015.06.004)
17. R. M. Asath, T. N. Rekha, S. Premkumar, T. Mathavan, A. M. F. Benial, *J. Mol. Struct*. **1125** (2016) 633 (https://doi.org/10.1016/j.molstruc.2016.07.064)
18. A. D. Beirami, Z. Hajimahdi, A. Zarghi, *J. Biomol. Struct. Dyn.* **37** (2019) 2999 (https://doi.org/10.1080/07391102.2018.1502687)
19. L. L. Wu, Y. Z. Wang, Y. Liu, S. Y. Yu, H. Xie, X. J. Shi, S. Qin, F. Ma, T. Z. Tan, J. P. Thiery, L. M. Chen, *Oncotarget*. **5** (2014) 7677 (https://doi.org/10.18632/oncotarget.2291)
20. H. Khani, M. B. Sepehrifar, S. Yarahmadian, *Med. Chem. Res.* **26** (2017) 1184 (https://doi.org/10.1007/s00044-017-1828-7)
21. V. C. Pham, M. J. Choi, T. W. Kim, J. Kim, D. J. Choo, K. T. Lee, J. Y. Lee, *Bull. Korean Chem. Soc*. **33** (2012) 305 (https://doi.org/10.5012/bkcs.2012.33.1.305)
22. Y. D. Liu, Y. W. Xie, Y. Y. Liu, P. C. Wang, J. X. Ye, Y. L. Su, Z. H. Liang, Z. H. He, H. B. Zhou, G. C. Zhou, J. Xu, Y. Q. Chang, P. H. Sun, *Med. Chem. Res.* **28** (2019) 1796 (https://doi.org/10.1007/s00044-019-02416-3)
23. E. Pourbasheer, R. Aalizadeh, *SAR QSAR Environ. Res.* **27** (2016) 385 (https://doi.org/10.1080/1062936X.2016.1184713)
24. G. Bringmann, C. Rummey, *Cheminform*. **43** (2003) 304 (https://doi.org/10.1021/ci025570s)
25. A. Singh, S. Goyal, S. Jamal, B. Subramani, M. Das, N. Admane, A. Grover, *Struct. Chem*. **27** (2016) 993 (https://doi.org/10.1007/s11224-015-0697-2)
26. J. B. Bhonsle, D. Venugopal, D. P. Huddler, A. J. Magill, R. P. Hicks, *J. Med. Chem*. **50** (2007) 6545 (https://doi.org/10.1021/jm070884y)
27. S. Yu, P. Wang, Y. Li, Y. Liu, G. Zhao, *SAR QSAR Environ. Res*. **24** (2013) 819 (https://doi.org/10.1080/1062936X.2013.820792)
28. P. P. Roy, J. T. Leonard, K. Roy, *Chemometr. Intell. Lab*. **90** (2008) 31 (https://doi.org/10.1016/j.chemolab.2007.07.004)
29. C. Xu, Y. J. Ren, *Bioorg. Med. Chem. Lett*. **25** (2015) 4522 (https://doi.org/10.1016/j.bmcl.2015.08.070)
30. D. D. Huang, Y. L. Liu, B. Z. Shi, Y. T. Li, G. X. Wang, G. Z. Liang, *J. Mol. Graphics Model.* **45** (2013) 65 (https://doi.org/10.1016/j.jmgm.2013.08.003)
31. J. B.Tong, Y. Wang, S. Lei, S. S. Qin, *Chin. J. Struct. Chem.* **38** (2019) 464 (https://doi.org/10.14102/j.cnki.0254-5861.2011-2123)
32. X. Q. Yan, Z. C. Wang, Z. Li, P. F. Wang, H. Y. Qiu, L. W. Chen, X. Y. Lu, P. C. Lv, H. L. Zhu, *Bioorg. Medl. Chem. Lett.* **25** (2015) 4664 (https://doi.org/10.1016/j.bmcl.2015.08.026).

Journal of the Serbian Chemical Society
JSCS-info@shd.org.rs • www.shd.org.rs/JSCS
J. Serb. Chem. Soc. *86* (5) 483–494 (2021)
JSCS–5436
Original scientific paper

The spectral study of azo dye and cationic surfactant interaction in ethanol–water mixture

NEELAM SHAHI[1], SUJIT KUMAR SHAH[1], AMAR PRASAD YADAV[2] and AJAYA BHATTARAI[1]*

[1]*Department of Chemistry, M.M.A.M.C., Tribhuvan University, Biratnagar, Nepal and* [2]*Central Department of Chemistry, Tribhuvan University, Kirtipur, Nepal*

(Received 16 November 2020, revised 10 March, accepted 11 March 2021)

Abstract: The interaction of the azo dye methyl red (MR) with dodecyl trimethyl ammonium bromide (DTAB) has been studied by the spectrometric methods through the azo-hydrazone tautomeric behaviour of MR for a series of the ethanol–water system (0.1, 0.2, 0.3 and 0.4 volume fractions of ethanol) at room temperature. The critical micelle concentration was determined using the conductometric technique with the increased ethanol volume, influenced by the solvent polarity and the architectural flexibility of methyl red. The azo form of methyl red brings the electrostatic interaction with the cationic surfactant through the adsorption phenomenon. The binding parameters were calculated with the aid of a modified Benesi–Hildebrand equation.

Keywords: molar absorptivity; binding constant; standard Gibbs energy.

INTRODUCTION

The performance of the interaction between dye and surfactant is one of the basic requirements for understanding the dyeing process and textile finishing.[1–5] In order to study this process numerous researches have been performed by the selective research techniques to access the basic information of the interactions for the process of the molecular complex formation in the dye-surfactant ion pair.[6–11]

There are no specified studies about the azo dye methyl red with cationic surfactant dodecyl trimethyl ammonium bromide, using various methods.[12–17] The absorbance peak of methyl red was decreased, due to the photodegradation in water. It was checked after 10, 20 and 35 min (complete photodegradtion) by the kinetic analysis treatment, which is based on the azo dye photosensitization.[18] The anchoring position of the –COOH group at the para position of methyl red tuned the wavelength and intensity[19] and showed a broad peak at 519 nm in

* Corresponding author. E-mail: bkajaya@yahoo.com
https://doi.org/10.2298/JSC201116020S

hydrazone form, indicating the considerable optical nonlinearities.[20] The visible spectrum of MR in aqueous solutions is marked by the overlap of a principal peak at 520±15 nm and a shoulder peak at 435±20 nm, for the hydroazo (acidic) and the azo (alkaline) species respectively.[21]

In this paper, the spectrophotometric study of the interaction between azo dye methyl red (MR) (Fig. 1) and cationic surfactant dodecyl trimethyl ammonium bromide (DTAB) (Fig. 2) is described.

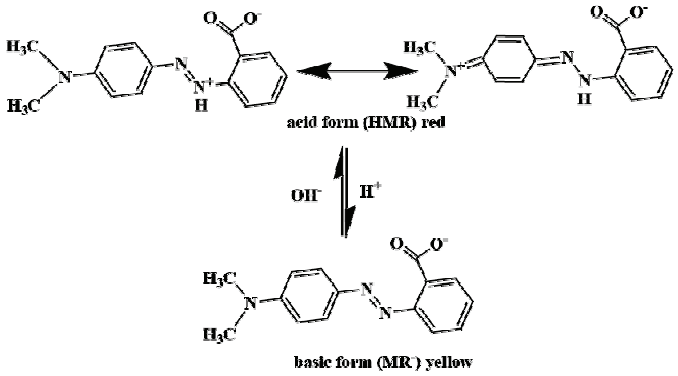

Fig. 1. Acid and basic forms of methyl red.

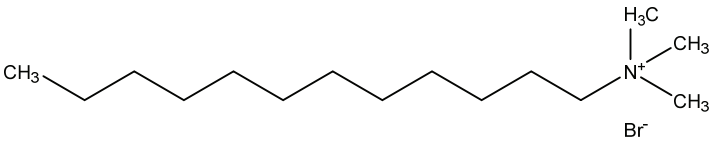

Fig. 2. Dodecyl trimethyl ammonium bromide.

The interaction between dye and surfactant plays an important role in the formation of the complex as shown in Fig. 3.

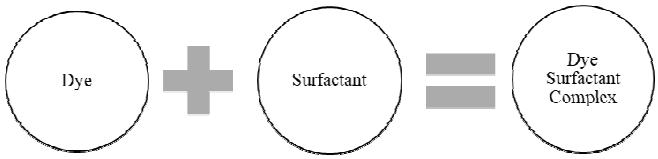

Fig. 3. The interaction between dye and surfactant for their complex formation.

To study the significance of theinteraction of the molecular complex formation of the azo dye–cationic surfactant ion pair, the absorbance measurement was performed for the series of the ethanol–water systems containing the various volumes of ethanol (0.1, 0.2, 0.3 and 0.4 volume fractions of ethanol). A modified model was applied in order to determine the binding constants and the change of standard Gibbs energy of binding for the molecular complex formation

of the ion pair. The result displayed the influence of volume fraction of ethanol on the formation of dye–surfactant molecular complex and the importance of the interaction of azo dye and cationic surfactant.

Methyl red is a good example which illustrates that both the linear and non-linear optical properties can be seen through the absorbance technique. The literature shows the azo-hydrazone tautomerism of MR, with the change of surfactant charge effects and without the change in solvent polarity, generates the azo-hydrazone tautomerism as shown in Fig. 1.[14,20,21] The optical sensitivity of azo dye makes the interaction study interesting with a cationic surfactant.[14] The interaction of the azo dye and the cationic surfactant brings the flexibility in absorbance which alters the nature of spectra.[12,13]

The present study describes the azo-hydrazone tautomerism, using the absorbance techniques along with the observation of binding constant and the change of Gibbs energy of binding of DTAB on MR, which will facilitate the advancement in the molecular design of similar derivatives, specifically a –COOH group azo dye through the photosensitized system in optical tenability. We applied a spectrophotometric technique and used the modified Benesi-Hildebrand equation in order to calculate the binding constant of methyl red, in the presence of DTAB/ethanol/water system. Such a concept was applied to calculate the binding parameters (the binding constant and the change of standard Gibbs energy of binding) for dyes (methylene blue and methyl orange) absorbance in DTAB–SDS mixed surfactant, by the absorption technique in an aqueous medium, without using critical micelle concentration (*CMC*) values.[22]

EXPERIMENTAL

Chemicals

DTAB and MR were obtained from Loba Chemicals, India. Similarly, MR (95 %) was purchased from Ranbaxy, India, and used without purification and spectroscopy quality ethanol was obtained from Merck, India.

Preparation of solutions

Four types of solutions were prepared to study the interaction of MR–DTAB in the ethanol–water system.

In the first part of the study, 0.1, 0.2, 0.3 and 0.4 volume fractions of ethanol–water mixed solvent were prepared. Sequentially the surfactant (DTAB, concentration ranging from 10^{-4} to 0.12 mol L^{-1} and the azo dye MR at a constant concentration of 2.97×10^{-4} mol L^{-1} were prepared separately in the respective volume fraction of ethanol–water. In the second part of the study, the spectral absorbance corresponding to wavelengths ranging from 300 to 700 nm of the solution at variable concentrations of DTAB, with a constant dye concentration of MR, was obtained for the interaction study.

Methods

The spectrophotometric measurements were recorded by a single beam microprocessor UV–Vis spectrophotometer (LT-290 Model, India) from which UV–Vis spectra were registered at room temperature using 1 cm length quartz cuvette. The conductometric measure-

ments were performed in order to obtain the *CMC* value of DTAB in the absence, as well as the presence of MR at 0.1,0.2,0.3 and 0.4 volume fraction of ethanol, as described in the literature.

RESULTS AND DISCUSSION

UV – Vis spectra of azo dye in ethanol – water mixture

The UV–Vis spectra of MR in the ethanol-water mixture (from 0.1 to 0.4 volume fractions of ethanol) were measured at the constant dye concentration ($C_{dye} = 2.97\times10^{-4}$ mol/L^{-1}). When the graph displaying the relation between absorbance (A) and wavelength (λ) was plotted (Fig. 4) the redshift was observed, from 0.4 to 0.2 volume fraction of ethanol, which was due to an increase in the dielectric constant and the reduction of solubility.[23] But the redshift between 0.1 and 0.2 volume fraction of ethanol were not observed. The absorbance spectra of MR at 0.1 volume fraction of ethanol showed two broad peaks at λ_{abs} of 532 and 529 nm. However, the absorbance spectra of MR showed a slight redshift with broad peaks at λ_{abs} of 528, 529 and 532 nm for 0.4, 0.3 and 0.2 volume fraction of ethanol, respectively. The observed peaks of MR as hydrazone (acidic) species were found at 0.1, 0.2, 0.3 and 0.4 volume fraction of ethanol. Thus, the UV–Vis spectra of methyl red were found to be solvent-dependent and the absorbance of methyl red in 0.4 volume fraction of ethanol is largest among 0.3, 0.2, 0.1 volume fraction of ethanol (Table I).

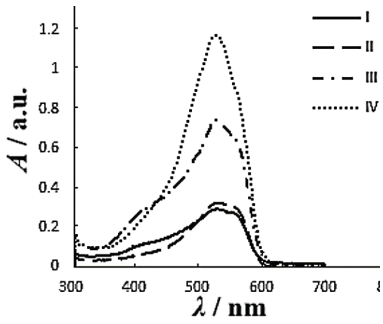

Fig. 4. Visible spectra of MR at various volume fractions of ethanol. Here, I, II, III and IV represent volume fraction of ethanol: 0.1, 0.2, 0.3 and 0.4, respectively.

TABLE I. The calculation for ε_0 from Eq. (4)

Volume fraction of ethanol	λ_{max} / nm	A / a. u.	ε_0 / L mol^{-1}cm^{-1}
0.1	532	0.2938	989.22
0.2	532	0.3268	1100.34
0.3	529	0.7428	2501.01
0.4	528	1.1798	3972.39

UV – Vis spectra of cationic surfactant – azo dye interactions in ethanol – water mixture

The UV–Vis spectra of MR in ethanol–water–DTAB were observed at constant dye concentration. When the graph (Fig. 5) was plotted (absorbance *vs.* wavelength), the absorbance peak of MR in ethanol–water–DTAB showed a broad absorbance peak at λ_{abs} of 419, 424, 421 and 420 nm for 0.1, 0.2, 0.3 and 0.4 volume fraction of ethanol, respectively. The peak range is attributed to the azo form of MR within ethanol–water–DTAB. The blue shift is observed for the constant dye concentration at the variable concentration of DTAB for the spectra of 'V' of legend represented in Fig. 5 – A, B, C and D were due to the formation of H-aggregates during the electrostatic interaction in the molecular complex (Fig. 3).[24]

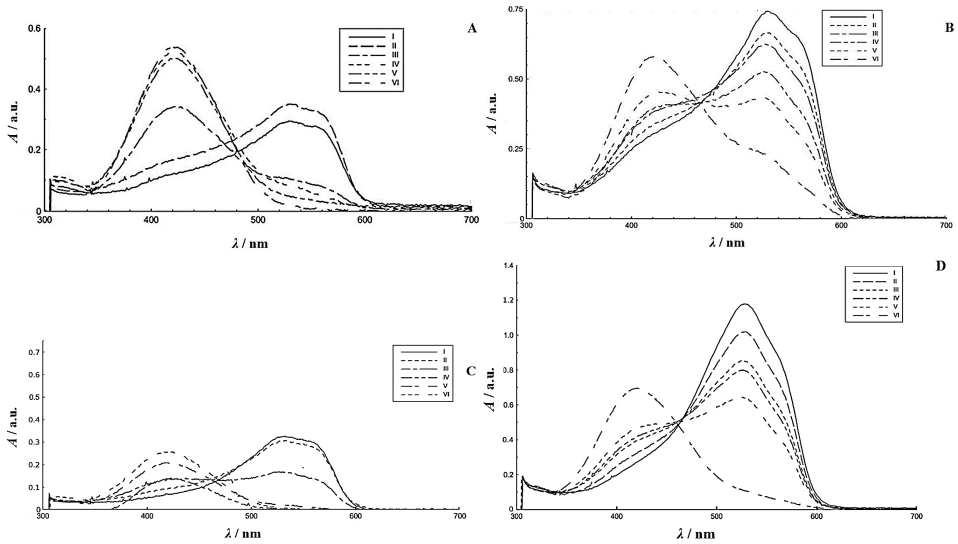

Fig. 5. Absorption spectra for methyl- red with presence and absence of DTAB; volume fraction of ethanol: 0.1 (A); 0.2 (B); 0.3 (C); 0.4 (D).

In the recent study, the interaction of CTAB (cationic surfactant) with MR is attributed to the azo form at λ_{abs} of 414 nm, whereas the interaction of AOT (anionic surfactant) with MR is subjected to the hydrazone form at λ_{abs} = 519 nm.[14]

In the present work, the interaction of cationic surfactant (DTAB) with the azo dye (MR) is studied through the spectrophotometric method. In the case of MR, due to its photoisomerisation, its azo(basic) form attracts the ionized surface-active agents. The ionic surfactants dissociate as electrolytes (weak or strong) which shows the adsorption phenomenon. The idealized charged spherical micelles are partially neutralized by the counterions forming the stern layer as shown in Fig. 6. The long alkyl groups of surfactants are in the interior of the micelle and the hydrophilic (polar) part of surfactants are at the surface, which exhibits the electrostatic interaction with the counterions of azo dye. Due to such

interactions, approximately 60–80 % micellized charge is neutralized by counterions and the remaining unbounded counterions are moving freely, forming the Gouy–Chapman double layer.

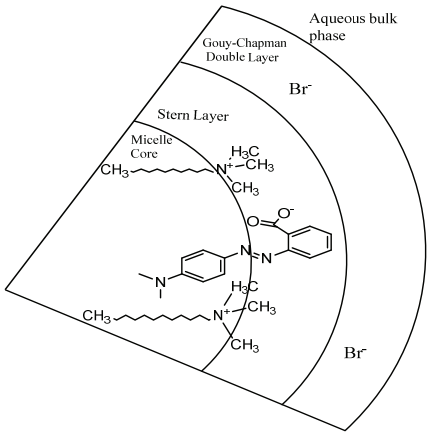

Fig. 6. A schematic structure of cationic surfactant with azo dye.[27]

We observed the interaction through different spectral behaviour and the obtained absorbance concerning the constant concentration of azo dye in the absence and the presence of a variable concentration of DTAB, for the series of the ethanol–water mixture, at room temperature.[25]

The spectral characteristics of azo dye were greatly influenced by the addition of cationic surfactant in the presence of various ethanol concentrations. The absorbance was increased with rised ethanol volume (Fig. 4), which contributes to the formation of molecular complex between the cationic surfactant and the azo dye as presented in Fig. 6. The origin of electrostatic interaction on the hydrocarbon core of the surfactant, at constant dye concentration, was analysed due to a decrease in absorbance with a higher concentration range of ionic surfactant.[26]

Various natures of absorption spectra of a dye with the presence and absence of cationic surfactant had been observed for the series of the ethanol–water mixtures as shown in Fig. 5.

Absorption spectra in Fig. 5A. In 0.1 volume fraction of ethanol, as the concentration of DTAB increased the MR band intensity initially increased and finally decreased. Here, I, II, III, IV, V and VI represents the DTAB concentrations (C/mol L^{-1}), which were varied from as 0, 0.011695, 0.023390, 0.035085, 0.046780 and 0.116951, respectively.

The absorption spectra in Fig. 5B. In 0.2 volume fraction of ethanol, as the concentration of DTAB increased the MR band intensity initially decreased and then increased. Here, I, II, III, IV, V and VI represents the DTAB concentrations

(C/mol L^{-1}), which were varied from as 0, 0.0105994, 0.0211988, 0.0317982, 0.0423976 and 0.1059940, respectively.

The absorption spectra in Fig. 5C and D. In 0.3 and 0.4 volume fraction of ethanol, as the concentration of DTAB increased the MR band intensity decreased. Here, in the case of Fig 5C, I, II, III, IV, V and VI represent DTAB concentrations (C/mol L^{-1}), which were varied as 0, 0.011122, 0.022244, 0.033366, 0.044488 and 0.111220, respectively. In the case of Fig 5D, I, II, III, IV, V and VI represent DTAB concentrations (C/mol L^{-1}), which were varied as 0, 0.011122, 0.022244, 0.033366, 0.044488 and 0.111220, respectively.

Analysis of cationic surfactant – azo dye interactions in ethanol – water mixture

We used the spectrophotometric technique and confirmed the surfactant induced spectral change by binding and thermodynamic properties, evaluated through the spectral changes, as the observed absorbance at different surfactant concentrations at constant dye concentration in the ethanol-water mixture, Fig. 5.

Shah *et al.*[28] investigated the CMC of DTAB in the ethanol–water mixture up to 0.6 volume fraction of ethanol using conductometry and tensiometry. The *CMC* was found to be increased up to 0.4 volume fraction of ethanol due to a decrease in hydrophobic character, with the addition of ethanol and the decrease in *CMC* up to 0.6 due to entrance of alcohol molecules into a micellar core. We used the conductometry technique to obtain the *CMC* value of DTAB in the absence, as well as in the presence of MR, at 0.1, 0.2, 0.3 and 0.4 volume fraction of ethanol. The sequential increased *CMC* is obtained in the adopted system, but the *CMC* values are suppressed with MR, in comparison to *CMC* values in the absence of MR.[28,29] The decreased *CMC*s of DTAB, in the presence of MR is due to the change in the status of the molecular complex system.[29] The *CMC* values are listed the in Table II along with literature.[28]

TABLE II. *CMC* values of DTAB in the presence and absence of MR at 298.15 K

Volume fraction of ethanol	*CMC* / mol L^{-1}		
	With MR	Without MR	Without MR[28]
0.1	0.01497	0.01637	0.0151
0.2	0.02102	0.02178	0.0214
0.3	0.02110	0.03054	0.0325
0.4	0.02487	0.04375	0.0462

It can be seen that both the conductivity and *CMC* of DTAB decrease with the addition of MR, as it is presented in Fig. 7, with is in agreement with the literature.[30]

The interaction between the dye and micellized surfactant can be described by the Eq. (1). Here, the term D, S, DS and K_b represent the dye, surfactant, dye––surfactant associate and binding constant, respectively:

$$D + S \xleftrightarrow{K_b} DS \quad (1)$$

Fig. 8 displays for the interaction study for the determination of the binding constant (K_b), related to the scheme on Fig. 6, which is calculated using the modified Benesi–Hildebrand Equation (2):[22]

$$\frac{D_T}{\Delta A} = \frac{1}{(\varepsilon_m - \varepsilon_0)} + \frac{1}{K_b(\varepsilon_m - \varepsilon_0)C_s} \quad (2)$$

$$\Delta A = A - A_0 \quad (3)$$

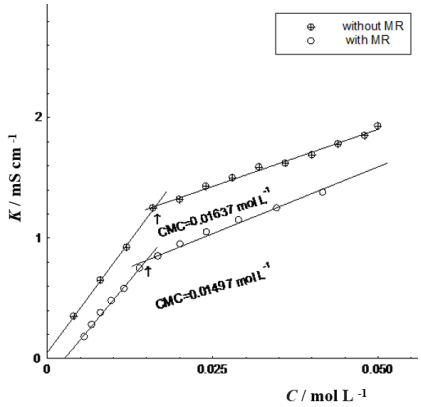

Fig. 7. Conductivity *versus* concentration of DTAB at 0.1 volume fraction of ethanol with and without MR.

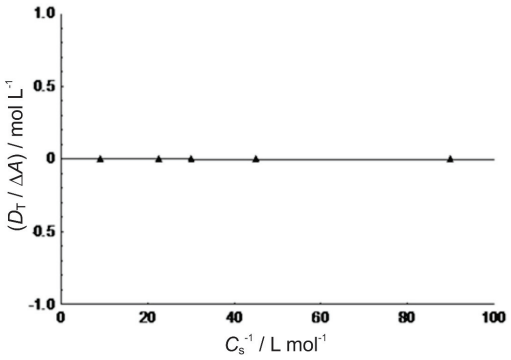

Fig. 8. The plot of ($D_T/\Delta A$) against reciprocal of C_s for MR with DTAB at 0.3 volume fraction of ethanol. Here, $y = 3.19\times10^{-5}x - 8.54\times10^{-4}$; Max. dev. $6.05\ 10^{-9}$, $r^2 = 1.00$.

The term D_T in Eq. (2) and A in Eq. (3) represents the concentration and the absorbance of dye. The left side of Eq. (2) consists of ΔA, which is the difference between the absorbance of dye in the presence and the absence of DTAB is expressed in Eq. (3). The right side of Eq. (2) consists of term ε_m, ε_0, C_s and K_b which represents the molar absorptivity of the dye, the molar absorptivity of dye fully bound to micelles, the concentration of DTAB (surfactant) and the binding constant respectively. Eq. (2) can be applied for studying spectral behaviour containing *CMC* value,[29] or without *CMC* value.[22] The molar absorptivity of dye

represented as ε_0 was calculated using the relation the rearranged Beer–Lambert Equation (4):

$$\varepsilon_0 = \frac{A}{LC} \tag{4}$$

The Eq. (4) term consists of terms A, L and C, which represents the absorbance for a given wavelength, the length of cuvette and the concentration of dye, respectively.

The maximum wavelength corresponding to absorbance (λ_{max} / nm), absorbance for a given wavelength (A / a.u.), length of the cuvette (L / cm), the concentration of dye (D_T / mol L^{-1}) , and molar absorptivity of dye (ε_0 / L mol^{-1} cm^{-1}) are the values and its interactive relationship are represented in Table I. Here, L = 1 cm, $C = 2.97\times10^{-4}$ mol L^{-1}. It can be seen that the highest molar absorptivity of azo dye at 0.4 volume fraction of ethanol is due to the influence of a higher volume of ethanol in water.[24]

The binding constant (K_b) can be determined by plotting ($D_T/\Delta A$) against reciprocal of C_s for DTAB, with MR at 0.3 volume fraction of ethanol, as shown in Fig. 8, as a typical example. From the slope and the intercept, the binding constant was calculated at a different volume fractions of ethanol and tabulated in Table III.

TABLE III. Calculation of the slope, intercept and binding constant in the different volume fractions of ethanol

Volume fraction of ethanol	Slope×10^5	Intercept×10^4	K_b / L mol^{-1}
0.1	6.22	7.59	12.2
0.2	1.3.3	6.48	4.87
0.3	3.19	8.54	26.77
0.4	1.48	2.96	20.00

Table III shows that the binding values, which were highest at the volume fraction of ethanol is 0.3, increased which is because the hydrophilic head portion of surfactants plays a significant role in dye-surfactant interaction.[31] When the volume of ethanol is 0.2, the binding value between the azo dye and the surfactant is lowest, due to the abnormal aggregation around the hydrophilic portion of DTAB micelles by MR molecules.

Many researchers had reported that the addition of mixed solvent completely blocks the micellization behaviour of surfactant at a certain concentration level of mixed solvent.[29]

The thermodynamic parameter, the change of standard Gibbs energy of binding can be obtained using Eq. (5):

$$\Delta G^{\ominus} = -RT\ln K_b \tag{5}$$

In Eq. (5), the left side represents the change of standard Gibbs energy of binding, $\Delta G^{\ominus}$, whereas, on the right side, R represents a universal gas constant, the recorded room temperature of the laboratory is denoted by T and K_b is the binding constant. The values are presented in Table IV, which indicates the interaction between the dye and ionic surfactant, at 0.1, 0.2, 0.3 and 0.4 volume fractions. This is due to the strong electrostatic interaction between the hydrophilic cationic head of surfactant and azo dye as well as with a decrease in the dielectric constant with the addition of mixed solvent.[30,32]

TABLE IV. Calculation of $\Delta G^{\ominus}$ in the different volume fractions of ethanol

Volum fraction of ethanol	$\Delta G^{\ominus}$ / kJ mol^{-1}
0.1	–6010.31
0.2	–3803.77
0.3	–7898.50
0.4	–7197.98

CONCLUSION

Based on the spectral study of the interaction between the azo dye MR and the cationic surfactant DTAB, the following conclusions can be summarized.

The spectrophotometric technique is the best method for the study of the dye–surfactant interaction, by a wide range of spectral analysis, with typical azo-hydrazone tautomerism in the ethanol–water mixture. The variable absorbance values ultimately indicated the scheme of dye–surfactant interaction through the adsorption phenomena and the formation of a dye surfactant complex. The interaction behaviour was studied through thermodynamic processes, which were characterized by the variable binding constant and the change of standard Gibbs energy of binding. The mixed solvent media containing alcohol–water mixtures broke down the structure of water, which lowered down the dielectric constant and hence *CMC* of DTAB increases, with the addition of ethanol in water, while *CMC* values of DTAB decrease with the presence of methyl red.

Acknowledgement. This work was supported by the University Grants Commission, Sanothimi, Bhaktapur, Nepal, under the funding award no. PhD-75/76-S&T-05.

И З В О Д

СПЕКТРОСКОПСКО ИСПИТИВАЊЕ ИНТЕРАКЦИЈЕ АЗО БОЈЕ И КАТЈОНСКОГ СУРФАКТАНТА У СМЕШИ ЕТАНОЛ–ВОДА

NEELAM SHAHI[1], SUJIT KUMAR SHAH[1], AMAR PRASAD YADAV[2] и AJAYA BHATTARAI[1]

[1]*Department of Chemistry, M.M.A.M.C., Tribhuvan University, Biratnagar, Nepal и* [2]*Central Department of Chemistry, Tribhuvan University, Kirtipur, Nepal*

Интеракција азо боје метил-црвена (MR) и додецилтриметиламонијум-бромида (DTAB) је спектроскопски испитивана праћењем азо-хидразон таутомерног понашања MR за серију смеша етанол–вода (запреминске фракције етанола: 0,1, 0,2, 0,3 и 0,4) на собној температури. Критична мицеларна концентрација је одређивана кондуктометријски, и

са повећањем запремине етанола на њу утиче поларност растварача и структурна флексибилност MR. Азо облик MR се адсорбује на сурфактанту електростатичким интеракцијама. Параметри везивања су израчунати применом Бенеси–Хилдебранд (Benesi–Hildebrand) једначине.

(Примљено 16. новембра 2020, ревидирано 10 марта, прихваћено 11. марта 2021)

REFERENCES

1. G. Kyzas, E. Peleka, E. Deliyanni, *Materials* **6** (2013) 184 (https://doi.org/10.3390/ma6010184)
2. A. Bhattarai, A. K. Yadav, S. K. Sah, A. Deo, *J. Mol. Liq.* **242** (2017) 831 (https://doi.org/10.1016/j.molliq.2017.07.085)
3. A. Pal, A. Garain, D. Chowdhury, M. H. Mondal, B. Saha, *Tenside Surfact. Det.* **57** (2020) 401 (https://doi.org/10.3139/113.110700)
4. S. Tunç, O. Duman, B. Kancı, *Dyes Pigments* **94** (2012) 233 (https://doi.org/10.1016/j.dyepig.2012.01.016)
5. K. M. Sachin, S. A. Karpe, M. Singh, A. Bhattarai, *Roy. Soc. Open Sci.* **6** (2019) 181979 (https://doi.org/10.1098/rsos.181979)
6. S. Fazeli, B. Sohrabi, A. R. Tehrani-Bagha, *Dyes Pigments* **95** (2012) 768 (https://doi.org/10.1016/j.dyepig.2012.03.022)
7. H. Akbaş, Ç. Kartal, *Spectrochim. Acta, A* **61** (2005) 961 (https://doi.org/10.1016/j.saa.2004.05.025)
8. S. Malik, A. Ghosh, P. Sar, M. H. Mondal, K. Mahali, B. Saha, *J. Chem. Sci.* **129** (2017) 637 (https://doi.org/10.1007/s12039-017-1276-4)
9. M. F. Nazar, S. S. Shah, M. A. Khosa, *J. Surfact. Deterg.* **13** (2010) 529 (https://doi.org/10.1007/s11743-009-1177-8)
10. M. H. Mondal, S. Malik, B. Saha, *Tenside Surfact. Det.* **54** (2017) 378 (https://doi.org/10.3139/113.110519)
11. M. Mondal, M. Ali, A. Pal, B. Saha, *Tenside Surfact. Det.* **56** (2019) 516 (https://doi.org/10.3139/113.110654)
12. S. Biswas, A. Pal, *Talanta* **206** (2020) 120238 (https://doi.org/10.1016/j.talanta.2019.120238)
13. F. Ahmadi, M. A. Daneshmehr, M. Rahimi, *Spectrochim. Acta, A* **67** (2007) 412 (https://doi.org/10.1016/j.saa.2006.07.033)
14. S. Sharifi, M. F. Nazar, F. Rakhshanizadeh, S. A. Sangsefedi, A. Azarpour, *Opt. Quantum Elec.* **52** (2020) (https://doi.org/10.1007/s11082-020-2211-3)
15. C. Hahn, A. Wokaun, *Langmuir* **13** (1997) 391 (https://doi.org/10.1021/la9603378)
16. S. Chanda, K. Ismail, *IJC A* **48** (2009) 775 (http://nopr.niscair.res.in/handle/123456789/4686)
17. M. H. Mondal, S. Malik, A. Roy, R. Saha, B. Saha, *RSC Adv.* **5** (2015) 92707 (https://doi.org/10.1039/c5ra18462b)
18. R. B. Narayan, R. Goutham, B. Srikanth, K. P. Gopinath, *J. Environ. Chem. Eng.* **6** (2018) 3640 (https://doi.org/10.1016/j.jece.2016.12.004)
19. L. Zhang, J. M. Cole, P. G. Waddell, K. S. Low, X. Liu, *ACS Sustain. Chem. Eng.* **1** (2013) 1440 (https://doi.org/10.1021/sc400183t)
20. D. N. Christodoulides, I. C. Khoo, G. J. Salamo, G. I. Stegeman, E. W. Van Stryland, *Adv. Opt. Photonics* **2** (2010) 60 (https://doi.org/10.1364/aop.2.000060)
21. M. R. Plutino, E. Guido, C. Colleoni, G. Rosace, *Sens. Actuators, B* **238** (2017) 281 (https://doi.org/10.1016/j.snb.2016.07.050)

22. K. M. Sachin, S. A. Karpe, M. Singh, A. Bhattarai, *Heliyon* **5** (2019) e01510 (https://doi.org/10.1016/j.heliyon.2019.e01510)
23. A. A. Rafati, S. Azizian, M. Chahardoli, *J. Mol. Liq.* **137** (2008) 80 (https://doi.org/10.1016/j.molliq.2007.03.013)
24. M. S. Ramadan, N. M. El-mallah, G. M. Nabil, M. Sherif, *J. Dispers. Sci. Technol.* **40** (2018) 1 (https://doi.org/10.1080/01932691.2018.1496837)
25. K. K. Karukstis, J. P. Litz, M. B. Garber, L. M. Angell, G. K. Korir, *Spectrochim. Acta, A* **75** (2010) 1354 (https://doi.org/10.1016/j.saa.2009.12.087)
26. M. L. Moyá, A. Rodríguez, M. del Mar Graciani, G. Fernández, *J. Colloid Interf. Sci.* **316** (2007) 787 (https://doi.org/10.1016/j.jcis.2007.07.035)
27. M. E. D. Garcia, A. Sanz-Medel, *Talanta* **33** (1986) 255 (https://doi.org/10.1016/0039-9140(86)80060-1)
28. S. K. Shah, S. K. Chatterjee, A. Bhattarai, *J. Mol. Liq.* **222** (2016) 906 (https://doi.org/10.1016/j.molliq.2016.07.098)
29. K. Edbey, A. El-Hashani, A. Benhmid, K. Ghwel, M. Benamer, *Chem. Sci. Int. J.* **24** (2018) 1 (https://doi.org/10.9734/csji/2018/44312)
30. P. Shah, N. Jha, A. Bhattarai, *J. Chem-Ny.* **2020** (2020) 5292385 (https://doi.org/10.1155/2020/5292385)
31. A. Rodríguez, M. del M. Graciani, M. L. Moyá, *Langmuir* **24** (2008) 12785 (https://doi.org/10.1021/la802320s)
32. S. Bračko, J. Špan, *Dyes Pigments* **50** (2001) 77 (https://doi.org/10.1016/S0143-7208(01)00025-0).

Journal of the Serbian Chemical Society
JSCS-info@shd.org.rs • www.shd.org.rs/JSCS
J. Serb. Chem. Soc. 86 (5) 495–505 (2021)
JSCS–5437
Original scientific paper

Electrochemical oxidation of 2,4,6-trichlorophenol on iron-doped nanozirconia ceramic

NADICA D. ABAZOVIĆ[1], TATJANA D. SAVIĆ[1], TATJANA B. NOVAKOVIĆ[2], MIRJANA I. ČOMOR[1#] and ZORICA D. MOJOVIĆ[2]*

[1]*Vinča Institute of Nuclear Sciences – National Institute of the Republic of Serbia, University of Belgrade, P.O. Box 522, 11000 Belgrade, Serbia and* [2]*University of Belgrade – Institute of Chemistry, Technology and Metallurgy – National Institute of the Republic of Serbia, Njegoševa 12, 11000 Belgrade, Serbia*

(Received 4 August, revised 13 November, accepted 30 November 2020)

Abstract: Solvothermaly synthesized zirconium oxide nanopowders, pure and doped with various amounts of iron ions (1–20 %), were used as modifiers of glassy carbon electrodes. The modified electrodes were tested in the reaction of electrochemical oxidation of 2,4,6-trichlorophenol (TCP) in order to investigate the influence of doping on electrochemical performance of zirconia matrix. The techniques of cyclic voltammetry and electrochemical impedance spectroscopy were employed. Cyclic voltammetry showed that electrooxidation of TCP proceeded through the oxidation of hydroxyl group. Possible pathway included the formation of quinones and the formation of polyphenol film on the electrode surface, leading to the electrode fouling. Iron doping enhanced the activity of zirconia matrix towards TCP electrooxidation. Electrochemical impedance spectroscopy showed the importance of iron content in zirconia matrix for the preferable pathway of TCP electrooxidation. The quinone formation pathway was favoured by low iron doped zirconia (doped with 1% of iron), while polyphenol film formation on the electrode surface was more pronounced at samples with higher iron ion content (for doping with 10 and 20 % of iron). The sample with 5 % of added iron ions, showed intermediate behaviour, where the formed polyphenol film showed slight degradation.

Keywords: ZrO_2; modified electrode; phenols.

INTRODUCTION

The extensive pollution is a worldwide problem today. Various pollutants, organic and inorganic, are being emitted and accumulated in different parts of the environment. Water pollution by phenol and its derivatives is recognized as a particular problem and addressed in a great number of articles. Europian Union,

* Corresponding author. E-mail: zoricam@nanosys.ihtm.bg.ac.rs
# Serbian Chemical Society member.
https://doi.org/10.2298/JSC200804078A

World Health Organization and American Environment Protection Agency have adopted the list of phenolic compounds that are considered as major pollutants. Among these pollutants chlorophenols are considered to be the most toxic and cancerous. Various methods have been investigated in order to detect[1–4] and remove[5–8] chlorophenols from water.

Electrochemical techniques attracted lot of attention because they are swift, efficient and low-cost. Additionally, the potential control enables easy and fine tuning of reaction. Various electrodes have been used to detect[9,10] and degrade[11–13] phenol compounds. Ureta-Zañartu *et. al.* investigated the mechanism of electrooxidation of phenol and phenol derivatives[14–20] on different electrodes. They concluded that there can be two possible pathways for the chlorophenol electrooxidation that proceeded to the formation of quinones or polymerization. The concentration of chlorophenol, the number of chlorine atoms and their position influences a preferable pathway, as well as a type of electrode.

Zirconia is eco-friendly ceramic material interesting as catalyst,[21] catalyst support[22] or photocatalyst,[23] being the only metal oxide material which, depending on crystal phase, can possess both Brønsted and Lewis acid and basic surface sites, and strong oxidizing and reducing ability[24]. However, since it is a wide band gap material ($E_g \approx 5.0$ eV) with the absorption edge placed deep in UV region of solar spectrum, its extensive application as photocatalyst is somewhat hindered. Various approaches have been developed to shift its spectral response towards the visible part of the spectrum, and among these, the doping of zirconia matrix with transition metal ions is a common strategy. In our previous study,[25] we have presented the synthesis and the detailed characterization of the series of iron doped zirconia samples (from 1 up to 20 wt.% of Fe^{3+}). Lower iron concentrations stabilized tetragonal crystal phase of zirconia, while for the highest dopant concentration (20 wt.%), beside tetragonal zirconia, hematite is also formed. The synthesized samples were probed in the photocatalytic degradation of 2,4,6-trichlorophenol (TCP) under simulated solar light. It was shown that photocatalytic activity greatly depends on the amount of added iron and on the formation of a great number of intraband defect sites (oxygen vacancies, Fe^{3+}/Fe^{2+} and Fe^{3+}/Fe^{4+} levels). Comparing two extremes: doped (1 wt.% Fe^{3+}) and composite (hematite/tetragonal zirconia) sample (20 wt.% Fe^{3+}), it turned out that the sample with lower iron content expressed higher efficiency toward TCP degradation. As far as we are aware, the electrochemical properties and the possible use of iron doped zirconia as the electrode material is studied previously only by Doménech-Carbó and Alarcón.[26,27]

In the present study, the effect of iron doping of zirconia on electrochemical oxidation of TCP was investigated. The iron-doped zirconia was used as modifier of glassy carbon electrodes. The electrochemical behaviour and electrocatalytic

properties were studied by cyclic voltammetry and electrochemical impedance spectroscopy.

EXPERIMENTAL

The solvothermal synthesis of pure and iron doped zirconium oxide nanopowders is presented elsewere.[25] Shortly, the appropriate amounts of iron (III) acetylacetonate and zirconium propoxide (70%) were mixed in acidic medium in a Teflon vessel and stirred vigorously in ice bath. After 15 min of stirring, the dispersion was autoclaved 24 h at 150 °C. The obtained powders were washed, dried weight and annealed at 600 °C for 3 h. The samples were denoted according to stoichiometric quantities of Fe ions, as ZrO_2, 1-ZrO_2, 5-ZrO_2, 10-ZrO_2 and 20-ZrO_2 (for 0, 1, 5, 10 and 20 wt.% of iron ions, respectively). The results of the detailed characterization are presented elsewhere.[25]

In order to use the investigated materials as electrode materials, 5 mg of each of the samples were homogeneously dispersed in 125 μl of the original 5 % Nafion solution, using an ultrasonic bath for 30 min. The droplets (10 μl) of these suspensions were placed on the surface of a glassy carbon electrode (GCE) (area = 0.0706 cm^2) and left to dry at 90 °C during 3h. After the solvent evaporation, the sample was uniformly distributed on the GCE in the form of a thin layer. For the electrochemical investigations in a three-electrode glass cell, the modified GCE, was used as working electrode. The reference electrode was Ag/AgCl in 3 M KCl, while a platinum foil served as a counter electrode. The electrochemical behaviour of samples was investigated in 0.1 M H_2SO_4 supporting electrolyte. TCP oxidation was investigated for the concentration of TCP of 1 mM in 0.1 M H_2SO_4. The electrochemical measurements were performed using Autolab electrochemical workstation (Autolab PGSTAT302N, Metrohm-Autolab BV, Netherlands). Cyclic voltammetry was performed at scan rate of 50 mV s^{-1}. Impedance measurements were carried out at constant potential using a 5 mV rms sinusoidal modulation in the 10 kHz–10 mHz frequency range.

RESULTS AND DISCUSSION

Electrochemical behavior of zirconia modified GCE in 0.1 M H_2SO_4

Cyclic voltammograms of ZrO_2 and iron-doped ZrO_2 modified GCE were recorded in 0.1 M H_2SO_4 at the scan rate of 50 mV s^{-1} (Fig. 1).

The potential range was chosen to encompass hydrogen and oxygen evolution at the potential range limits. Beside current the rise at the limits of the potential range due to hydrogen and oxygen evolution reaction, there is only one pair of redox peak at the potential of 0.55 V *vs.* Ag/AgCl. This pair of peaks can be ascribed to the Fe^{2+}/Fe^{3+} oxidation/reduction process. The intensity of the peak current rised with the increase of the Fe content in samples. The electrochemistry of iron oxides and iron doped zircon and zirconia was investigated by Doménech-Carbó *et al.*[26–28] The electrochemistry of solid materials on the electrode surface occurs at the three-phase boundary: solid sample, solid substrate electrode and electrolyte. Several processes can occur depending on the conductivity and solubility of the solid material: the oxidative dissolution of metals and alloys, the reductive dissolution of oxides and oxide hydrates and the reductive conversion of oxides and salts to metal deposits and dissolved anions. In the

media where protons are abundant, such as acid solution, the proton-promoted reductive dissolution of iron-species takes precedence:[26–28]

$$1/2Fe_2O_3 + 3H^+ + ne^- = (1–n)Fe^{3+} + nFe^{2+} + 3/2H_2O \quad (1)$$

$$FeO(OH) + 3H^+ + ne^- = (1–n)Fe^{3+} + nFe^{2+} + 2H_2O \quad (2)$$

The n value in above equations takes value 1 under condition that the medium is non-complexing, the proton-promoted dissolution is small and all dissolved iron is in Fe^{2+} form.

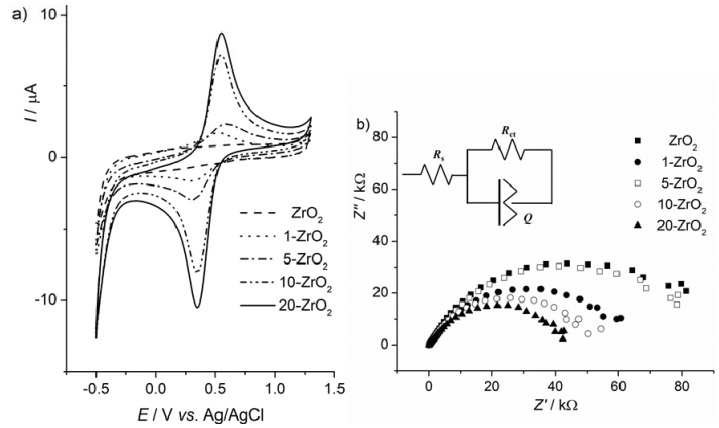

Fig 1. a) Cyclic voltammograms of ZrO_2 and iron-doped ZrO_2 in 0.1 M H_2SO_4, scan rate 50 mV s^{-1}; b) Nyquist plot for ZrO_2 and iron-doped ZrO_2 samples in 0.1 M H_2SO_4. Inset: equivalent electric circuit model used to fit experimental data.

According to the results of characterization[25] Fe ions were incorporated into the ZrO_2 matrix, in both crystalline phases and on the surface and in the bulk of nanoparticles. Also, in the sample with highest Fe^{3+} concentration, hematite can be detected. Slight decrease of current was noticed with the increase of cycling number that probably indicates the dissolution of iron species.

Further characterization of the samples was performed by the electrochemical impedance spectroscopy. For a modified electrode, the Nyquist plot recorded at 0.5 V showed a characteristic semi-circle pattern. The obtained EIS data (Fig. 1b) were used to fit an equivalent electrical circuit model (Fig. 1b, inset). In this circuit model R_s represents the solution resistance, while R_{ct} and constant phase element (CPE) are the charge transfer resistance and the non-ideal capacitor, respectively. The values of R_s and R_{ct} were obtained as the intercept of the recorded curve with x-axis at high frequencies and low frequencies, respectively. CPE usually represents the double layer capacitance and can be described by following equation:

$$Z = 1/(Y_0(j\omega)^{\alpha}) \quad (3)$$

where Y_0 is CPE admittance, j is the imaginary unit, ω is the angular frequency and α is CPE exponent which is associated with the system inhomogeneity. The capacitance element CPE would be pure capacitance when $\alpha = 1$ while it would be pure resistance when $\alpha = 0$. For the values $0.5 < \alpha < 1$ CPE is the non-ideal capacitor, which is influenced by surface heterogeneity. The values of circuit elements obtained by fitting were presented in Table I.

TABLE I. The electrochemical parameters extracted from the EIS data recorded in 0.1 M H_2SO_4 (R_s – the solution resistance; R_{ct} – the charge transfer resistance; Y_0 – CPE admittance, n – CPE exponent)

Sample	R_s / Ω	R_{ct} / kΩ	Y_0 / μS s^n	α
ZrO_2	60.9	105.3	6.26	0.73
1-ZrO_2	52.8	79.6	7.81	0.66
5-ZrO_2	54.6	104.1	5.99	0.69
10-ZrO_2	58.0	54.4	5.55	0.76
20-ZrO_2	51.5	45.9	5.68	0.74

The solution resistance, R_s, is almost constant (51–61 Ω) for all investigated samples. The charge transfer resistance, R_{ct}, had the highest value for ZrO_2, and this value decreased with the increase of Fe content in the samples. The only exception was sample 5-ZrO_2 that had charge transfer resistance almost equal to the starting material. The possible explanation might be the partial formation of zirconium ferrite, leaving much fewer Fe^{3+} for doping of zirconia matrix.[25] The admittance is proportional to the surface area involved in the electrochemical reaction.[29] There was no great variation in the values of admittance, although the highest admittance value was obtained for 1-ZrO_2 sample.

Electrochemical behavior of zirconia modified GCE in 0.1 M H_2SO_4 in the presence of TCP

Fresh GCE modified with zirconia was placed in the 0.1 M H_2SO_4 solution containing 1 mM TCP. The cycling of all electrodes measured in the potential range of –0.5 to 1.3 V, produced the family of voltammogram curves. The representative family of curves obtained for 5-ZrO_2 modified GCE is presented in Fig. 2a.

The irreversible anodic peak at 0.93 V, designated as a, corresponded to the oxidation of hydroxyl group at TCP. The peak current slightly decreased with cycling, which is considered as electrode fouling, due to the formation of polyphenol film.[30] The reversible pair of peaks (a2/c2) at lower potential was ascribed to the formation of quinones, and the anodic peak currents increased with cycling. The cyclic voltammograms of all investigated samples in 0.1 M H_2SO_4 containing 1 mM TCP had similar shape (Fig. 2b). The comparison of investigated modified electrodes was performed by the voltametric parameters obtained from cyclic voltammograms presented in Fig. 2b (Table II).

The onset potential is the potential at the foot of peak wave when the current starts to increase, *i.e.*, the potential that is necessary to reach for faradic current to

rise above capacitive current. As the indicator of electrode activity, the onset potential is particularly useful when the process that is investigated leads to the electrode fouling. The decreased values of onset potential were obtained for 1-ZrO_2 and 5-ZrO_2 samples, indicating higher electrode activity in comparison to undoped ZrO_2, 10- and 20-ZrO_2.

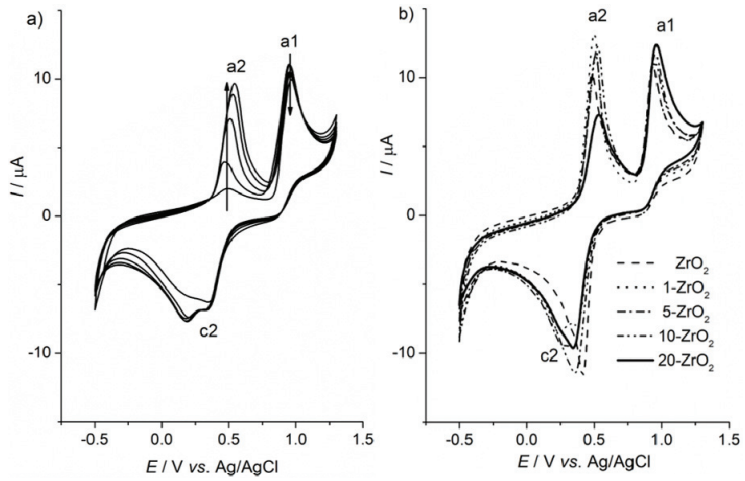

Fig 2. a) Successive cyclic voltammograms recorded on 5-ZrO_2. The arrows indicate the direction of peak current change with cycling; b) 5th cyclic voltammograms recorded on ZrO_2 and iron-doped ZrO_2 in 1 mM TCP + 0.1 M H_2SO_4, scan rate 50 mV s^{-1}.

TABLE II. The parameters obtained from cyclic voltammograms presented in Figure 2b: E_{a1} – peak potential of peak a1, E_o – onset potential for peak a1, Q – peak charge of designated peak

Sample	E_{a1} / V	E_o / V	Q_{a1} / µC	Q_{a2} / µC	Q_{c2} / µC	Q_{a2}/Q_{c2}	Q_{a2}/Q_{a1}
ZrO_2	0.93	0.82	0.73	0.98	1.01	0.97	1.34
1-ZrO_2	0.93	0.80	0.81	1.25	1.20	1.04	1.54
5-ZrO_2	0.94	0.81	0.90	1.19	1.21	0.98	1.32
10-ZrO_2	0.95	0.83	1.01	1.23	1.38	0.89	1.22
20-ZrO_2	0.96	0.82	1.08	0.71	1.11	0.64	0.66

The peak charge of peak a1 rises with the increase of the iron ion content in the zirconia sample on the GCE, indicating that the iron (iron oxide) enhanced the electrocatalytic activity of ZrO_2 for the oxidation of hydroxyl group of TCP. The highest current of TCP electrooxidation was obtained for 20-ZrO_2 electrode.

The oxidation of phenol and phenol derivatives usually produce one or two pair of reversible peaks due to formation of orto- or/and para-hydroquinone. In order to form quinones from TCP it is necessary to eliminate at least one of the chlorine atoms. The chlorine atom in para- position is the probable candidate due to less steric hindrance.[31] For samples with 1-ZrO_2 and 5-ZrO_2 the separation of

cathodic peak c2 was observed (Fig. 2a and b), which probably originated from the slight potential difference of iron reduction and hydroquinone formation. With the increase of the iron ions content, the potential difference between these two processes could not be observed any more. This finding implies the difference in iron ions properties/surroundings in the resulting samples formed at various iron ions content. These findings are in the accordance with our previous work,[25] where it was shown that samples with 10 and 20 % of iron ions have formed hematite phase, detected using XRD technique. 10-ZrO_2 and 20-ZrO_2 are actually composites of hematite and Fe-doped zirconia, i.e. iron ions exist as iron oxide and as dopant in zirconia matrix, while in the zirconia samples with lower iron ions content (1 and 5 %) iron ions exist only as dopants.

The ratio of the anodic to the cathodic charge of the hydroquinone/quinone process, (Q_{a2}/Q_{c2}), yields the reversibility of the hydro- quinone/quinone couple (Table II). The reversibility was almost equal for the undoped and the zirconia doped up to 5 % of Fe ions. The further increase of the iron ions content led to the decrease of the reversibility. The ratio Q_{a2}/Q_{a1} could be used to estimate the fraction of TCP oxidized to quinone[15]. These values were above unity except for 20-ZrO_2, and the highest value was obtained for 1-ZrO_2. This finding might indicate that the electrooxidation of TCP on samples with the high content of iron in zirconia matrix favours polyphenol film formation pathway. Bearing in mind that the oxido-reduction of iron ions zirconia matrix on the GCE occurs at similar potential as the formation of quinone, these features has to be taken with caution. Additionally, the cathodic peak currents did not show increase with the number of cycles, indicating a possible overlap of mentioned processes.

Further investigation of the electrochemical behaviour of TCP on zirconia samples was performed by the electrochemical impedance spectroscopy recorded at several potentials around the potential of oxidation of the hydroxide group of TCP: 0.80 (before peak potential), 0.93 (peak potential) and 1.10 V (after peak potential). The obtained Nyquist plots are presented in Fig. 3a–c.

The Nyquist plot recorded at peak potential consist of semicircle and straight line indicating the diffusion controlled Faradic process. The plot recorded at the potential 0.80 V shows characteristic semicircle obtained, indicating a charge transfer process, while the shape of plot recorded at 1.10 V showed the high resistance toward charge transfer process. The impedance data obtained at different potentials have been adjusted to the equivalent circuits presented in the inserted picture each Fig. 3a–c and the results are presented in Table III.

The equivalent circuit used for the plot recorded at peak potential contained two CPE corresponding to diffusion process (Q_1) and double layer capacitance (Q_2).

The charge transfer resistance at peak potential decreased with the increase of iron ions content present in samples, while the reverse trend was noticed for

potential of 1.10 V, probably due to fouling of the electrode surface by the polyphenol film.[15] Plot of the logarithm of the impedance, as a function of the potential at constant frequencies for ZrO_2, is presented in Fig. 3d. The plots obtained for other samples were similar and are not presented for the sake of clarity. The comparison of samples is presented in Fig. 3e as the plot of the logarithm of the impedance as a function of the potential at high frequency (10^4 Hz), *i.e.*, the resistance designated as R_s. The increase of impedance with potential indicates fouling of the electrode.[16] The impedance obtained for 1-ZrO_2 is higher than the impedance obtained for undoped ZrO_2, but the value remained constant with the increase of potential evidencing the absence of fouling. A slight decrease of impedance at potential of 1.10 V obtained for 5-ZrO_2 indicated some degradation of the formed polymer film. The samples with high content of iron (10 and 20 %) showed that fouling of the electrode is most likely to occur on these electrodes.

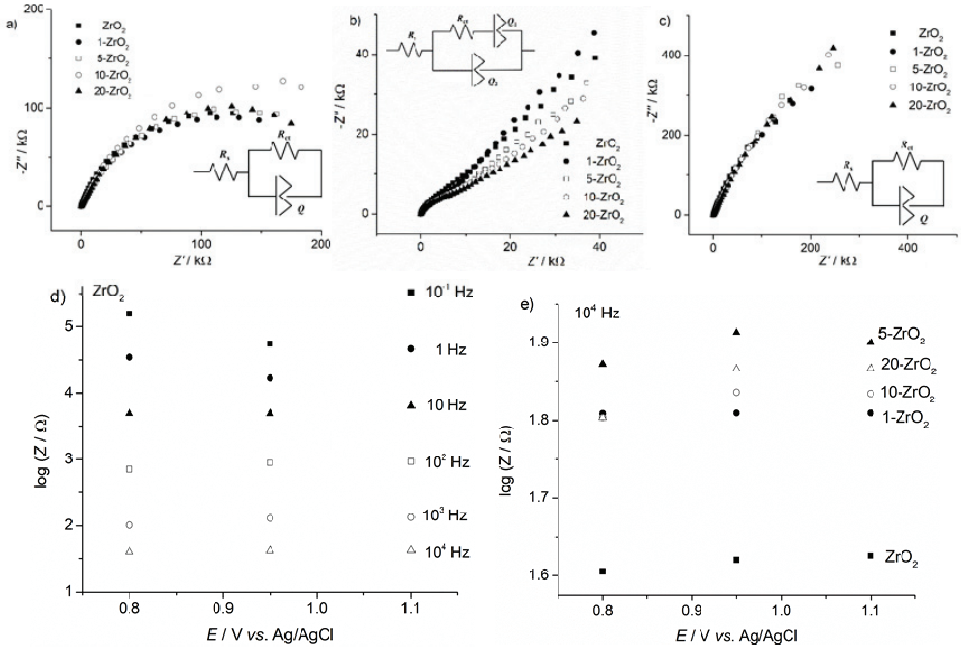

Fig 3. Nyquist plot for ZrO_2 and iron-doped ZrO_2 samples in 1 mM TCP + 0.1 M H_2SO_4 recorded at a) 0.80, b) 0.93 and c) 1.10 V (inset: equivalent electric circuit model used to fit experimental data.); d) plots of log|*Z*| *vs.* applied potential at the designated constant frequencies of a ZrO_2 electrode in 1 mM TCP + 0.1 M H_2SO_4; e) plots of log|*Z*| *vs.* applied potential at the frequency of 10^4 Hz for ZrO_2 and iron-doped ZrO_2 samples.

The results obtained from electrochemical studying of these samples indicated that iron enhances the electrocatalytic properties of ZrO_2 towards the oxidation of TCP. However, doping of 1 % pushed the reaction toward the formation

of quinons, while the higher iron content directed the reaction also towards the formation of polymer film and the passivation of electrode.

TABLE III. The electrochemical parameters extracted from the EIS data in 1 mM TCP + 0.1 M H_2SO_4 (R_s – the solution resistance; R_{ct} – the charge transfer resistance; Y – CPE admittance, n – CPE exponent)

Sample	At potential of 0.80 V			At potential of 0.93 V					At potential of 1.10 V		
	R_{ct} / kΩ	Y / μS s^n	n	R_{ct} / kΩ	Y_1 / μS s^n	n	Y_2 / μS s^n	n	R_{ct} / MΩ	Y / μS s^n	n
ZrO_2	229	5.6	0.9	11.0	23.9	0.6	4.4	0.9	1.0	4.4	0.8
1-ZrO_2	267	4.9	0.8	9.9	20.7	0.6	4.1	0.8	1.8	3.8	0.8
5-ZrO_2	314	4.3	0.8	7.6	27.6	0.5	3.1	0.8	2.1	3.2	0.8
10-ZrO_2	369	4.0	0.8	7.0	28.7	0.5	2.5	0.8	2.5	3.1	0.8
20-ZrO_2	295	3.7	0.8	5.2	31.4	0.4	2.1	0.8	3.1	3.0	0.8

CONCLUSION

Solvothermaly synthesized pure and Fe-doped zirconia nanopowders were applied on the surface of glassy carbon electrode by Nafion and tested in the reaction of electrooxidation of 2,4,6-trichlorophenol (TCP). Cyclic voltam-mograms of all investigated electrodes showed the characteristic peak of oxidation of hydroxyl group at TCP and the reversible pair of peaks ascribed to the formation of quinones. Investigation of the electrodes based on pure and doped zirconium oxide nanopowders revealed that the amount of iron present in the sample influenced the pathway of TCP oxidation. The increase of iron content led to the increase of the current of TCP electrooxidation. However, the different iron content led to the various pathways of TCP electrooxidation. The low iron doping (1-ZrO_2) favoured the formation of quinons, while the samples with iron ion content higher than 1 % favoured the formation of polyphenol film on the electrode surface and the passivation of electrode. The 5-ZrO_2 electrode showed mixed behaviour reflected in the slight degradation of polyphenol film formed on this electrode.

Acknowledgement. This work was supported by the Ministry for Education, Science and Technological Development of the Republic of Serbia (Grants No. 451-03-68/2020-14/ /200026 and 451-03-68/2020-14/200017).

И З В О Д

ЕЛЕКТРОХЕМИЈСКА ОКСИДАЦИЈА 2,4,6-ТРИХЛОРФЕНОЛА НА НАНО-ЦИРКОНИЈУМ-ОКСИДНОЈ МАРТИЦИ ДОПИРАНОЈ ГВОЖЂЕМ

НАДИЦА Д. АБАЗОВИЋ[1], ТАТЈАНА Д. САВИЋ[1], ТАТЈАНА Б. НОВАКОВИЋ[2], МИРЈАНА И. ЧОМОР[1] и ЗОРИЦА Д. МОЈОВИЋ[2]

[1]Институт за нуклеарне науке Винча – Институт од националног значаја за Републику Србију – Универзитет у Београду, Београд и [2]Универзитет у Београду – Институт за хемију, технологију и металургију – Институт од националног значаја за Републику Србију, Његошева 12, 11000 Београд

Нанопрахови цирконијум-оксида, чисти и допирани различитим количинама јона гвожђа синтетисани су солвотермалном методом. Добијени прахови су коришћени као

модификатори електрода од стакластог угљеника. Модификоване електроде су тестиране у реакцији електрохемијске оксидације 2,4,6-трихлорфенола (TCP), како би се испитао утицај допанта на перформансе цирконијум-оксидне матрице. За испитивање су коришћене технике цикличне волтаметрије и електрохемијске импедансне спектроскопије. Резултати цикличне волтаметрије су показали да се електрооксидација TCP одиграва преко оксидације хидроксилне групе. Могуће даље реакционе путање су укључивале формирање хинона и настајање полифенолног филма на површини електроде који доводи до пасивације електроде. Допирање јонима гвожђа је повећало активност цирконијум-оксидне матрице за електрооксидацију TCP. Резултати електрохемијске импедансне спектроскопије су указали на утицај количине јона гвожђа у цирконијум-оксидној матрици на реакциони механизам TCP електроосидације. Реакциона путања која укључује формирање хинона је фаворизована на цирконијум-оксидним електродама са ниским садржајем јона гвожђа (допираног са 1 % јона гвожђа), док је формирање полифенолног филма дошло до изражаја на узорцима са већим садржајем јона гвожђа (допираних са 10 и 20 % јона гвожђа). Узорак цирконијум-оксида, допиран са 5 % јона гвожђа, има прелазна својства, јер долази до формирања полифенолног филма на површини електроде, али и до његове разградње.

(Примљено 4. августа, ревидирано 13. новембра, прихваћено 30. новембра 2020)

REFERENCES

1. C. Terashima, T. N. Rao, D. A. Tryk, A. Fujishima, *Anal. Chem.* **74** (2002) 895 (https://doi.org/10.1021/ac010681w)
2. M. Saraji, M. Ghani, *J. Chromatogr., A* **1418** (2015) 45 (https://doi.org/10.1016/j.chroma.2015.09.062)
3. S. Almeda, L. Nozal, L. Arce, M. Valcárcel, *Anal. Chim. Acta* **587** (2007) 97 (https://doi.org/10.1016/j.aca.2007.01.035)
4. Y. Higashi, Y. Fujii, *J. Liq. Chromatogr. Relat. Technol.* **32** (2009) 2372 (https://doi.org/10.1080/10826070903188013)
5. A. J. Barik, P. R. Gogate, *Ultrason. Sonochem.* **40** (2018) 383 (https://doi.org/10.1016/j.ultsonch.2017.07.029)
6. C. Tai, G. Jiang, *Chemosphere* **59** (2005) 321 (https://doi.org/10.1016/j.chemosphere.2004.10.024)
7. J. Xiong, C. Hang, J. Gao, Y. Guo, C. Gu, *Chem. Eng. J.* **254** (2014) 276 (https://doi.org/10.1016/j.cej.2014.05.139)
8. L. Wang, D. Kong, Y. Ji, J. Lu, X. Yin, Q. Zhou, *Chem. Eng. J.* **343** (2018) 235 (https://doi.org/10.1016/j.cej.2018.03.006)
9. M. Shabani-Nooshabadi M, Roostaee, F. Tahernejad-Javazmi, *J. Mol. Liq.* **219** (2016) 142 (https://doi.org/10.1016/j.molliq.2016.01.081)
10. S. Hashemnia, Sh. Khayatzadeh, M. Hashemnia, *J. Solid State Electrochem.* **16** (2012) 473 (https://doi.org/10.1007/s10008-011-1355-2)
11. C. Comninellis, A. Nerini, *J. Appl. Electrochem.* **25** (1995) 23 (https://doi.org/10.1007/BF00251260)
12. Z. Sun, X. Ma, X. Hu, *Environ. Sci. Pollut. Res*. **24** (2017) 14355 (https://doi.org/10.1007/s11356-017-9004-7)
13. Y. Yao, L. Jiao, N. Yu, J. Zhu, X. Chen, *Russ. J. Electrochem.* **52** (2016) 348 (https://doi.org/10.1134/S1023193516040157)
14. M. S. Ureta-Zañartu, P. Bustos, M. C. Diez, M. L. Mora, C. Gutiérrez, *Electrochim. Acta* **46** (2001) 2545 (https://doi.org/10.1016/S0013-4686(01)00448-0)

15. F. Fernández, C. Berríos, E. Garrido-Ramírez, N. Escalona, C. Gutiérrez, M. S. Ureta-Zañartu, *J. Appl. Electrochem.* **44** (2014) 1295 (https://doi.org/10.1007/s10800-014-0763-2)
16. C. Berríos, J. F. Marco, C. Gutiérrez, M. S. Ureta-Zañartu, *Electrochim. Acta* **54** (2009) 6417 (https://doi.org/10.1016/j.electacta.2009.06.017)
17. C. Berríos, R. Arce, M. C. Rezende, M. S. Ureta-Zañartu, C. Gutiérrez, *Electrochim. Acta* **53** (2008) 2768 (https://doi.org/10.1016/j.electacta.2007.10.053)
18. M. S. Ureta-Zañartu, M. L. Mora, M. C. Diez, C. Berríos, J. Ojeda, C. Gutiérrez, *J. Appl. Electrochem.* **32** (2002) 1211 (https://doi.org/10.1023/A:1021680420834)
19. M. S. Ureta-Zañartu, C. Berríos, J. Pavez, J. Zagal, C. Gutiérrez, J. F. Marco, *J. Electroanal. Chem.* **553** (2003)147 (https://doi.org/10.1016/S0022-0728(03)00309-7)
20. M. S. Ureta-Zañartu, P. Bustos, C. Berríos, M. C. Diez, M. L. Mora, C. Gutiérrez, *Electrochim. Acta* **47** (2002) 2399 (https://doi.org/10.1016/S0013-4686(02)00043-9)
21. W. Xia, F. Wang, X. Mu, K. Chen, *React. Kin. Mech. Catal.* **122** (2017) 463 (https://doi.org/10.1007/s11144-017-1193-z)
22. Y. Wang, X. Yang, Y. Chen, S. Nie, M. Xie, *React. Kin. Mech. Catal.* **122** (2017) 915 (https://doi.org/10.1007/s11144-017-1243-6)
23. M. V. Carević, N. D. Abazović, T. D. Savić, T. B. Novaković, D. J. Pjević, M. I. Čomor, *J. Am. Ceram. Soc.* **101** (2018) 1420 (https://doi.org/10.1111/jace.15324)
24. K. C. Soni, S. C. Shekar, B. Singh, T. Gopi, *J. Colloid Interface Sci.* **446** (2015) 226 (https://doi.org/10.1016/j.jcis.2015.01.031)
25. M. V. Carević, T. D. Savić, N. D. Abazović, M. D. Mojović, T. B. Novaković, M. I. Čomor, *Ceram. Int.* **46** (2020) 6820 (https://doi.org/10.1016/j.ceramint.2019.11.175)
26. A. Doménech-Carbó, G. Herrera, N. Montoya, P. Pardo, J. Alarcón, M. T. Doménech-Carbó, M. Silva, *J. Electrochem. Soc.* **161** (2014) H539 (https://doi.org/10.1149/2.0751409jes)
27. G. Herrera, N. Montoya, A. Domenech, J. Alarcón, *Phys. Chem. Chem. Phys.* **15** (2013) 19312 (https://doi.org/10.1039/C3CP53216J)
28. A. Doménech-Carbó, M. T. Doménech-Carbó, J. V. Gimeno-Adelantado, F. Bosch-Reig, M. C. Saurí-Peris, S. Sánchez-Ramosa, *Analyst* **126** (2001) 1764 (https://doi.org/10.1039/B100257K)
29. K. W. Cho, V. S. Rao, H.S. Kwon, *Electrochim. Acta* **52** (2007) 4449 (https://doi.org/10.1016/j.electacta.2006.12.032)
30. H. Al-Maznai, B. E. Conway, , *J. Serb. Chem. Soc.* **66** (2001) 765 (https://doi.org/10.2298/JSC0112765A)
31. Z. Ežerskis, Z. Jusys, *J. Appl. Electrochem.* **31** (2001) 1117 (https://doi.org/10.1023/A:1012280216273).

Journal of the Serbian Chemical Society
JSCS-info@shd.org.rs • www.shd.org.rs/JSCS
J. Serb. Chem. Soc. 86 (5) 507–519 (2021)
JSCS–5438
Original scientific paper

Trace determination of isoniazid at micro level using kinetic spectrophotometric method

RUPAL YADAV, INDRESH KUMAR and RADHEY MOHAN NAIK*

Department of Chemistry, University of Lucknow, Lucknow, (U.P.) – 226007, India

(Received 13 May 2020, revised 27 February, accepted 4 March 2021)

Abstract: An effective and fairly inexpensive spectrophotometric method for tracing the determination of isoniazid (INH) in pure form, as well as in pharmaceutical formulations, has been developed through the ligand substitution reaction between INH and aquapentacyanoruthenate (II) ion ($[Ru(CN)_5OH_2]^{3-}$) in aqueous medium at λ_{max} = 502 nm. The fixed time procedure has been employed under optimum reaction conditions. The calibration equations, relating absorbance measured at 502 nm at fixed times (t_n = 2, 5 and 7 min) and c_{INH} in linear range 1.37-27.43 μg mL^{-1}, were used for the trace determination of INH, which has been reported in the present investigation and are in agreement with official and reported methods. The percentage recovery has been calculated and found to be within the range of 99–101 % in the analysis of different pharmaceutical samples. The results reveal that the use of common recipients as the used additives do not produce any type of interference in the suggested method. The validity of the proposed method was also checked by statistical analysis which agreed with the results obtained using the official method. The present method is very simple, reproducible, sensitive and it can be adopted for trace determination of INH in different samples without using extracting agent.

Keywords: ligand substitution reaction; aquapentacyanoruthenate (II) ion; calibration equations; pharmaceutical samples analysis

INTRODUCTION

Tuberculosis, caused by *Mycobacterium tuberculosis*, is a major health hazard for the society and currently a prominent cause of mortality among all existing diseases globally as it affected a mass population worldwide[1]. Patients with the decreased immunity are suspected to be frequent sufferer. At present, the front-line treatment against the infection caused by *Mycobacterium tuberculosis* involves the use of first line drug isoniazid[2] (Fig. 1), prepared first in 1912[3] and was found to be effective against tuberculosis in 1952.[4] Although INH possess a very simple chemical structure and exhibits various pharmaceutical properties

* Corresponding author. E-mail: adheynaik@gmail.com
https://doi.org/10.2298/JSC200513017Y

over last few decades, yet it is possible that the synergistic mechanism of action still remains uncertain.[5]

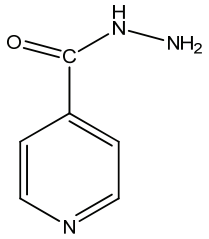

Fig. 1. Structure of isoniazid, INH.

Isoniazid, INH (pyridine-4-carboxylic acid hydrazide), commercially known as isonicotinylhydrazide, is a prodrug and it is activated by the enzyme catalase-peroxidase, produces isonicotinoyl acyl radical[6] through subsequent steps after being added to NAD^+ and forms adduct, INH-NADH. The adduct so formed that it is responsible for producing antitubercular activity in INH[7]. Owing to various biological and medicinal applications of INH in several industrial and pharmaceutical processes, its determination in pure form and in pharmaceutical preparations (dosage form) is of great public interest. The various analytical methods for detection, determination and analysis of INH in pharmaceutical formulations as well as in analytical and biological samples have been described in literature based on colorimetry,[8] spectrophotometry,[9] NMR spectroscopy,[10] spectrofluorimetry,[11] atomic absorption spectrometry,[12] chemiluminescence-based detection,[13] capillary electrophoresis,[14] flow injection analysis,[15] kinetic determination,[16,17] voltammetry/electrochemical[18,19] and different chromategraphic techniques such as capillary gas chromatography,[20] thin layer chromatography,[21,22] electrokinetic chromatography,[23,24] liquid chromatography[25] and high-performance liquid chromatography.[26] Recently, analytical methods for the isoniazid determination has been reviewed. In addition to the above mentioned techniques, some indirect approaches have also been reported for the determination of INH such as the designation of an optical sensor by Safavi and Bagheri.[27] Recently, analytical methods for the isoniazid determination have been reviewed.[28] Many of the methods reported above require expensive and hazardous chemicals and involves sophisticated instrumental techniques. These techniques are very expensive**,** time consuming and not easily accessible in most of the laboratories in India, which limits their direct applications in real samples. In the past, few analytical methods were developed by Naik *et al.* for different analytes[29–35] and Prasad *et al.*[36] Based on the knowledge gained by us in our earlier investigations, here we report a reliable kinetic spectrophotometric method, which has good reproducibility for the trace determination of INH at micro level in pure form as well as in pharmaceutical samples. The present investigation is based on the ligand exchange reaction between aquapentacyanoruthenate(II) ion ($[Ru(CN)_5OH_2]^{3-}$)

and INH in aqueous medium and it is the first indicator reaction of its kind, using aqupentacyanoruthenate(II) for the determination of INH in various pharmaceutical preparations. Further, the novelty of the proposed method lies in the fact that the statistical parameters, as well as recovery experiment data, demonstrates high reproducibility and accuracy of the method and compares adequately with the official reported method[37] for the assay of the INH tablets. Apart from this, the analysis of the pharmaceutical preparations which contain isoniazid as a single drug, as well as the multiple ingredients which show the no interference from the common excipients and does not involve the use of any oxidant, prior heating of a sample containing an extracting agent and uses a simple spectrophotometer for determination.

Therefore, this method could be recommended for the determination of isoniazid in pharmaceutical quality control laboratories.

The applicability of the method was tested on 6 INH containing pharmaceutical samples with the use of pre-established calibration equations, between the absorbance and the time at the fixed wavelength based on the fixed time procedure.

EXPERIMENTAL

Reagents

All analytical reagent grade chemicals and double distilled de-ionised water were used throughout the present kinetic study. All the solutions were stored in dark amber coloured bottles to prevent photodecomposition and oxidation. Potassium hexacyanoruthenate(II) ($K_4[Ru(CN)_6]\cdot 2H_2O$) was obtained from Merck (India) and used as received. The INH was purchased from BDH (UK) and its required stock solution was made in the double distilled de-ionized water by weighing the calculated amount accurately. The sodium perchlorate was purchased from Merck and used without any further purification. Now, a 2×10^{-2} mol dm^{-3} of $NaClO_4$ was prepared and used to maintain the ionic strength (μ) of the reaction mixture at a desired value. A 10^{-2} M stock solution of bromine was standardized regularly using the iodometric method.[38] The pH of the reaction mixture was maintained using KCl/HCl or potassium hydrogen phthalate and HCl/NaOH buffer.[39] Standard BDH buffers were used to standardize the pH meter regularly from time to time.

Apparatus

The ligand substitution kinetics between $[Ru(CN)_5OH_2]^{3-}$ and INH was studied spectrophotometrically using a single beam visible-spectrophotometer model DIGI-110 (SISCO, India), equipped with a circulatory arrangement of water for thermostating the cell compartment. Recording of the absorption spectra was made by the UV–Vis double-beam spectrophotometer (Systronic-2203). All the pH measurements were made by Systronics μ pH system, 361 model. All the volumetric apparatus used were of certified 'A' grade and steamed regularly before each kinetic run. Acetone and 10 % HNO_3 solutions were used for cleaning of the quartz cuvettes from time to time.

Experimental procedure

All the reaction conditions have been optimized to carry out the experiment optimized in an order to attain the maximum reaction rate and sensitivity. The stock solutions were accur-

ately diluted to the required concentrations. In order to attain the thermal equilibrium, all the working solutions were placed in a self-designed thermostat for at least 30 min at 25.00±0.01 °C, prior to the start of the reaction, by placing them in volumetric flasks. All the thermally pre-equilibrated reagent solutions were added in a reaction mixture in the sequence: $[Ru(CN)_5OH_2]^{3-}$, $NaClO_4$ and INH to initiate the reaction. The reaction mixture was properly shaken and quickly transformed into a 10 mm spectrophotometric quartz cuvette, placed in a pre-thermostatic cell compartment of spectrophotometer. The progress of the reaction was monitored by monitoring the increase in the absorbance due to the formation of pale yellow coloured complex, $[Ru(CN)_5INH]^{3-}$ (λ_{max} = 502 nm) where only product absorbs strongly, while other reactants do not have appreciable absorbances at this wavelength.

The examined reaction is believed to proceed through Eqs. (1) and (2), respectively:

$$\left[Ru(CN)_6\right]^{4-} + Br_2 \xrightarrow{H_2O} \left[Ru(CN)_5OH_2\right]^{3-} + Br^- + BrCN \quad (1)$$

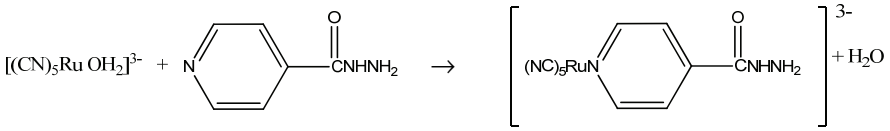

(2)

Eq. (1) represents the generation of $[Ru(CN)_5OH_2]^{3-}$ (pale yellow colour, having λ_{max} = 310 nm) through rapid aquation of $[Ru(CN)_6]^{4-}$, mixing the equimolar concentrations of hexacyanoruthenate(II) and bromine with KBr in tenfold excess other reactants do not have appreciable absorbances at this wavelength.

RESULTS AND DISCUSSION

The incess[37] generates the desired pale yellow product, *i.e.*, $[Ru(CN)_5INH]^{3-}$, in Eq. (2) upon subsequent reaction with INH. The pale yellow colour solution gets intensified and a peak grows at 502 nm due to the formation of the product, *i.e.*, $[Ru(CN)_5INH]^{3-}$. The absorbance spectra for the reactants and the product are given in Fig. 2.

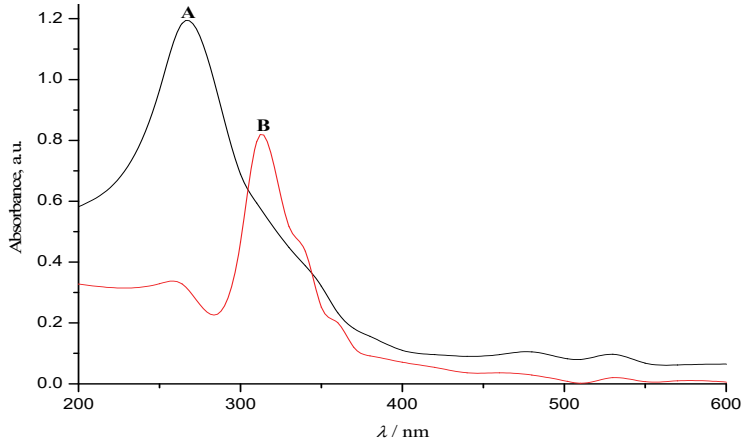

Fig. 2. UV–Vis absorption spectra of the reactants: A – $c_{INH} = 5\times10^{-3}$ mol dm^{-3}; B – $c_{[Ru(CN)5OH2]3-} = 5\times10^{-4}$ mol dm^{-3}.

The repetitive spectral scan for the formation of the product, $[Ru(CN)_5INH]^{3-}$, is given in Fig. 3. and it clearly demonstrates the formation of product which has the wavelength of maximum absorbance (λ_{max} at 502 nm).

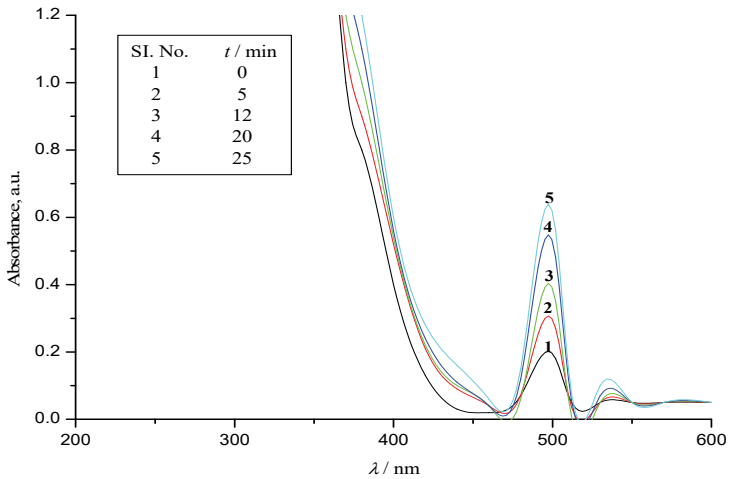

Fig. 3. Repetitive spectral scan of formation of product, $[Ru(CN)_5INH]^{3-}$ under the reaction conditions: $c_{[Ru(CN)_5OH_2]^{3-}} = 5\times10^{-4}$ mol dm^{-3}, $c_{INH} = 5\times10^{-3}$mol dm^{-3}, pH 4.00±0.02, $\mu = 2\times10^{-2}$ mol dm^{-3} ($NaClO_4$) and $t = 25.00\pm0.01$ °C.

In general, the reaction rate is found to be influenced by various parameters, *viz.* pH, concentration of reactant, ionic strength and temperature. Thus, the kinetics of the examined reaction is studied by optimizing the different parameters sequentially, under pseudo-first-order condition by keeping all the parameters fixed at a constant value, except the one whose effect has to be studied. In the present work, the effects of pH, $c_{[Ru(CN)_5OH_2]^{3-}}$, c_{INH}, ionic strength and temperature variation on the reaction rate have been investigated thoroughly. Optimized experimental conditions were made by a precise investigation of the kinetic study of the indicator reaction. The $c_{[Ru(CN)_5OH_2]^{3-}}$ and c_{INH} were varied from 2.0×10^{-4}–7.0×10^{-4} mol dm^{-3} and 10^{-5}–2×10^{-4} mol dm^{-3}, respectively. The reaction was studied at a pH 4.00±0.02. All the results were obtained at $t = 25.00\pm0.01$ °C and $\mu = 2\times10^{-2}$ mol dm^{-3}, respectively.

Effect of pH

The reaction rate depends upon the pH of the reaction mixture and therefore the maintenance of pH is essential to be at an optimum level. In order to select a suitable value of pH, its influence on the reaction rate was investigated in a pH range 2.0–8.0 using the fixed time procedure method, as a measure of the initial rate. The pH of the reaction mixture was varied using potassium hydrogen phthalate/NaOH or potassium hydrogen phthalate/HCl buffer.[40] The variations obs-

erved in initial rate (A_t) after 2 and 8 min of the mixing of the reagents as a function of the pH is provided in Fig. 4. It was observed that the reaction rate was slow at low pH values initially, became the maximum at pH of 4.00±0.02 and then it decreased. At low pH, lower reaction rate is attributed to the formation of various protonated species[41] of $[Ru(CN)_6]^{4-}$ such as monoprotonated; $H[Ru(CN)_6]^{3-}$ and diprotonated, $H_2[Ru(CN)_6]^{2-}$. Again, at higher pH, the low reaction rate is due to lack of protons. Thus, the pH 4.00±0.02 is associated with the maximum absorption and selected as an optimum pH for further study.

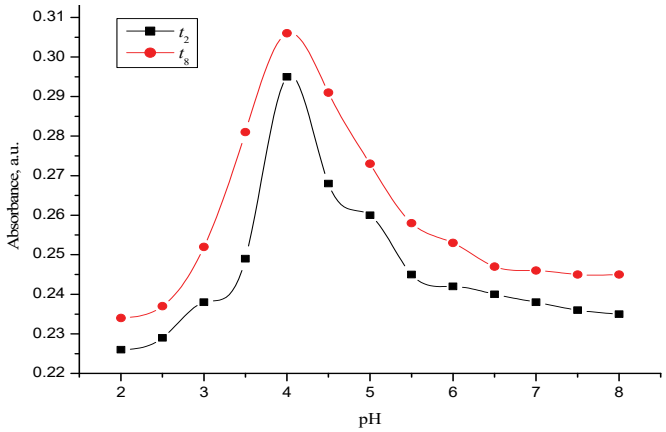

Fig. 4. Effect of pH on the reaction rate under the reaction conditions: $c_{[Ru(CN)_5OH_2]^{3-}} = 6\times10^{-4}$ mol dm^{-3}, $c_{INH} = 5\times10^{-3}$mol dm^{-3}, pH 4.00±0.02, $\mu = 2\times10^{-2}$ mol dm^{-3}($NaClO_4$) and t = 25.00±0.01 °C.

Effect of $[Ru(CN)_5OH_2]^{3-}$

The above selected value of pH 4.00±0.02 facilitated us to do further investigation by varying other parameters sequentially. The influence of $c_{[Ru(CN)_5OH_2]^{3-}}$ upon absorption intensity during the formation of $[Ru(CN)_5INH]^{3-}$ was investigated by the variation of its concentration in the range of 2.0×10^{-4}–7.0×10^{-4} mol dm^{-3}. The plot of absorbance *versus* $c_{[Ru(CN)_5OH_2]^{3-}}$ clearly demonstrates that the reaction attains a steady rate after 5×10^{-4} mol dm^{-3} of $c_{[Ru(CN)_5OH_2]^{3-}}$ (Fig. 5). Thus, 5×10^{-4} mol dm^{-3} $c_{[Ru(CN)_5OH_2]^{3-}}$ is recommended for further study which provides appreciable change in the absorbance value.

Effect of temperature

The dependence of the reaction rate on the temperature was studied by the variation of the temperature in the range of 20 to 45 °C, keeping other reaction variables fixed at optimum values. Higher temperature was strictly avoided due to the possibility of degradation of the product $[Ru(CN)_5INH]^{3-}$. A distinct change in reaction rate was noticed at temperature 25 °C. Hence, the room temperature 25.00±0.01 °C was chosen for further study as an optimum temperature.

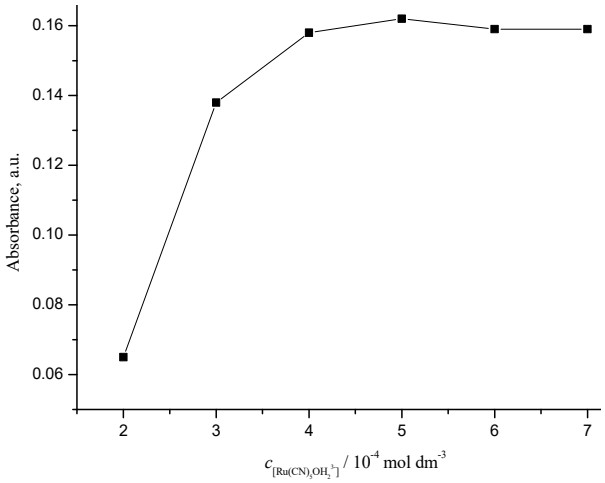

Fig. 5. Effect of $c_{[Ru(CN)_5OH_2]^{3-}}$ on the reaction rate under the reaction conditions: $c_{INH} = 5\times10^{-3}$mol dm^{-3}, pH 4.00±0.02, $\mu = 2\times10^{-2}$mol dm^{-3} ($NaClO_4$) and t = 25.00±0.01 °C.

*Effect of ionic strength (*μ*)*

The dependence of reaction rate on the ionic strength of the medium was investigated by varying $NaClO_4$ concentration (2.5×10^{-2}–2×10^{-1} mol dm^{-3}). The variation of ionic strength on the rate of reaction showed that the ionic strength of 2×10^{-2} mol dm^{-3} of $NaClO_4$ is optimum for the determination of the drug.

Kinetic determination of INH in pharmaceutical formulations

The fixed time procedure method was employed to obtain the calibration equations, under the optimum reaction conditions. A pre-selected time was chosen to record the absorbance for different concentrations of INH. The graph plotted between absorbance *versus* c_{INH} (Fig. 6) displays linear dependence in c_{INH} in the range of (1–20)$\times10^{-5}$ mol dm^{-3} (1.37–27.43 μg mL^{-1}), at different fixed times. Hence, the calibration graphs were obtained in the above-mentioned range. The calibration equations relating absorbance at fixed time (t_n = 2, 5 and 7 min) with c_{INH} have been presented in Table I, along with the values of correlation coefficient (r^2) and detection limit (3σ).

The precision and accuracy of the method.

Although the linearity is obtained in the same ranges of concentrations for all three fixed time intervals, a time of 5 min is recommended for further study, as it is when the best linearity was achieved (maximum correlation coefficients, r^2), which also satisfies the application of short analysis time.

The recovery experiment was performed to check the precision and the accuracy of the given method confirmed, adding the calculated INH amount in the range (3.060–27.382 μg mL^{-1}) in double distilled de-ionised water for the

recovery of drug. The results acquired are provided in Table II along with the errors and standard deviations (±*sd*). The recovered values were measured in the calibration range of 98–102 % using five independent determinations. The results tabulated in Table II show excellent reproducibility of the present method. In order to correspond to the calibration equations, the errors obtained during the measurement of the absorbance at 5 min, *i.e.*, A_5 is comparatively much less than those obtained during the study at 2 and 7 min (*i.e.*, A_2 and A_7), as the study of initial rate in case of A_5 is more adjacent than A_2 or A_7. Consequently, for further study a fixed time interval of 5 min is favoured, which is in accordance with the short analysis time, reproducibility and maximal value of correlation coefficients, r^2 as stated above (*vide infra*). Therefore, in the further investigation, at trace level calibration equation, A_5 was used for INH determination.

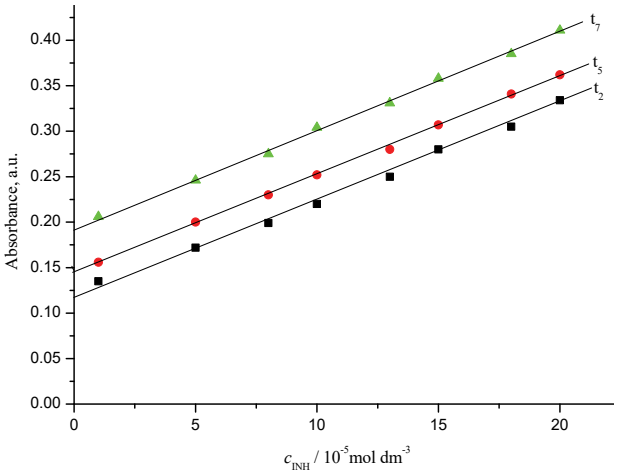

Fig. 6. Linear dependence of c_{INH} on the reaction rate at different times under the reaction conditions: $c_{[Ru(CN)_5OH_2]^{3-}} = 5\times10^{-4}$ mol dm^{-3}, pH 4.00±0.02, $\mu = 2\times10^{-2}$ mol dm^{-3} ($NaClO_4$) and t = 25.00±0.01 °C.

TABLE I. Determination of c_{INH} in the range of (1–20)×10^{-5} mol dm^{-3} under the optimum reaction conditions at $c_{[Ru(CN)_5OH_2]^{3-}} = 5\times10^{-4}$ mol dm^{-3}, pH 4.00±0.02, $\mu = 2\times10^{-2}$ mol dm^{-3} ($NaClO_4$) and t = 25.00±0.01 °C

Calibration equation	Detection limit, μg mL^{-1}	r^2
$A_2 = 1.05\times10^3 c_{INH} + 0.1193$	0.204	0.9957
$A_5 = 1.08\times10^3 c_{INH} + 0.1442$	0.210	0.9990
$A_7 = 1.08\times10^3 c_{INH} + 0.1929$	0.197	0.9983

Study of selectivity

In order to examine the applicability of the proposed method, the magnitude of the interference produced by some excipients in pharmaceutical agents was studied by the above mentioned procedure under the optimal reaction conditions.

The recovery experiments were performed in samples containing fixed concentration of INH (10 μg mL^{-1}) and a huge amount of diverse species. From the results, it is suggested that the chosen method is not affected by interferences of potential excipients even when their concentrations are quite high up to 1000 times (Table III). The tolerance limit (Excipient/INH) was evaluated for different excipients and the maximum error up to ±4 % was considered to be quite tolerable.

TABLE II. Accuracy and precision of c_{INH} determination by the proposed method under the reaction conditions: $c_{[Ru(CN)_5OH_2]^{3-}} = 5\times10^{-4}$ mol dm^{-3}, pH 4.00±0.02, $\mu = 2\times10^{-2}$ mol dm^{-3} ($NaClO_4$) and t = 25.00±0.01°C

c_{INH} added μg mL^{-1}	A_2		A_5		A_7	
	c_{INH} found[a]±sd[b] μg mL^{-1}	Error %	c_{INH} found[a]±sd[b] μg mL^{-1}	Error %	c_{INH} found[a]±sd[b] μg mL^{-1}	Error %
3.060	3.041±0.07	–0.62	3.052±0.03	–0.26	3.078±0.05	+0.59
4.441	4.476±0.04	+0.79	4.468±0.03	+0.61	4.432±0.04	–0.20
6.079	6.058±0.08	–0.34	6.068±0.16	–0.18	6.071±0.08	–0.13
7.402	7.312±0.05	–1.22	7.484±0.06	+1.11	7.436±0.04	+0.46
9.316	9.221±0.08	–1.02	9.186±0.05	–1.40	9.306±0.02	–0.11
13.212	13.362±0.51	+1.13	13.218±0.12	+0.04	13.196±0.26	–0.12
16.451	16.683±0.25	+1.41	16.422±0.02	–0.17	16.384±0.09	–0.41
19.268	19.182±0.18	–0.44	19.274±0.13	+0.03	19.564±0.10	+1.53
21.943	21.952±0.03	+0.04	21.881±0.44	–0.28	21.763±0.39	–0.82
25.324	25.262±0.62	–0.24	25.383±0.09	+0.23	25.427±0.23	+0.40
27.382	27.638±0.02	+0.93	27.394±0.33	+0.04	27.582±0.56	+0.73
Average		+0.42		–0.23		+0.17

[a]Mean of five determinations; [b]standard deviation of the mean of five determinations

TABLE III. Determination of INH concentration at 10 μg mL^{-1} level in presence of excipients under the optimum reaction conditions: $c_{[Ru(CN)_5OH_2]^{3-}} = 5\times10^{-4}$ mol dm^{-3}, pH 4.00±0.02, $\mu = 2\times10^{-2}$ mol dm^{-3} ($NaClO_4$) and t = 25.00±0.01 °C

Additive species	Tolerance limit	Recovery of drug±sd[a], %
Iodide	1000	100.2±0.8
Citrate	500	99.06±0.6
Talc	500	100.46±0.2
Sodium chloride	500	101.3±0.4
Glucose	1000	97.03±0.8
Lactose	500	99.6±0.6
Starch	500	100.2±0.2
Sodium phosphate	1000	101.4±0.6

[a]Standard deviation of the mean of five determinations

Application of the method for the assessment of INH in pharmaceutical preparations

To check the applicability of the developed kinetic spectrophotometric method it was successfully tested on six pharmaceutical samples for INH deter-

mination. The samples were prepared by the method discussed previously by Naik and co-workers.[35] Twenty tablets were weighed, grounded and the average mass per tablet was determined. The finely grounded tablet material was weighed accurately to 200 mg of INH, transferred and solubilized into different 100 mL flasks containing 70 mL de-ionised distilled water. The flasks containing dissolved INH were sonicated for 15 min and further diluted with 100 mL of de-ionised distilled water. In subsequent steps, the solutions were filtered using a 0.45 μm Millipore Whatmann filter paper. The concentration of the drugs within the calibration range was maintained by its accurate dilution using de-ionised distilled water. Further, the diluted samples were analysed directly using the calibration equation for INH determination. Analysis of six samples has been executed and presented in Table IV and the results indicate the quantitative and higher recovery of INH in the range of 99–101 % using size independent determinations.

TABLE IV. Determination of INH concentration in pharmaceutical preparations under the reaction conditions: $c_{[Ru(CN)_5OH_2]^{3-}} = 5\times10^{-4}$ mol dm^{-3}, pH 4.00±0.02, $\mu = 2\times10^{-2}$ mol dm^{-3} ($NaClO_4$) and t = 25.00±0.01 °C

Type of drug used	Amount taken, mg	Amount found±*sd*[a], mg		*t*-value	*F*-value
		Proposed method	Standard method[39]		
Solonex tablet (Macleods)	300	298.4±0.4	298.3±0.5	0.349	1.56
Solonex tablet (Macleods)	100	99.6±0.3	99.4±0.5	0.767	2.77
Isonex tablet (Pfizer)	100	99.6±0.3	99.5±0.4	0.447	1.77
Ipcazide tablet (IPCA)	100	99.2±0.3	99.0±0.4	0.894	1.77
Isokin tablet (Warner)	100	99.5±0.4	99.4±0.5	0.349	1.56
Isokin liquid (Warner)	20	19.6±0.3	19.4±0.5	0.767	2.77

[a]Standard deviation of the mean for five determinations

Validation of the proposed method by statistical analysis of the results in comparison with the official method

The Student's *t*-test and the variance ratio *F*-test was used to judge the performance of the proposed method statistically. At 95 % confidence level, the computed *t*-values from the Student's *t*-test and *F*-values from the variance ratio *F*-test do not exceed the theoretical values, *i.e.*, 2.776 (theoretical *t*-value for n = = 5) and 6.39 (theoretical *F*-value for n = 5), provided in Table IV. Thus, it signifies that there are no remarkable difference between the proposed method and the official method, assuring the suggested method is quite accurate and precise as the official method.[37] The result of INH analysis, using above recommended procedure, was found to be significantlly agreement with that obtained from the standard method.

CONCLUSION

The sugessted spectrophotometric method for INH determination is quite feasible when compared to other developed methods, which are reported in literature and it is of major interest in analytical pharmacy, because it offers the distinct possibility in the assay of isoniazid in pharmaceutical formulations. The main importance of the proposed method lies in the fact that it involves the use of the readily available reagents without any prior heating and without the use of any oxidant, catalyst and process of extraction. The short analysis time and the least interference due to excipients, good reproducibility and the accuracy of the method is further certified by the statistical parameters and by the recovery experiments performed on different samples. Hence, the present method could be used for the routine quality control in pharmaceutical industry.

Acknowledgement. Authors thank to the Head, Department of Chemistry, Lucknow University, Lucknow, for providing required departmental facilities to carry out the research work.

И З В О Д

ОДРЕЂИВАЊЕ ТРАГОВА ИЗОНИЈАЗИДА ПРИМЕНОМ КИНЕТИЧКЕ СПЕКТРОФОТОМЕТРИЈСКЕ МЕТОДЕ

RUPAL YADAV, INDRESH KUMAR и RADHEY MOHAN NAIK

Department of Chemistry, University of Lucknow, Lucknow, (U.P.) – 226007, India

Развијена је ефикасна и економична спектрофотометријска метода за одређивање трагова изонијазида (INH) у чистој форми, као и у фармацеутским формулацијама, базирана на лиганд-супституционој реакцији између INH и аквапентацијанофератног(II) јона ($[Ru(CN)_5OH_2]^{3-}$) у воденој средини на λ_{max} = 502 nm. Примењено је време процедуре за оптималне реакционе услове. Калибрациона једначина, за апсорбанцију на 502 nm, на фиксираном времену (t_n = 2, 5 и 7 min) и INH у линераном опсегу 1,37 до 27,43 μg mL^{-1}, примењена за одређивање трагова INH, у сагласности је са официналним и објављеним методама. Одређен је проценат приноса у анализи различитих фармацеутских узорака и износи 99–101 %. Резултати предложене методе указује на чињеницу да уобичајени адитиви не узрокују било какве интерференције. Резултати валидације предложене методе показују добру сагласност са истим добијеним официналном методом. Презентована метода је веома једноставна, репродуктивна, осетљива и може се применити за одређивање трагова INH у различитим узорцима без коришћења екстракционих агенаса.

(Примљено 13. маја 2020, ревидирано 27. фебруара, прихваћено 4. марта 2021)

REFERENCES

1. *Global Tuberculosis Report 2012*, World Health Organization, 2012 (https://apps.who.int/iris/handle/10665/75938)
2. A. Korokovals, J. H. Burckhalter, *J. Chem. Educ.* **54** (1977) A497. (https://dx.doi.org/10.1021/ed054pA497.2)
3. H. Meyer, J. Mally, *Monatsh. Chem.* **33** (1912) 393. (https://dx.doi.org/10.1007/BF01517946)
4. H. H. Fox, *Science* **116** (1952) 129 (https://www.jstor.org/stable/1680129)

5. C. Vilcheze,W. R. Jacobs, *Ann. Rev. Microbiol*. **61** (2007) 35 (https://dx.doi.org/10.1146/annurev.micro.61.111606.122346)
6. K. Johnsson, D. S. King, P. G. Schultz, *J. Am. Chem. Soc.* **117** (1995) 5009. (https://dx.doi.org/10.1021/ja00122a038)
7. D. A. Rozwarski, G. A. Grant, D. H. R. Barton, W. R. Jabobs, J. C. Sacchettini, *Science* **279** (1998) 98 (https://dx.doi.org/10.1126/science.279.5347.98)
8. A. M. El-Bbrashy, L. R. Elhussein, *Anal. Lett.* **30** (1997) 609 (https://dx.doi.org/10.1080/00032719708001805)
9. Q.-M. Li, Z.-J. Yang, *J. Chin. Chem. Soc.* **53** (2006) 383 (https://dx.doi.org/10.1002/jccs.200600049)
10. J. V. de Assis, M. G. Teixeira, C. G. P. Soares, J. F. Lopes, G. S. L. Carvalho, M. C. S. Lourenço, M. V. de Almeida, W. B. de Almeida, S. A. Fernandes, *Eur. J. Pharm. Sci.* **47** (2012) 539. (https://dx.doi.org/10.1016/j.ejps.2012.07.015)
11. J. A.García Bautista, J. V.García Mateo, J. M. Calatayud, *Anal. Let.* **31** (1988) 1209 (http://dx.doi.org/10.1080/00032719808002857)
12. Z. Q. Zhang, Z. X. Cao, X. M. He, X. M. Li, Y. F. Li, *J. Anal. Sci.* **12** (1996) 52 (http://en.cnki.com.cn/Article_en/CJFDTotal-FXKX199601015.htm)
13. J. Xi, B. Shi, X. Ai, Z. He, *J. Pharm. Biomed. Anal.* **36** (2004) 237 (https://dx.doi.org/10.1016/j.jpba.2004.05.021)
14. M. Acedo-Valenzuela, A. Espinosa-Mansilla, A. M. D. Pena, F. Canada-Canada, *Anal. Bioanal. Chem.* **374** (2002) 432. (http://dx.doi.org/10.1007/s00216-002-1494-5)
15. B. Haghighi, S. Bozorgzadeh, *Microchem. J.* **95** (2010) 192. (https://dx.doi.org/10.1016/j.microc.2009.11.012)
16. M. A. Karimi, M. Mazloum-Ardakani, M. H. Mashhadizadeh, F. Banifatemeh, *Croat. Chem. Acta* **82** (2009) 729 (https://hrcak.srce.hr/45534)
17. R. M. Kulkarni, D. C. Bilehal, S. T. Nandibewoor, *Anal. Sci*. **20** (2004)743 (https://dx.doi.org/10.2116/analsci.20.743)
18. M. R. Majidi, A. Jouyban, K. Asadpour-Zeynali, *J. Electroanal. Chem.* **89** (2006) 32 (https://dx.doi.org/10.1016/j.jelechem.2006.01.016)
19. J. S. Singh. *Res. J. Pharm. Technol.* **13** (2020) 4061 (https://doi.org/10.5958/0974-360X.2020.00718.0)
20. M. Y. Khuhawar, L. A. Zardari, *J. Food Drug Anal*. **14** (2006) 323 (http://iarscs.usindh.edu.pk/myk/papers/2006/1442p323328.pdf)
21. D. Hebel, S. Guermouche, M. H. Guermuche, *JPC-J. Planar. Chromat.* **10** (1997) 453 (http://pascal-francis.inist.fr/vibad/index.php?action=getRecordDetail&idt=2127215)
22. S. Guermouche, M. H. Guermouche, *J. Chromatogr. Sci*. **42** (2004) 250 (https://dx.doi.org/10.1093/chromsci/42.5.250)
23. M. Acedo-Valenzuela, A. Espinosa-Mansilla, A. M. D. Pena, F. Canada-Canada, *Anal. Bioanal. Chem*. **374** (2002) 432 (https://dx.doi.org/10.1007/s00216-002-1494-5)
24. I. L. Tsai, H. Y. Liu, P. H. Kuo, J. Y. Wang, L. J. Shen, C. H. Kuo, *Anal. Bioanal. Chem*. **401** (2011) 2205 (https://dx.doi.org/10.1007/s00216-011-5285-8)
25. M. Y. Khuhawar, F. M. A. Rind, *J. Chromatogr., B* **766** (2002) 357 (https://dx.doi.org/10.1016/S0378-4347(01)00510-2)
26. M. C. Gennaro, R. Calvino, C. Abrigo, *J. Chromatogr., B* **754** (2001) 477 (https://dx.doi.org/10.1016/S0378-4347(01)00037-8)
27. A. Safavi, M. Bagheri, *Spectrochim. Acta, A* **70** (2008)735 (https://dx.doi.org/10.1016/j.saa.2007.09.001)

28. G. F. Dos. S. Fernandes, H. Regina. Nunes Salgado, J. L. D.Santos, *Crit. Rev. Anal. Chem.* **47** (2017) 298 (https://doi.org/10.1080/10408347.2017.1281098)
29. R. M. Naik, A. Agarwal, S. Prasad, *Spectrochim. Acta, A* **74** (2009) 887 (https://dx.doi.org/10.1016/j.saa.2009.08.029)
30. R. M. Naik, A. Agarwal, S. Prasad, A. K. Verma, *Microchem. J.* **93** (2009) 43 (https://dx.doi.org/10.1016/j.microc.2009.04.006)
31. R. M. Naik, J. Sarkar, S. Prasad, *Microchem. J.* **88** (2008) 45 (https://dx.doi.org/10.1016/j.microc.2007.09.003)
32. S. Prasad, R. M. Naik, A. Srivastava, *Spectrochim. Acta, A* **70** (2008) 958 (https://dx.doi.org/10.1016/j.saa.2007.10.011)
33. R. M. Naik, B. Kumar, A. Asthana, *Spectrochim. Acta, A* **75** (2010) 1152 (https://dx.doi.org/10.1016/j.saa.2009.12.078)
34. A. Agarwal, S. Prasad, R. M. Naik, *Microchem. J.* **128** (2016) 181 (https://dx.doi.org/10.1016/j.microc.2016.04.005)
35. R. M. Naik, S. Prasad, B. Kumar, S. B. S. Yadav, A. Asthana, M. Yoshida, *Microchem. J.* **111** (2013) 108 (https://dx.doi.org/10.1016/j.microc.2013.02.011)
36. V. Chand, S. Prasad, *J .Hazard. Mater*. **165** (2009) 780 (https://dx.doi.org/10.1016/j.jhazmat.2008.10.076)
37. United States Pharmacopoeia XXIV**,** U.S.P. Convention, Rockville, MD20852, USA, 2000 (https://www.pharmaceuticalonline.com/doc/united-states-pharmacopoeia-xxiv-national-for-0001
38. A. I. Vogel, J. Bassett, *Vogel's text book of quantitative inorganic analysis*, 4th ed., Longman, New York, 1978 (ISBN-13: 978-0582463219)
39. R.C. Weast, *CRC Handbook of Chemistry and Physics*, 60th ed., CRC Press, Boca Raton, FL, 1979 (ISBN-13, https://www.biblio.com/9780849304606)
40. C. R. Johnson, R. E. Shepherd, *Inorg. Chem*. **22** (1983) 2439 (https://dx.doi.org/10.1021/ic00159a020)
41. K. W. Hicks, G. Chappelle, *Inorg. Chem*. **19** (1980) 1623 (https://dx.doi.org/10.1021/ic50208a038).

Journal of the Serbian Chemical Society
JSCS-info@shd.org.rs • www.shd.org.rs/JSCS
J. Serb. Chem. Soc.86 (5) 521–532 (2021)
JSCS–5439
Original scientific paper

Characterization of microcrystalline cellulose extracted from walnut and apricots shells by alkaline treatment

YASMINE MAHMOUD[1]*, ZITOUNI SAFIDINE[2] and NAIMA BELHANECHE-BENSEMRA[1]

[1]*Laboratoire des Sciences et Techniques de l'Environnement, Ecole Nationale Polytechnique, 10, Avenue des frères Oudek, BP 182 El-Harrach, Alger, Algeria and* [2]*Laboratoire de Chimie Macromoléculaire, Ecole Militaire Polytechnique, BP 17, Bordj El Bahri, Alger, Algeria*

(Received 6 August 2020, revised 1 February, accepted 10 February 2021)

Abstract: In this study, microcrystalline cellulose (MCC) was isolated from walnut and apricot shells (WS and AS) as agricultural wastes in order to use it as reinforcement in polymer composites. The microcrystalline cellulose was extracted by alkaline treatment and bleached by peroxide as an environmentally friendly treatment, called walnut cellulose (WC) and apricot cellulose (AC). The chemical composition of the samples was set according to the Technical Association of Pulp and Paper Industry (TAPP). After treatments, the *alpha*-cellulose content increased by about 23 % for the two used cellulose sources. The structural and morphological properties of the samples were investigated by Fourier transform infrared spectroscopy in the attenuated total reflectance mode (ATR-FTIR), optical microscopy (OM), X-ray diffraction and scanning electron microscopy (SEM). The crystallinity index values evaluated for WC and AC *via* X-ray diffraction were 86.4 and 80.3 %, respectively. The alkaline soluble fractions of walnut (ASW) and apricot (ASA) shells were recovered and characterized by OM and ATR-FTIR spectroscopy. Furthermore, their chemical composition was analyzed. The characterization and the properties of the WC and AC were similar to those of commercial MCC and MCC prepared in the literature from wood and some agricultural wastes.

Keywords: agricultural wastes; walnut shell; apricot shell; microcrystalline cellulose; crystallinity index.

INTRODUCTION

Over the last decade, biopolymers and natural fiber-reinforced plastics have become an interesting alternative to replace petroleum-based plastics. For this, academic and industrial research use wastes generated by agriculture in order to develop environmentally friendly composites with good thermal stability.[1,2] mechanical properties[1–3] and biodegradable.[2] These wastes consist of fibrous

* Corresponding author. E-mail: mahmoudyasmine9@gmail.com
https://doi.org/10.2298/JSC200806011M

vegetable tissues, mainly composed of cellulose, hemicelluloses and lignin, as the major constituents, considered as bio-composites, and of pectin, waxes, proteins, lipids, ash and extractive compounds that could be found as minor constituents.[3] Generally, a good dispersion of cellulose in the matrix of polymers enhance their mechanical and barrier properties of gases and vapors.[4] Thus, some researchers used lignin as a coupling agent to improve the interfacial adhesion between cellulose fibers and polymer matrices, and to enhance the thermal stability of the composites.[5] Recall that cellulose is the most abundant renewable polymer in the world. In cellulose fibers, the cellulosic chains are arranged in ordered crystallites and less-ordered amorphous regions, while lignin and hemicelluloses are amorphous components. Cellulose fibers found their first application in paper and clothing manufacturing, due to their high stiffness, low density and low cost. Cellulose fibers can be extracted from various agricultural wastes, such as wood, bamboo, flax, wheat,[6] almond shell,[7] corn stover,[8] sisal,[9] *etc.* For this, researchers developed different processes and treatments to valorize it, such as cellulose fibers,[10] cellulose crystals,[7] microfibers,[11] microcrystalline cellulose,[12] nanofibers,[6] or cellulose nanocrystals.[13]

The isolation of cellulose fibers requires the removal of other components, such as lignin, hemicelluloses and pectin, from natural fibers. However, the physicochemical properties depend on the method used and the raw material. Rajeshkumar *et al.*[14] proposed an environmental process to extract cellulose fibers from petioles of *Phoenix Sp.* plants. It consists of immersing these petioles in water for 15 to 20 days, then peeling them manually. On the other hand, Belouadah *et al.*[15] proposed the same procedure followed by manually brushing using a comb with metal teeth for *Lygeum spartum L*. Some researchers extracted cellulose fibers just by alkaline treatment.[16] However generally, the microcellulose fibers extracted by chemical treatment undergo alkaline treatment in order to remove the hemicelluloses and soluble lignin fraction, followed by bleaching with sodium hypochlorite in the presence of acetic acid, in order to remove the lignin part.[17] Chen *et al.*[6] and Reddy *et al.*[11] first dewaxed their samples with benzene and ethanol mixture using a Soxhlet apparatus. Cellulose crystals were extracted from almond shells by the same process but not dialyzed, vacuum-dried[7] and the cellulose nanocrystals derived from walnut shell were isolated using the same process reinforced by homogenization and ultrasonication processes.[13] Microcrystalline cellulose was isolated from palm oil fronds by an original process starting with alkaline hydrogen peroxide, followed by mechanical fibrillation, and then a solution of sodium chlorite was added to set pH to 4–5. Finally, this fiber was hydrolyzed in hydrochloric acid and the microcrystalline cellulose was dialyzed than dried in a vacuum oven.[18] Others precipitated the soluble lignin, after alkaline treatment or after alkaline peroxide, using HCl.[19]

The aim of the present work was to extract microcrystalline cellulose (MCC) by alkaline treatment and environmentally peroxide bleaching and remove the residual fraction after alkaline treatment from two agricultural residues (apricot and walnut shells). To that end, an alkaline treatment was carried out to remove the hemicelluloses and the soluble lignin fraction in order to isolate it, and peroxide bleaching was carried out to eliminate the insoluble lignin and isolate the MCC. To date, MCC has not been extracted from apricot shell and very few studies on walnut shells have been reported (Zheng *et al.*,[20] Harini *et al.*[21] and Hemmati *et al.*[13]). The structure and morphology of this cellulose were characterized by different techniques, *i.e.*, optical microscopy, scanning electron microscopy (SEM), Fourier transform infrared spectroscopy (FTIR), and X-ray diffraction (XRD). The removed fraction after alkaline treatment was analyzed using optical microscopy and FTIR spectroscopy. The chemical compositions of fibers and removed fraction were analyzed as per TAPPI standards.

EXPERIMENTAL

Materials

Walnut (WS) and apricot (AS) shell fibers were used as native cellulose fibers. The fruits come from a local market in Algiers (Algeria). Hydrogen peroxide (H_2O_2, 50 %) was purchased from Distrim. Hydrochloric acid (37 %) and sulfuric acid (96 %) were purchased from Carlo Erba Reagents. Sodium hydroxide (98 %) and acetic acid (99.8 %) were supplied by Scharlab S.L. Methanol was purchased from Chromanorm®. Ethanol (≥ 97 %), Ferroin solution ($C_{36}H_{24}FeN_6O_4S$, 0.1 wt. %) and sodium metasilicate pentahydrate (≥ 97 %) were supplied by Sigma–Aldrich. Benzene (99.5 %) was purchased from Riedel de Haen. Dichloromethane (CH_2Cl_2, 99.8 %) was supplied by VWR Prolabo. Sodium chlorite (80 %) was purchased from Fluka, Potassium dichromate (99.97 %) and ferrous ammonium sulfate hexahydrate ($(NH_4)_2Fe(SO_4)_2{\cdot}6H_2O$) were respectively supplied by Labosi and Biochem.

Extraction of cellulose fibers from walnut and apricot shells

The walnut and apricot shells were washed with distilled water five times at 90 °C during 2 h. After filtration, these shells were directly crushed with a knife grinder. Dried product was sieved and chemically purified according to the following steps: The powders of the walnut and apricot shells (WS and AS), between 40 and 100 μm in size, were treated with 5 % NaOH for 4 h at 80 °C in order to remove the alkaline-soluble components, such as soluble lignin, hemicelluloses and pectin. After this treatment, the fibers were centrifuged and washed with distilled water**.** The residual fibers were then dried in a hot air oven at 80 °C and crushed with a knife grinder. The definition of the sample code used is illustrated in Table I.

Recovery of alkaline soluble fraction

The alkaline soluble fraction of the WS and AS was precipitated at pH 1.5 adjusted by HCl from the supernatant solution of the alkaline treatment. The solution was centrifuged and washed with distilled water and the residual fraction was recuperated and dried at 60 °C.

Preparation of microcrystalline cellulose from walnut and apricot shells

The dried powder treated with alkaline solution was bleached using alkaline peroxide as an environmentally friendly treatment. In the alkaline media, H_2O_2 allows the formation of the hydroperoxide anion (–OOH) that reacts strongly with the chromophores and phenolic ring-

conjugated ethylenic or carbonyl groups present in lignin and remove them permanently.[22,23] The powder was treated with 5 % hydrogen peroxide solution in the presence of 1 % of sodium metasilicate pentahydrate, the pH of this solution was adjusted at 9.7±0.3 using 10 % of NaOH solution. During the first hour, the fibers were treated without any heating (exothermic reaction). The reaction was realized at 80°C during the following three hours.[22]

TABLE I. Definition of each sample code

Sample code	Definition of sample code
WS	Walnut shell
WC	Walnut cellulose
WTA	Alkaline soluble fraction of walnut
AS	Apricot shell
AC	Walnut cellulose
APA	Alkaline soluble fraction of apricot shell

The fibers were treated with H_2O_2 at pH 9.7±0.3, four times successively, in order to remove the greatest amount of lignin from the fiber and to obtain white colored fibers. The treated fibers were isolated by centrifugation and washed 3 times after each treatment. After the last treatment, the fibers were washed to a constant pH. Then they were dried at 60 °C, crushed with a knife grinder and sieved to produce fibers smaller than 40 μm.

Fiber characterization

The chemical composition of the untreated and chemically treated fibers was determined in accordance with the standards of the Technical Association of the Pulp and Paper Industry (TAPPI). The extractives were removed with an ethanol–benzene mixture according to the T 204 cm-97. The holocellulose content was determined as described by Yokoyama,[24] by the selective degradation of the lignin polymer by sodium chlorite at 70 °C in the presence of acetic acid. The α-cellulose content was determined by the removal of β and γ-cellulose from the holocellulose by alkaline extraction according to TAPPI T203 om-88. The acid soluble lignin content was analyzed by reaction with sulfuric acid using a standard method recommended in TAPPI-T222 om-88.

Fourier transform infrared spectroscopy (FTIR) measurements were performed using a Spectrum Two Perkin Elmer spectrometer, in the attenuated total reflectance (ATR) mode. The samples were scanned 10 times in the range 650–4000 cm^{-1}, with a resolution of 4 cm^{-1}. Microscopic photographs for the untreated WS, AS and for the WC, AC, WTA and APA were obtained using a Zeiss Axioskop coupled with an Optimas 1.5 picture analysis system. The magnification was 100× and 1000×. The surface morphologies of samples were investigated using a JEOL® JSM-6360 model with diverse voltages (5, 10, 15 kV) in order to observe the structure of the walnut and apricot shells (WS and AS) and the microcrystalline cellulose extracted from these shells (WC and AC). The crystallinity of the WS, WC, AS and AC was determined with a PANalytical XPERT-PRO diffractometer fitted with copper anode (Cu) under (λ = 1.5406 Å) wavelength and at 40 kV and 45 mA generator settings. Sample analysis was performed in the range 3–70° of the 2θ region. The crystallinity index (*CrI*) was calculated by the empirical method proposed by the Segal formula (1959) for native cellulose:[25]

$$CrI = 100\frac{I_{200} - I_{\text{am}}}{I_{200}} \quad (1)$$

where I_{200} denotes the maximum intensity of the 200 peak near to $2\theta = 22.5°$ and I_{am} is the intensity of the background scatter measures at 2θ value near 18°.

RESULTS AND DISCUSSION

Chemical composition

The chemical composition differs between different plants and different parts of the same plant, according to the geographic location, age, climate and soil conditions, among other factors. The chemical composition of the walnut and the apricot shells used for this study are presented in Table II.

TABLE II. Chemical analysis for untreated and treated wastes

Chemical composition	Content, %					
	Walnut			Apricot		
	WS	WC	WTA	AS	AC	APA
Extractives	4.3	1.8	13.7	4.4	1.3	11.2
Acid soluble lignin	35.4	13.4	66.7	32.5	11.0	60.9
Holocellulose	60.6	85.0	8.8	63.0	87.0	12.4
α-Cellulose	51.6	75.8	–	51.9	75.3	–
Hemicelluloses	9.0	9.1	–	11.1	11.7	–

The holocellulose contents found in walnut and apricot shell were in the range of 60.6 and 63 %, respectively. They were in the range found for Giant reed[12] and Posidonia balls[26] and somewhat higher those found for Posidonia leaves,[26] Sugar palm[27] and Peanut shell.[28] The contents of holocellulose and *alpha*-cellulose increased after treatment in the WS and AS. This enhancement is due to the extractive removal lignin after the set treatments. The contents of holocellulose were enhanced by 24.4 and 24 %, respectively, for WS and AS after treatment. At the same time, the content of *alpha*-cellulose increased by 18.2 and 23.4 % for WS and AS, respectively,.

The acid soluble lignin contents found, respectively, for WS and AS fibers were 35.4 and 32.5 %. These results seem considerably higher than the lignin content in bamboo and wood, (20–25 %)[6] and lower than that found in piassava, (≈48 %).[29] It is similar to the lignin content in Coir fiber (36.14 %)[30] and Peanut shell (35.2 %).[27]

The untreated fiber of walnut and apricot shells had a higher percentage of lignin, and a lower percentage of α-cellulose than WC and AC; the bleaching treatment cannot eliminate the total lignin content. The alkaline soluble fractions of the walnut and apricot shells (WTA and APA) contain considerably more lignin than hemicelluloses and the extracted fractions.

ATR-FTIR spectroscopic characterization

To study the effect of the treatment process on the composition of both WS and AS, FTIR spectra of each sample before treatment (the raw cellulose fiber),

after treatment (treated cellulose fiber) and after isolation of lignin (soluble alkaline fraction) were recorded and are compared in Fig. 1a and b.

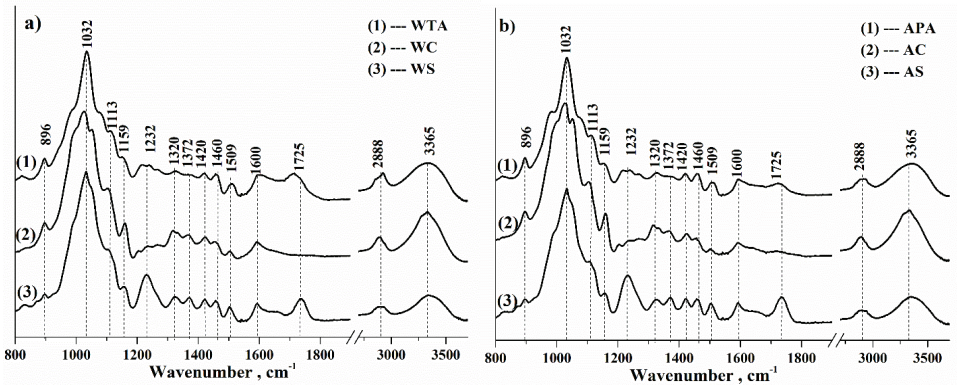

Fig. 1. FTIR spectra of WS, WC and WTA (a) and AS, AC and APA (b).

This FTIR spectroscopic analysis is in good agreement with the chemical analysis for all the samples. A wide band at around 3360 cm^{-1}, due to the stretching vibration of the hydrogen bonded hydroxyl group, is observed. It becomes more prominent for the AC and WC samples as the results of the increased availability and content of cellulose (75 % α-cellulose), *i.e.*, newly exposed cellulose hydroxyl groups.[31,32] The band at around 2900 cm^{-1} for all samples is attributed to the aliphatic C–H stretching vibration in methyl (CH_3) and methylene (CH_2) functional groups. The band at 1460 cm^{-1} represents the aromatic ring C=C of the phenyl propane group of lignin.[33] and the asymmetric bending of $–CH_3$ group,[34] while the band at 1422 cm^{-1} corresponds to vibrations of the aromatic skeletal and ring breathing with C–O stretching in lignin.[35] The intensity of these bends decreased after the treatment due to the removal of lignin. The band at around 1730 cm^{-1} was only observed in the spectra of WS and AS. It is attributed to the stretching vibration of the carbonyl group (C=O) of hemicelluloses present in these shells.[17,34] This band disappeared after alkaline and bleaching treatments, but just decreased for WTA and APA due to the reduction of hemicelluloses content. These results are in good agreement with the variation of the chemical composition according to the treatments performed, which are summarized in Table II. The bands at 1600 and 1509 cm^{-1}, significantly reduced in WC and AC, are attributed to symmetrical stretching vibration of C=C in plane of the aromatic ring present in lignin.[34] The band at 1230 cm^{-1}, which is present in the spectra of WS and AS, is attributed to the out of plane stretching vibration of C–O of aryl group present in the lignin part. It was significantly reduced in the WC and AC samples. This reduction is due to the removed lignin in WC and AC, as seen in Table II. The bands at 1320 and 1370

cm^{-1} are attributed, respectively, to the asymmetric and symmetric stretching of –COOH and the bonding of CH_2.[36] The band at 1032 cm^{-1} is attributed to the stretching mode of C–O–C bonds in the glucosidic rings.[36] The absorption band at 1155 cm^{-1} is attributed to C–O–C asymmetric stretch vibration in cellulose and hemicelluloses, while the band at 894 cm^{-1} is ascribed to the stretching vibration of C_1–O–C of β-(1-4)-glycosidic linkages in cellulose I and the amorphous fraction. The absorbance of these bands is more intense after alkaline and bleaching treatment due to the increase of cellulose content. The band at around 840 cm^{-1} associated with the band at 894 cm^{-1} observed in WTA and APA confirmed the presence of 1,2,4-tetrasubstituted aromatics in the lignin.[37]

Optical microscopy

Microscopic photographs at magnifications of 100× and 1000× were taken for the untreated WS, AS and for WC, AC, WTA and APA (Fig. 2). After the bleaching treatment, microscopic photographs at the same magnifications as for WC and AC were taken.

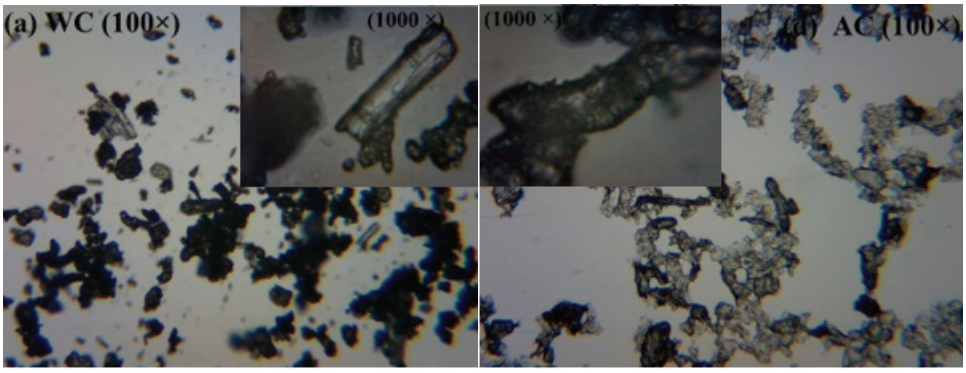

Fig. 2. Optical microscopic images of microcrystalline cellulose WC (a) and AC (b).

The microscopic photographs of untreated WS and AS show that a mixture of almost totally spherical shapes and some cylindrical shapes of inhomogeneous size, notably for the AS, were obtained. After treatment, microcrystalline cellulose particles of more cylindrical shape, in particular for WC, were obtained (Fig. 2). Their surface was smoother than that of the initial cellulose.

X-Ray diffraction analysis

The XRD results for microcrystalline cellulose derived from WS and AS before and after treatment are illustrated in Fig. 3a and b, respectively. The X-ray diffraction patterns of the samples are a combination of the diffraction of the amorphous region from lignin and hemicelluloses and ordered crystallites and less-ordered amorphous regions from the cellulosic chains. The XRD analysis of these samples (WS, WC, AS and AC) revealed a typical cellulose Iβ structure.[38]

They have three common peaks for all samples located at 2θ 14.8, 16.2 and 22.4° characterized the presence of cellulose I_{β}.[38,39]

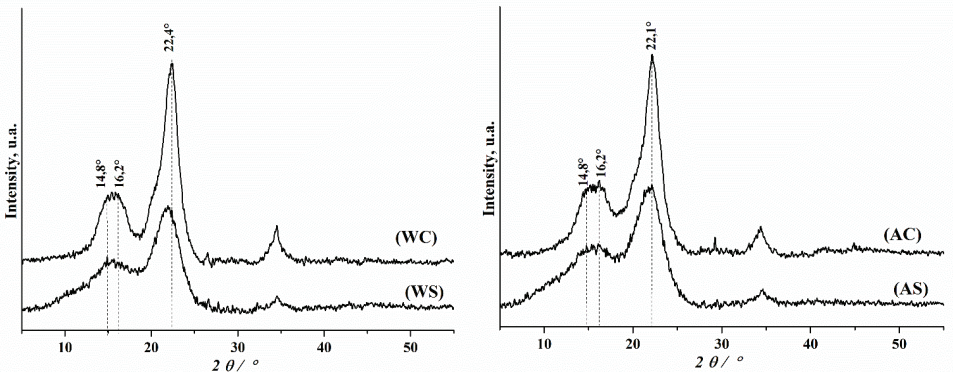

Fig. 3. XRD patterns for WS and WC (a) and AS and AC (b).

The peaks located at 2θ of 14.8 and 16.2° have the positions of (101) and (101-) crystallographic plane reflections, respectively,[40,41] the peak located at 22.4° has the positions of (200) crystallographic plane reflections.[38,39] The XRD results fit well with cellulose I_{β} crystals and the degrees of crystallinity were calculated using the Eq. (1). After chemical treatment of the raw materials, the crystallinity index increased from 55.2 and 60.4 %, for WS and AS to 86.4 and 80.3 % for WC and AC, respectively. Similar values were reported in literature.[42] These results indicate that after the treatments, the regions with a random amorphous structure, such as hemicelluloses and lignin, had dissolved and were removed.[43]

SEM characterization

SEM characterization was performed in order to evaluate the changes in surface morphology of WS and AS after treatment. Images of WS, AS, WC and AC are shown at 2000× magnification in Fig. 4.

The SEM images of the raw materials (WS and AS) show non-uniform particles with a rough and irregular surface. This irregularity may be attributed to the presence of impurities, waxes, hemicelluloses and lignin on its surface.[44] The presence of pores is clearly visible on the surface of WS and AS. After treatment, more uniform particles could be seen. The WC and AC have, respectively, more cylindrical and spherical shapes but not a completely rough surface due to the hydrogen-bonding present between the cellulose fibers.[45]

From the SEM micrographs of WS, AS, WC and AC (Fig. 4), it is evident that a profound morphological change in the shape of the raw material occurred after treatment. Yet, a high level of aggregation and agglomeration was observed due to the hydrophilic nature of the cellulose surface. The morphological shapes

of the microcrystalline cellulose WC and AC are similar to those of commercial microcrystalline cellulose reported by many authors, such as Karim.[45]

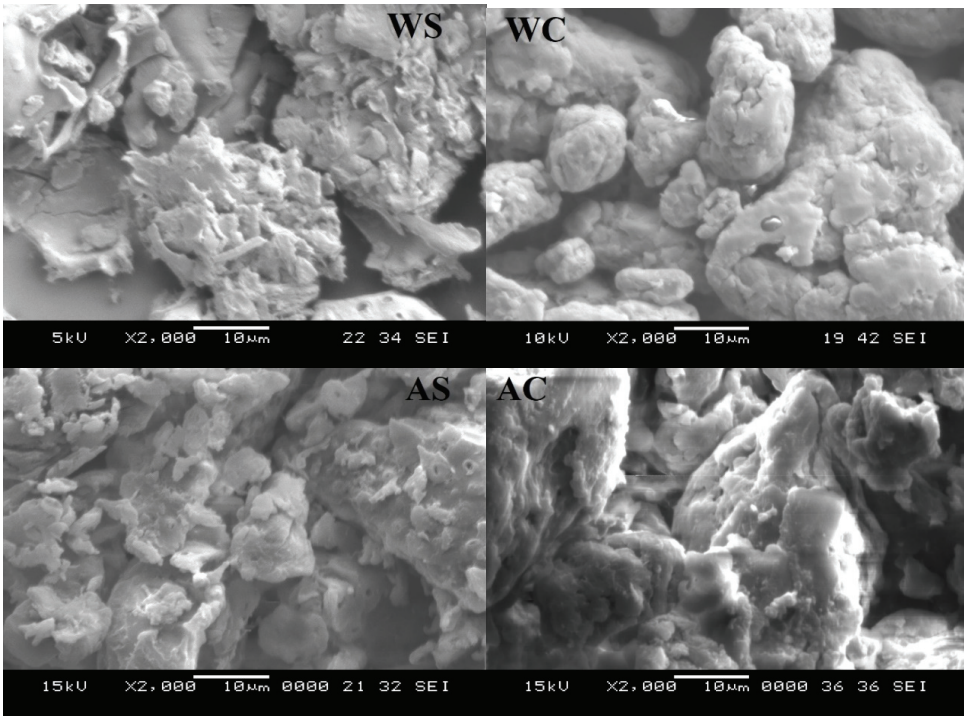

Fig. 4. Scanning electron microscopy images of different fiber surfaces (WS, WC, AS and AC).

CONCLUSIONS

MCC was successfully prepared from walnut and apricot shells, using only mercerization (NaOH) and bleaching with alkaline peroxide. The chemical compositions of WS and AS are very similar considering the nature of their similar sources. The chemical composition analysis showed an increasing trend in the holocellulose and α-cellulose contents after the chemical treatment. The α-cellulose content changed from 51.6 % in WS to 75.8 % in WC and from 51.9 % in AS to 75.3 % in AC. The ATR-FTIR spectra and chemical compositions are in agreement and show, on the one hand, that the ratio of lignin had considerably decreased by 35.4 and 32.5 % in WC and AC, respectively, but are not completely eliminated by the method used in this work. On the other hand, they show that alkaline treatment allows considerable quantities of extractable lignin to be extracted. This alkaline soluble fraction can easily be recovered by acid precipitation. Microscopic characterizations showed the morphological changes occurring on WS and AS fibers during the treatment. The X-ray diffraction analysis

showed a high crystallinity index (calculated by the Segal formula) of 86.4 and 80.3 % for WC and AC, respectively. This crystallinity index is good enough and in agreement with the crystallinity index of commercial MCC.

Acknowledgement. This work was supported by DGRSDT (Direction Générale de la Recherche Scientifique et du Développement Technologique (General Directorate of Scientific Research and Technological Development, Algeria)).

ИЗВОД

КАРАКТЕРИЗАЦИЈА МИКРОКРИСТАЛНЕ ЦЕЛУЛОЗЕ ЕКСТРАХОВАНЕ ИЗ ЉУСКИ ОРАХА И КОШТИЦА КАЈСИЈЕ АЛКАЛНИМ ТРЕТМАНОМ

YASMINE MAHMOUD[1], ZITOUNI SAFIDINE[2] и NAIMA BELHANECHE-BENSEMRA[1]

[1]Laboratoire des Sciences et Techniques de l'Environnement, Ecole Nationale Polytechnique, 10, Avenue des frères Oudek, BP 182 El-Harrach, Alger, Algeria и [2]Laboratoire de Chimie Macromoléculaire, Ecole Militaire Polytechnique, BP 17, Bordj El Bahri, Alger, Algeria

У овом раду је микрокристална целулоза (MCC) изолована из љуски ораха (WS) и коштица кајсије(AS) као пољопривредног отпада у циљу добијања пунилаца за ојачавање полимерних композита. MCC је екстрахована алкалним третманом и избељена пероксидом као еколошки прихватљивим поступком, чиме су добијени узорци целулозе WC (од љуске ораха) и AC (од коштице кајсије). Хемијски састав узорака је одређен према стандардима Техничке асоцијације индустрије целулозе и папира (TAPP). Након третмана, садржај α-целулозе се повећао за око 23 % за оба коришћена материјала. Структурна и морфолошка својства узорака су испитивана инфрацрвеном спектроскопијом са Фуријеовом трансформацијом у тоталној рефлексији (ATR-FTIR), оптичком микроскопијом (OM), рендгенском дифракционом анализом (XRD) и скенирајућом електронском микроскопијом (SEM). Индекс кристалиничности, одређен на основу резултата XRD анализе , износи 86,4 % за WC и 80,3 % за AC. Алкално растворљиве фракција WS и AS (ASW и ASA, редом) су издвојене и карактерисане оптичком микроскопијом и ATR-FTIR спектроскопијом. Такође, одређен је и хемијски састав. Карактеристике WC и AC су сличне карактеристикама комерцијалних MCC и узорака целулозе који су у литератури припремљени од дрвета и неких пољопривредних отпадних материјала.

(Примљено 6. августа 2020, ревидирано 1. фебруара, прихваћено 10. фебруара 2021)

REFERENCES

1. N. Saba, A. Safwan, M. L. Sanyang, F. Mohammad, M. Pervaiz, M. Jawaid, O. Y. Alothman, M. Sain, *Int. J. Biol. Macromol.* **102** (2017) 822 (https://doi.org/10.1016/j.ijbiomac.2017.04.074)
2. K. G. Satyanarayana, G. G. C. Arizaga, F. Wypych, *Prog. Polym. Sci.* **34** (2009) 982 (https://doi.org/10.1016/j.progpolymsci.2008.12.002)
3. M. El Achabya, Z. Kassaba, A. Barakatc, A. Aboulkasd, *Ind. Crops Prod.* **112** (2018) 499 (https://doi.org/10.1016/j.indcrop.2017.12.049)
4. L. Ugarte, A. Santamaria-Echart, S. Mastel, M. Autore, R. Hillenbrand, M. A. Corcuera, A. Eceiza, *Ind. Crops Prod.* **95** (2017) 564 (http://dx.doi.org/10.1016/j.indcrop.2016.11.011)
5. S. S. Nair, P.-Y. Kuo, H. Chen, N. Yan, *Ind. Crops Prod.* **100** (2017) 208 (http://dx.doi.org/10.1016/j.indcrop.2017.02.032)
6. W. Chen, H. Yu, Y. Liu, Y. Hai, M. Zhang, P. Chen, *Cellulose* **18** (2011) 433 (http://dx.doi.org/10.1007/s10570-011-9497-z)

7. N. Maaloul, R. B. Arfi, M. Rendueles, A. Ghorbal, M. Diaz, *J. Mater. Environ. Sci.* **8** (2017) 4171 (http://www.jmaterenvironsci.com/Document/vol8/vol8_N11/438-JMES-2556-Maaloul.pdf)
8. L. A. S. Costa, D. de J. Assis, G. V. P. Gomes, J. B. A. da Silva, A. F. Fonsêca, J. I. Druzian, *Mater. Today-Proc.* **2** (2015) 287 (https://doi.org/10.1016/j.matpr.2015.04.045)
9. J. I. Morán. V. A. Alvarez. V. P. Cyras. A. Vázquez, *Cellulose* **15** (2008) 149 (https://doi.org//10.1007/s10570-007-9145-9)
10. M. Maache, A. Bezazi, S. Amroune, F. Scarpac, A. Dufresne, *Carbohydr. Polym.* **171** (2017) 163 (http://dx.doi.org/10.1016/j.carbpol.2017.04.096)
11. J. P. Reddy, J.-W. Rhim, *J. Nat. Fibers* **15** (2018) 465 (https://doi.org/10.1080/15440478.2014.945227)
12. A. F. Tarchoun, D. Trache, T. M., Klapötke, M. Derradji, W. Bessa, *Cellulose* **26** (2019) 7635 (https://doi.org/10.1007/s10570-019-02672-x)
13. F. Hemmati, S. M. Jafari, M. Kashaninejad, M. B. Motlagh, *Int. J. Biol. Macromol.* **120** (2018) 1216 (https://doi.org/10.1016/j.ijbiomac.2018.09.012)
14. G. Rajeshkumar, V. Hariharan, T. P. Sathishkumar, *J. Ind. Text.* **46** (2016) 667 (https://doi.org/10.1177/1528083715591581)
15. Z. Belouadah, A. Ati, M. Rokbi, *Carbohydr. Polym.* **134** (2015) 429 (http://dx.doi.org/10.1016/j.carbpol.2015.08.024)
16. P. Senthamaraikannan, M. Kathiresan, *Carbohydr. Polym.* **186** (2018) 332 (https://doi.org/10.1016/j.carbpol.2018.01.072)
17. I. M. Fareez, N. A. Ibrahim, W. M. H. W. Yaacob, N. A. M. Razali, A. H. Jasni, F. A. Aziz, *Cellulose* **25** (2018) 4407 (https://doi.org/10.1007/s10570-018-1878-0)
18. A. F. Owolabi, M. K. M. Haafiz, Md. S. Hossainc, M. H. Hussind, M. R. N. Fazita, *Int. J. Biol. Macromol.* **95** (2017) 1228 (http://dx.doi.org/10.1016/j.ijbiomac.2016.11.016)
19. R. C. Sun, X. F. Sun, J. L. Wen, *J Agric. Food Chem.* **49** (2001) 5322 (http://dx.doi.org/10.1021/jf010645y)
20. D. Zheng, Y. Zhang, Y. Guo, J. Yue, *Polymers **11*** (2019) *1130* (https://doi.org/10.3390/polym11071130)
21. K. Harini, C. C. Mohan, *Int. J. Biol. Macromol.* **163** (2020) 1375 (https://doi.org/10.1016/j.ijbiomac.2020.07.239)
22. R. C. Sun, J. M. Fang, J. Tomkinson, *Ind. Crop. Prod.* **12** (2000) 71 (https://doi.org/10.1016/S0926-6690(00)00039-X)
23. S. I. Mussatto, G. J. M. Rocha, I. C. Roberto, *Cellulose* **15** (2008) 641 (https://doi.org/10.1007/s10570-008-9198-4)
24. T. Yokoyama, J. F. Kadla, H.-M. Chang, *J. Agric. Food Chem.* **50** (2002) 1040 (https://doi.org/10.1021/jf011173q)
25. L. Segal, J. J. Creely, A. E. Martin, C. M. Conrad, *Text. Res. J.* **29** (1959) 786 (https://doi.org/10.1177/004051755902901003)
26. F. Bettaieb, R. Khiari, M. L. Hassan, M. N. Belgacem, J. Bras, A. Dufresne, M. F. Mhenni, *Ind. Crops Prod.* **72** (2015) 175 (https://doi.org/10.1016/j.indcrop.2014.12.038)
27. R. Ilyas, S. Sapuan, M. Ishak, *Carbohydr. Polym.* **181** (2018) 1038 (https://doi.org/10.1016/j.carbpol.2017.11.045)
28. S. Naduparambath, E. Purushothaman, *Cellulose* **23** (2016) 1803 (https://doi.org/10.1007/s10570-016-0904-3)
29. J. R. M. d'Almeida, R. C. M. P. Aquino, S. N. Monteiro, *Compos., A* **37** (2006) 1473 (https://doi.org/10.1016/j.compositesa.2005.03.035)

30. A. Espert, F. Vilaplana, S. Karlsson, *Compos., A* **35** (2004) 1267 (https://doi.org/10.1016/j.compositesa.2004.04.004)
31. J.-H. Chen, J.-G. Liu, Y.-Q. Su, Z.-H. Xu, M.-C. Li, R.-F. Ying, J.-Q. Wu, *Carbohydr. Polym.* **206** (2019) 616 (https://doi.org/10.1016/j.carbpol.2018.11.024)
32. L. Bergamonti, M. Potenza, A. Haghighi Poshtiri, A. Lorenzi, A. M. Sanangelantoni, L. Lazzarini, P. P. Lottici, C. Graiff, *Carbohydr. Polym.* **231** (2020) 115773 (https://doi.org/10.1016/j.carbpol.2019.115773)
33. B. D. Mistry, *A Handbook of Spectroscopic Data Chemistry (UV, IR, PMR, 13CNMR and Mass Spectroscopy)*, Oxford Book Co., Jaipur, 2009, p. 42
34. C. Yadav, A. Saini, P. K. Maji, *Carbohydr. Polym.* **165** (2017) 276 (http://dx.doi.org/10.1016/j.carbpol.2017.02.049)
35. B. H. Stuart, *Infrared spectroscopy: fundamentals and applications*, Wiley, Chichester, 2004, p. 77
36. F. Niu, M. Li, Q. Huang, X. Zhang, W. Pan, J. Yang, J. Li, *Carbohydr. Polym.* **165** (2017) 197 (http://dx.doi.org/10.1016/j.carbpol.2017.02.048)
37. Boukir, S. Fellak, P. Doumenq, *Heliyon*. **5** (2019) e02477 (http://dx.doi.org/10.1016/j.heliyon.2019.e02477)
38. A. D. French, *Cellulose* **21** (2014) 885 (http://dx.doi.org/10.1007/s10570-013-0030-4)
39. M.-J. Chen, X.-Q. Zhang, A. Matharu, E. Li, R.-M. Melo, C.-F. Liu, Q.-S. Shi, *ACS Sustain. Chem. Eng.* **5** (2017) 7278 (http://dx.doi.org/10.1021/acssuschemeng.7b01526)
40. R. Liu, H. Yu, Y. Huang, *Cellulose* **12** (2005) 25 (http://dx.doi.org/10.1007/s10570-004-0955-8)
41. K. Singh, T. J. M. Sinha, S. Srivastava, *Int. J. Miner. Process.* **139** (2015) 51 (http://dx.doi.org/10.1016/j.minpro.2015.04.014)
42. K. Zhang, Y. Zhang, D. Yan, C. Zhang, S. Nie, *Cellulose* **25** (2018) 5049 (http://dx.doi.org/10.1007/s10570-018-1928-7)
43. R. Li, J. Fei, Y. Cai, Y. Li, J. Feng, J. Yao, *Carbohydr. Polym*. **76** (2009) 94 (http://dx.doi.org/10.1016/j.carbpol.2008.09.034)
44. A. P. B. Gonçalves, C. S. de Miranda, D. H. Guimarães, J. C. de Oliveira, A. M. F. Cruza, F. L. B. M. da Silva, S. Luporinia, N. M. José, *Mater. Res.* **18** (2015) 205 (http://dx.doi.org/10.1590/1516-1439.366414)
45. M. Z. Karim, Z. Z. Chowdhury, S. B. Abd Hamid, M. E. Ali, *Materials* **7** (2014) 6982 (http://dx.doi.org/10.3390/ma7106982).

Journal of the Serbian Chemical Society
JSCS-info@shd.org.rs • www.shd.org.rs/JSCS
J. Serb. Chem. Soc. *86* (5) 533–545 (2021)
JSCS–5440
Original scientific paper

Operating parameter optimization of cell surface hydrophobicity test for ureolytic bacteria

OLJA LJ. ŠOVLJANSKI[1], LATO L. PEZO[2], ANA M. TOMIĆ[1]*, ALEKSANDRA S. RANITOVIĆ[1], DRAGOLJUB D. CVETKOVIĆ[1] and SINIŠA L. MARKOV[1]

[1]*University of Novi Sad, Faculty of Technology Novi Sad, Laboratory of Microbiology, Bulevard cara Lazara 1, Novi Sad, Serbia and* [2]*University of Belgrade, Institute of General and Physical Chemistry, Studenski trg 12/V, Belgrade, Serbia*

(Received 13 August, accepted 10 December 2020)

Abstract: As one of the main non-covalent relations in microbiological-based systems, cell surface hydrophobicity (CSH) can be observed as a relevant parameter for biodegradation capability and suggested bacterial behaviour and biofilm formation during a bioremediation process. On the other hand, the role of ureolytic bacteria in bioremediation has subsequently led to the examination of this bacterial type in different engineering fields. In order to optimize the operating parameters of microbial adhesion to hydrocarbons test (MATH) for ureolytic bacteria, Box–Behnken experimental design was conducted for five ureolytic bacteria isolated from soils, as well as for the reference strain *Sporosarcina pasteurii* DSM 33. The optimization was completed with and without the essential substrate for the targeted metabolic reaction, with the aim to compare differences in bacterial hydrophobicity. A vortex time of 2 min, a hydrocarbon volume of 0.5 mL, and a phase separation time of 15 min are recommended as MATH operating parameters for all tested ureolytic bacteria. Although all bacteria are hydrophobic, lower CSH values in the presence of urea were observed for the same bacterium, which could be explained by the interaction of urea with the organic phase of the separation system, as well as a rapid ureolysis process that also occurs during the application of ureolytic bacteria in biotechnology systems.

Keywords: MATH test; adhesion potential; phase separation time; hydrocarbon volume; vortex time; *Sporosarcina pasteurii*

INTRODUCTION

The evidence of the contribution of ureolytic bacteria in bioremediation processes has subsequently led to the examination of these bacteria in a variety of engineering fields. Applications of ureolytic bacteria are found in traditional techniques of soil bioremediation and removal of metals ions and colours from

* Corresponding author. E-mail: anav@uns.ac.rs
https://doi.org/10.2298/JSC200813082S

industrial effluents.[1–3] In addition to these conventional strategies that are dependent on the biodegradation of organic pollutants, the use of ureolytic bacteria has been suggested for civil engineering bio-based processes, such as biocalcification, biomineralization or bioconsolidation of different materials (from repairing of cultural heritage substrates to development of a new generation of cement-based materials).[4–7] In the past decades, isolation of ureolytic bacteria from nature has supported the investigation of metabolic activity as well as the potential role of viable ureolytic cells in targeted engineering processes. Besides the widespread application possibility of ureolytic bacteria, the role of concentration and bacterial cell in a bioremediation system were always the main questions for engineers.

The hydrophobicity of the surface of ureolytic bacterial cell could contribute to adhesion and biofilm formation on different abiotic and biotic surfaces, as well as it could improve beneficial processes, such as degradation of organic contaminants in nature or removal of heavy metal ions in industrial waste effluents.[8] Furthermore, direct hydrophobic interaction with the substrate allows ureolytic bacteria to modify the surface contact and affect a modification in bacterial behaviour. One of the necessities for a bioremediation process is using non-pathogenic microorganisms that have defined behaviour in terms of biofilm potential,[9] and determination of cell surface hydrophobicity could be one of the initial parameters of the appearance of biofilm at the treated site during bioremediation.

Cell surface hydrophobicity has a significant role in the adhesion potential of bacteria on a surface. Understanding this phenomenon is essential for the application of a specific type of bacteria in different engineered processes, such as food processing, environmental engineering, biological-based systems, *etc.*[10,11] Bacteria exist predominantly as a population of microbial biofilms in the environment, due to their high adhesion capacity and possibility to aggregate on a different surface.[12] Since microbial adhesion is considered as the initial stage of biofilm formation, hydrophobic bacteria have been involved in the interaction with surfaces, accumulation of different pollutants around cells, and their decomposition.[8] A high level of cell surface hydrophobicity strongly affects biofilm formation, influencing the sustainability of diverse and complex social cooperation and coordination inside a biofilm.[13]

As a laboratory assay, the microbial adhesion to the hydrocarbons test (MATH) is often used for defining the cell surface hydrophobicity (CSH) of different bacteria, such as *Pseudomonas*, *Bacillus*, *Escherichia*, *Staphylococcus*, *etc.*[11,14–16] This test is based on the partitioning of bacterial cells between the hydrocarbon and aqueous phase of the separation system. The results of spectrophotometric measurement of the aqueous phase before and after vortex mixing of a bacterial suspension could be used as a quick assessment of hydrophobicity and therefore has been used in different fields, such as bioremediation in a waste-

water system, biofiltration, biomedical science, food and dairy industry, *etc.*[17–19] As a result of the MATH test, cell surface hydrophobicity is presented as the percentage of bacterial cells separated into a hydrocarbon phase.[18]

Although the MATH test is frequently used in laboratory conditions, this method is liable to be influenced by variable operating conditions whereby the obtained values could vary by more than ten times and there is no unique or standard protocol in any scientific paper. For example, for vortex time as one of main MATH operating parameters is recommended from 10 s[20] through 60 s[21] and 120[22] to 300 s.[23] A similar situation exits for the employed phase separation time which is often 5, 15, 30 or 45 min,[14,24–26] as well as from 0.04 to 4 mL for the hydrocarbon volume.[11] Additionally, Saini[11] reported that the selection of hydrocarbon, wavelength, and suspension media could be used as variables in the MATH test, but the mentioned parameters do not exert a high influence on the results compared to the vortex time, hydrocarbon volume, and phase separation time as the main MATH operating parameters.

The optimization of laboratory assay, such as the MATH test, allows a comparative analysis of the influence of operating parameters and their interaction through quantification of the effect of operating parameters on the final result. A limited number of scientific studies have described a comparative analysis of operating parameters for the MATH test. It should be noticed that no specific experimental design has been established for this laboratory assay setting. Furthermore, no growth media with and without the addition of essential substrate for optimization of MATH operating parameters have yet been established for specific bacteria.

Therefore, this study aims to compare the effects of three MATH operating parameters (vortex duration, phase separation time, and hydrocarbon volume) on cell surface hydrophobicity by a Box–Behnken experimental design for six ureolytic bacteria. Considering that urea is always required as a nitrogen source when it comes to the utilization of ureolytic bacteria in engineering processes, the additional aim was observing differences of cell surface hydrophobicity between incubation of bacterial cultures in nutrient media with and without the addition of urea.

EXPERIMENTAL

The bacterial culture of five ureolytic bacteria from soil[27] and the well-known ureolytic strain *Sporosarcina pasteurii* DSM33 (DSMZ – German Collection of Microorganisms and Cell Cultures, Braunschweig, Germany) were used for this experiment. The selected bacterial isolates (named as II_8, II_{10}, III_{11}, III_{15} and IV_5) previously showed high ureolytic activity compared to the mentioned reference strain.[27] The nutrient media for bacterial growth were TSB (Tryptone Soya Broth, HiMedia, Mumbai, India) with and without the addition of 20 % urea. The bacterial cultures were aerobically incubated overnight at 30 °C and centrifuged at 13000 rpm for 15 min in a Hettich Rotina 380 R centrifuge (Tuttlingen, Germany). The cell pellets were washed and resuspended in the same growth media.

The MATH setup was performed at room temperature. Controls for the MATH test experiments ($A_{control}$) were the absorbance of prepared microbial suspensions in previous steps. An aliquot of 4 mL bacterial suspension (approx. 10^6 CFU mL^{-1}) was added in the selected hydrocarbon volume in a glass tube, vortexed, and hydrocarbon–aqueous phase separation was allowed. Hexadecane (Sigma–Aldrich) was used as the hydrocarbon. The aqueous phase was used for measuring the absorbance (A_{MATH}, wavelength = 600 nm) using a UV--1800 UV/Vis spectrophotometer (Shimadzu, Kyoto, Japan). All measurements were performed in triplicate. The non-inoculated nutrient media were used as the blank for the absorbance measurements and their absorbance was compared to the control cultures. The change in aqueous phase absorbance due to hydrocarbon addition represented as a measure of bacterial cells that separated into the hydrocarbon phase. Cell surface hydrophobicity (*CSH*) was calculated using Eq. (1):

$$CSH = 100\frac{A_{control} - A_{MATH}}{A_{control}} \quad (1)$$

Three operating parameters (X_1 – vortex time, X_2 – hydrocarbon volume, and X_3 – phase separation time) were independent factors in the selected Box–Behnken experimental design. The cell surface hydrophobicity was chosen as the dependent factor (Y_k). The experimental design is given as % in Table I with three levels for each independent factor, coded as –1, 0, and +1, which corresponded to the lower, middle, and higher levels, respectively. The response surface method was used to evaluate the influence of the MATH operating parameters on cell surface hydrophobicity for each bacterial strain. The relations between the independent factors and the responses were calculated by a second-order polynomial, Eq. (2):

$$Y_k = b_0 + \sum_{i=1}^{3} b_i X_i + \sum_{i=1}^{3} b_{ii} X_i^2 + \sum_{i=1, j=i+1}^{3} b_{ij} X_i X_j \text{ , k=10} \quad (2)$$

where Y_k is the defined response, b_0 is the intercept, b_i, $b_{ii,}$ and b_{ij} are the linear, quadratic, and interaction regression coefficients, respectively, while X_i and X_j are the varied factors.

Standard scores were calculated for each assay and were used for complex comparison of observed samples, regarding the obtained results for cell adhesion hydrophobicity. The ranking procedure between different samples was performed, based upon the ratio of raw data and extreme values for each applied assay,[28] according to Eq. (3) in case of "the higher, the better" criteria (used for cell adhesion hydrophobicity parameters) or Eq. (4) in case of "the lower, the better" criteria (used for factor scores), where x_i represents the raw data:

$$\overline{x_i} = \frac{x_i - \min\limits_i x_i}{\max\limits_i x_i - \min\limits_i x_i}, \quad \forall i \quad (3)$$

$$\overline{x_i} = 1 - \frac{x_i - \min\limits_i x_i}{\max\limits_i x_i - \min\limits_i x_i}, \quad \forall i \quad (4)$$

The higher cell adhesion hydrophobicity was considered as a positive score, while the lower factors scores were considered as positive for final product properties. The separate SS values for nutrient media without urea and nutrient media with the addition of 20 % urea were calculated. An optimization procedure was performed using Microsoft Excel 2007 to determine the workable optimum conditions.

TABLE I. Box–Behnken experimental design for the MATH assay

Experiment	Coded factor level			Varied factor value		
	X_1	X_2	X_3	Vortex time min	Hexadecane volume mL	Phase separation time min
1	–1	–1	0	0.5	0.5	30
2	1	–1	0	4	0.5	30
3	–1	1	0	0.5	4	30
4	1	1	0	4	4	30
5	–1	0	–1	0.5	2	15
6	1	0	–1	4	2	15
7	–1	0	1	0.5	2	45
8	1	0	1	4	2	45
9	0	–1	–1	2	0.5	15
10	0	1	–1	2	4	15
11	0	–1	1	2	0.5	45
12	0	1	1	2	4	45
13	0	0	0	2	2	30
14	0	0	0	2	2	30
15	0	0	0	2	2	30

Statistical analyses were done using Statistica software, v. 13.2 (Dell, Round Rock, TX, USA). The influence of examined factors, as well as their interaction, was studied by comparing the sum of squares values for each of the coefficients in the second-order polynomial (SOP) model. The response surface plots were drawn using the same software for a constant value of hydrocarbon volume (2.25 mL) and varied values of the other two factors (vortex time and phase separation time).

RESULTS AND DISCUSSION

To the best of our knowledge, no MATH operating parameters have to date been established for the determination of cell adhesion hydrophobicity (CSH) of ureolytic bacterial strains isolated from nature,. Additionally, using an essential substrate during the experimental setup allows a comparative analysis of cell surface hydrophobicity and defines potential bacterial behaviour of selected bacteria during the bioremediation process. This step could be very important because ureolytic bacteria always require urea as a nitrogen source to realize the stated targeted metabolic process– ureolysis.[3]

In this study, the MATH operating parameters and tested range for CSH examination of the selected ureolytic bacteria (reference and wild strains) were chosen from relevant scientific papers.[18–24] The vortex time, hydrocarbon volume, and phase separation time are the most variable operating parameters that strongly affected the results of the MATH test.[11] In order to determine the MATH operating parameters for the targeted bacterial type, experiments were performed according to Box Behnken design. The obtained results for all six bacteria in both tested nutrient media (with and without the addition of 20 % urea) are given in Table II.

TABLE II. The obtained results for cell adhesion hydrophobicity (%) of ureolytic bacteria by the Box–Behnken experimental design; –U: without urea addition, +U: with the addition of 20 % urea

Design	Reference strain		Wild ureolytic strain									
	S. pasteurii DSM33		II_8		II_{10}		III_{11}		III_{15}		IV_5	
	–U	+U	–U	+U	–U	+U	–U	+U	–U	+U	–U	+U
1	8.2	3.7	9.1	9.2	2.4	1.6	11.1	8.0	1.9	4.5	21.0	18.3
2	23.1	15.2	27.1	26.7	11.2	10.5	21.4	18.4	5.6	21.1	18.3	15.9
3	7.6	5.1	8.3	7.7	1.9	1.3	12.3	9.4	0.7	14.2	22.2	19.4
4	25.0	17.1	31.2	30.7	7.0	–0.2	19.4	19.5	2.6	–0.5	19.3	16.0
5	3.4	1.9	10.2	11.4	1.2	6.9	5.6	5.7	–0.3	10.9	17.6	15.4
6	17.1	13.7	19.4	18.8	10.1	2.2	17.0	17.8	1.2	8.8	18.7	15.9
7	9.2	4.9	11.1	11.7	3.3	8.7	15.2	11.1	4.7	15.3	24.7	21.6
8	20.2	13.3	26.7	25.0	12.6	2.8	14.7	10.1	2.8	5.6	21.8	19.1
9	10.1	7.1	17.7	16.6	4.0	5.2	15.2	13.3	1.5	10.7	22.4	19.6
10	14.1	7.7	17.2	16.9	7.5	5.6	19.2	14.4	3.0	11.7	19.2	16.6
11	14.9	5.9	22.1	19.0	8.2	6.4	22.4	16.9	3.3	13.8	23.1	16.7
12	16.2	9.0	23.0	24.5	9.5	6.5	21.4	17.0	4.1	14.1	25.0	20.2
13	16.5	9.85	23.9	24.7	9.1	6.0	22.0	17.4	4.4	13.8	20.0	16.8
14	16.35	9.71	24.0	24.5	8.9	5.9	23.1	16.8	3.9	13.3	18.5	17.8
15	16.2	9.9	23.9	23.8	8.8	6.0	22.7	17.2	4.05	13.4	19.6	16.2

Principal component analysis (PCA) of the presented data explained that the first two components (PC1 and PC2) accounted for 75.09 % of the total variance (PC1: 53.69 % + PC2: 21.40 %) in the twelve variables (cell surface hydrophobicity of the different bacterial strains). Considering the map of the PCA performed on the data (Fig. 1), the cell surface hydrophobicity of the reference strain incubated in nutrient media with and without urea (which contributed 11.7 and 14.0 % of the total variance, based on correlations, respectively), bacterial strains II_8 (14.0 and 14.1 % for nutrient media with and without urea, respectively), III_{11} (12.4 and 11.2 % for nutrient media with and without urea, respectively) as well as II_{10} and III_{15} incubated in the absence of urea (12.2 and 7.1 %, respectively) exhibited positive scores according to the first principal component.

The positive contribution to the second principal component calculation was observed in the following cases: bacterial strains II_{10} incubated with urea addition (24.6 % of the total variance, based on correlations), III_{15} incubated without urea addition (15.3 %), III_{15} incubated with urea addition (26.6 %), and IV_5 incubated with and without urea addition (10.6 and 12.1 %, respectively).

ANOVA calculation was conducted for the obtained second-order polynomial (SOP) models for incubation of selected ureolytic bacteria in nutrient medium TSB without the addition of urea, and the response variables were tested against the impact of factor variables (Table III).

According to the obtained results, ANOVA analysis revealed that the linear term of vortex time (X_1) considerably influenced the SOP model predictions of the

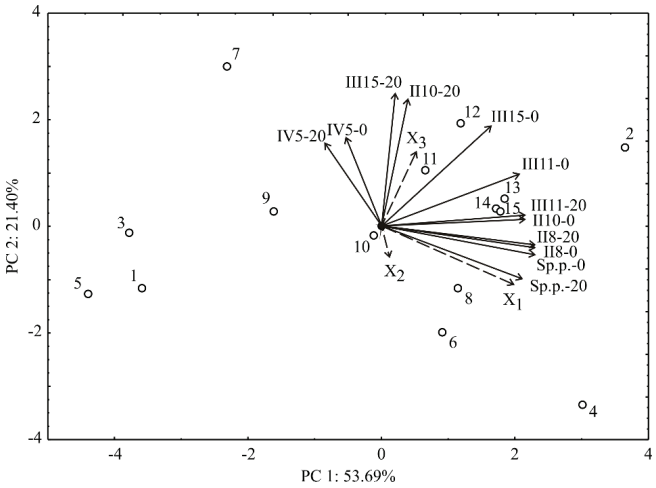

Fig. 1. PCA ordination of the variables based on component correlations.

TABLE III. ANOVA calculation for experiments with ureolytic bacteria nutrient media without urea (the sum of squares is presented); $^{+}$: statistically significant at $p<0.01$ level; *: $p<0.05$ level; **: $p<0.10$ level

Variable	Degrees of freedom	Reference strain	Wild ureolytic strain				
		S. pasteurii DSM33	II_8	II_{10}	III_{11}	III_{15}	IV_5
X_1	1	407.568^{+}	548.560^{+}	122.367^{+}	96.193^{+}	3.024	6.834**
X_1^2	1	12.933*	100.911^{+}	22.450*	178.869^{+}	5.612	0.360
X_2	1	6.040	2.592	0.038	0.392	0.576	0.093
X_2^2	1	0.500	3.623	7.230	0.038	0.205	5.836
X_3	1	27.668*	46.649*	13.616**	25.000*	9.734**	34.810^{+}
X_3^2	1	33.352^{+}	32.974**	0.214	33.117*	2.829	11.679*
$X_1 \times X_2$	1	1.862	9.592	5.379	2.216	0.826	0.012
$X_1 \times X_3$	1	1.655	9.738	0.017	36.230^{+}	2.449	3.364
$X_2 \times X_3$	1	2.037	0.638	1.074	6.118	0.246	5.698
Error	5	9.455	30.772	12.159	8.203	11.942	7.603
r^2		0.981	0.957	0.933	0.978	0.684	0.901

reference strain *Sporosarcina pasteurii* DSM33, as well as the bacterial strains II_8 and II_{10} calculation, and they were statistically significant at the $p<0.01$ level. The quadratic term of vortex time was also influential in the SOP models for these response calculations, statistically significant at $p<0.01$ or $p<0.05$ level. The linear term of phase separation time (X_3) was influential only for the reference strain and bacteria II_8, statistically significant at the $p<0.05$ level, while the quadratic term was only influential for the reference strain calculations, statistically significant at the $p<0.01$ level. The linear and the quadratic terms of vortex time were statistically significant at $p<0.01$ level in the SOP model, while the linear and the quadratic terms of phase separation time were statistically significant at the $p<0.05$ level in the SOP model for strain III_{11} calculation. The inter-

change term of vortex time and phase separation time ($X_1 \times X_3$) was also influential for bacterial strain III_{11} calculation, statistically significant at $p<0.01$ level. As shown in Table III, for bacterial strain IV_5, the linear and the quadratic terms of phase separation time were statistically significant at $p<0.01$ and $p<0.05$ level in the SOP model.

The coefficients of determination (r^2) for the SOP models were rather good (0.684–0.981, Table III). According to the results presented in Table III, the higher r^2 values were attributed to the SOP models in which the nonlinear terms had less effect and the linear terms were more pronounced. The relatively inaccurate results of the SOP models indicate that some other models would improve the validity of the model predictions.

ANOVA analysis for the experiment in which selected ureolytic bacteria were incubated in nutrient media with urea (Table IV) revealed that the linear term of vortex time considerably influenced the SOP model predictions of the reference strain, as well as strains II_8 and III_{11} calculations, and they were statistically significant at the $p<0.01$ level. The quadratic term of vortex time was also influential in the SOP models for bacterial strains II_8 and III_{11} calculations, statistically significant at the $p<0.01$ or $p<0.05$ level. The quadratic term of phase separation phase was influential for the reference strain calculation, statistically significant at the $p<0.01$ level. The coefficients of determination for the SOP models for nutrient media with urea were relatively good (0.500 – 0.990, Table IV).

TABLE IV. ANOVA calculations for experiments with ureolytic bacteria nutrient media with the addition of 20 % urea (sum of squares is presented); $^+$: statistically significant at $p<0.01$ level; *: $p<0.05$ level; **: $p<0.10$ level

Variable	Degrees of freedom	Sum of squares					
		Reference strain	Wild ureolytic strain				
		S. pasteurii DSM33	II_8	II_{10}	III_{11}	III_{15}	IV_5
X_1	1	**237.420**$^+$	**477.817**$^+$	2.609	**124.093**$^+$	25.227	7.863
X_1^2	1	0.006	**100.226***	10.124	**68.611**$^+$	30.197	0.202
X_2	1	**6.237***	10.555	17.499	1.754	27.761	0.289
X_2^2	1	0.615	11.394	2.104	0.563	0.694	0.424
X_3	1	0.810	40.069**	2.250	0.436	3.725	13.764**
X_3^2	1	**16.409**$^+$	43.943**	2.855	17.715**	0.528	3.458
$X_1 \times X_2$	1	0.123	10.928	24.186	0.053	**239.477**$^+$	0.366
$X_1 \times X_3$	1	2.531**	8.056	0.346	46.529	15.490	1.331
$X_2 \times X_3$	1	1.297	7.506	0.028	0.070	0.055	8.483
Error	5	2.710	49.035	59.914	17.030	52.173	15.448
r^2		0.990	0.929	0.500	0.935	0.861	0.692

In order to present the interactions of the MATH operating parameters and define the recommendation of their value in the MATH protocol for ureolytic bacteria, three-dimensional response (RSM) surface plots were created. All RSM

plots show the interaction of two tested parameters on the cell surface hydrophobicity, while the third parameter was sustained at the central value from the Box–Behnken experimental design. The effect of vortex time and phase separation time on the CSH at a constant volume of hydrocarbon (2.25 mL) is presented in Fig. 2a–f for all tested bacteria incubated in nutrient media without urea, as well as in Fig. 3a–f for all bacteria incubated in nutrient media with urea addition.

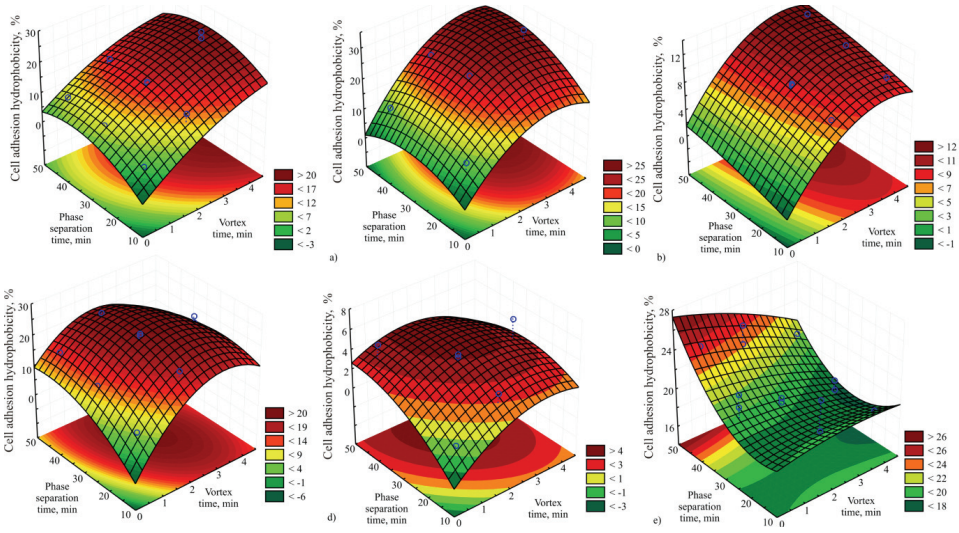

Fig. 2. The effects of the MATH operating parameters on cell surface hydrophobicity using nutrient media without urea: a) *S. pasteurii* DSM33; b) II_8; c) II_{10}; d) III_{11}; e) III_{15}; f) IV_5.

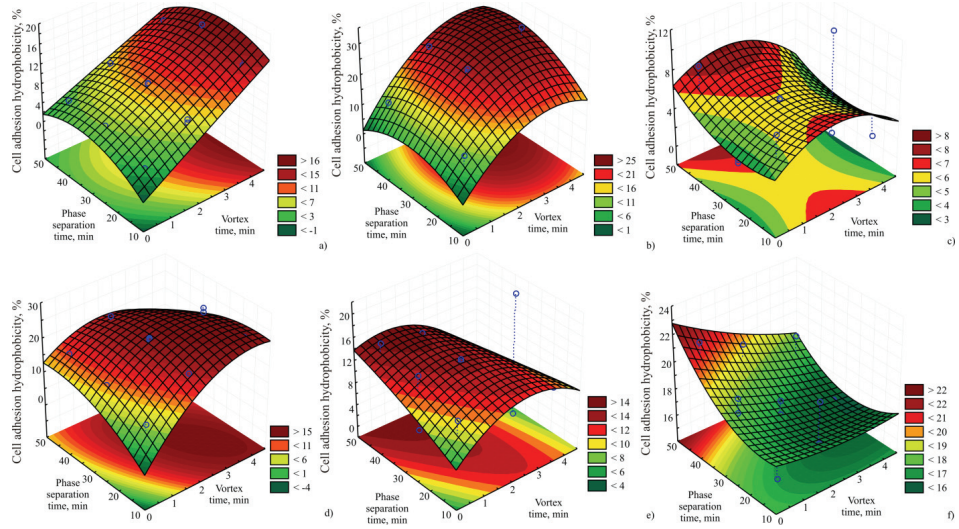

Fig. 3. The effects of the MATH operating parameters on cell surface hydrophobicity using nutrient media with 20 % urea: a) *S. pasteurii* DSM33; b) II_8; c) II_{10}; d) III_{11}; e) III_{15}; f) IV_5.

Based on the obtained results for the referent ureolytic strain (Figs. 2a and 3a), it is evident that the maximum value of CSH (about 20 %) was achieved at the maximum vortex time and at any value of the separation time. A similar effect of vortex and separation time was observed for bacterial strain II_8 (Fig. 2b and 3b). In the case of bacterial strain II_{10} incubated in nutrient media without urea (Fig. 2c), the maximum CSH (about 12 %) was detected at the highest values of both presented parameters. On the other hand, the maximum value of CSH (about 8 %) for the same bacterial strain incubated in the presence of urea, a vortex time of 2 min, and a separation time of 45 min were the most suitable values (Fig. 3c).

According to the results presented in Fig. 2d and 3d, it could be concluded that the maximum CSH of bacterial strain III_{11} is equally achieved at medium values of vortex and separation time (2 and 30 min, respectively) and the maximum values of mentioned parameters (4 and 45 min, respectively).

It could be noticed that the presence of urea in the nutrient media makes differences in the obtained results for all the tested bacteria. Namely, urea has a strong impact on hydrophobic interaction by the transfer of hydrophobes from aqueous solutions to a pure liquid hydrocarbon phase,[29] as well as inducing an immediate metabolic hydrolysis reaction. Due to these details and the fact that urea is an essential nitrogen source for ureolytic bacteria, the presence of urea is required to obtain more representative values of cell surface hydrophobicity.

Standard score analysis (Fig. 4) revealed that the optimal MATH operating parameters for the determination of the CSH of ureolytic bacteria are: a vortex time of 2 min, a hydrocarbon volume of 0.5 mL, and a phase separation time of 15 min for both the tested experiment settings. This treatment was recommended for all tested ureolytic bacteria, with an *SS* value of 0.634 for the nutrient media without urea, and an *SS* value 0.677 for nutrient media with the addition of 20 % urea. The highest value of standard score has bacterial strain IV_5 with values of 0.677 and 0.649 for incubation with and without the addition of urea, respectively. As shown in Table I, this bacterial strain is the most hydrophobic, while II_{10} has the lowest value of CSH.

Comparing the ureolytic bacterial strains from nature with the reference strain *S. pasteurii* DSM 33, three of them (II_8, III_{11} and IV_5) are more hydrophobic, while the cell surface hydrophobicity of the other strains (II_{10} and III_{15}) could be compared that of the referent.

It could be noticed that urea addition decreased the value of the hydrophobicity in almost all experiments, but did not affect change in the MATH operation parameters. Due to this fact, the gained optimized MATH operation parameters (vortex time, hydrocarbon volume, and phase separation time) could be recommended for all ureolytic bacteria. Additionally, using urea in the nutrient media as a nitrogen source, which is required for biotechnological use of ureo-

lytic bacteria, could provide more realistic values of CSH in a real-time process catalyzed by ureolytic bacteria.

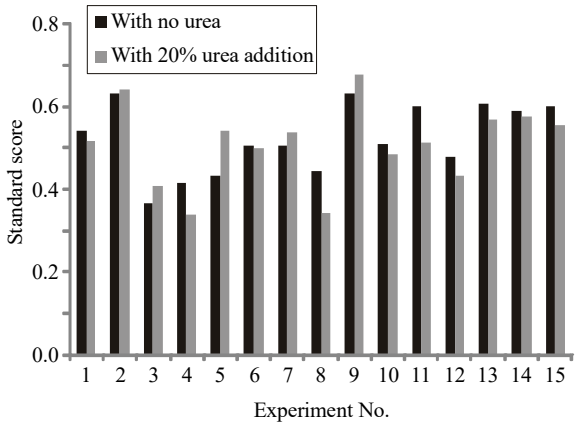

Fig. 4. Standard score analysis for cell adhesion hydrophobicity.

CONCLUSIONS

According to the results obtained in this study, the tested ureolytic bacteria showed hydrophobicity of cell surface in the range to 31.2 % as well as similar behaviour in the case of urea addition in the system. After the optimization process of the MATH test for six different ureolytic bacteria by the Box–Behnken experimental design, three main operating parameters (vortex time, hydrocarbon volume, and phase separation time) were adapted for the universal MATH protocol for ureolytic bacteria. The recommended values of these parameters are 2 min for the vortex time, 0.5 mL of hexadecane as an appropriate hydrocarbon, and 15 min for phase separation time. Despite the lower values of cell surface hydrophobicity of all tested ureolytic strains when urea was present in the system, incubation in nutrient media with urea addition is suggested for use in the MATH test, because this substrate is an essential nitrogen source for application of ureolytic bacteria in bioremediation systems.

Acknowledgment. The financial support of the Ministry of Education, Science, and Technological Development of the Republic of Serbia (Contract No. 451-03-68/2020-14/200134) is gratefully acknowledged.

И З В О Д

ОПТИМИЗАЦИЈА ПРОЦЕСНИХ ПАРАМЕТАРА ТЕСТА ЋЕЛИЈСКЕ ХИДРОФОБНОСТИ ПОВРШИНА ЗА УРЕОЛИТИЧКЕ БАКТЕРИЈЕ

ОЉА Љ. ШОВЉАНСКИ[1], ЛАТО Л. ПЕЗО[2], АНА М. ТОМИЋ[1], АЛЕКСАНДРА С. РАНИТОВИЋ[1], ДРАГОЉУБ Д. ЦВЕТКОВИЋ[1] и СИНИША Л. МАРКОВ[1]

[1]Универзитет у Новом Саду, Технолошки факултет Нови Сад, Лабораторија за микробиологију, Булевар цара Лазара 1, Нови Сад и [2]Универзитет у Београду, Институт за општу и физичку хемију, Студентски трг 12/V, Београд

Хидрофобне интеракције су једне од главних нековалентних веза у биолошким системима, те хидрофобност ћелијских површина представља један од кључних параметара за дефинисање способности биодеградације и понашања бактерија током процеса биоремедијације. С друге стране, улога уреолитичких бактерија у биоремедијацији је довела до испитивања карактеристика ћелијских површина као битног фактора адхезије ове бактеријске групе на абиотичке и биотичке површине и потенцијала стварања биофилма. У циљу оптимизације теста микробиолошке адхезије хидрокарбонатима (microbial adhesion to hydrocarbons test, MATH) за уреолитичку групу бактерија, урађен је Бокс–Бенкенов (Box–Behnken) експериментални дизајн за пет уреолитичких изолата из земљишта и референтни сој *Sporosarcina pasteurii* DSM 33. Оптимизација процесних параметара је урађена за хранљиву подлогу са и без додатка есенцијалног супстрата за циљану метаболичку активност (уреа), са циљем да се упореде разлике у хидрофобности истих уреолитичких сојева. Као оперативни параметри MATH теста, без обзира на присуство урее у систему се препоручују време мешања од 2 min, запремину хидрокарбоната од 0,5 mL и време раздвајања фаза од 15 min. Иако је за све тестиране бактерије доказана хидрофобност ћелијске површине, ниже вредности ове карактеристике у присуству урее за исти бактеријски сој. Овакав резултат може бити објашњен интеракцијом урее са органском фазом у систему за раздвајање и скоро тренутном индукцијом метаболичке реакције хидролизе што се неминовно дешава и у току употребе уреолитичких бактерија у биотехнолошким системима.

(Примљено 13. августа, прихваћено 10. децембра 2020)

REFERENCES

1. C. H. Kang, S. J. Oh, Y. Shin, S. H. Han, I. H. Nam, *Ecol. Eng.* **74** (2016) 402 (https://doi.org/10.1016/j.ecoleng.2014.10.009)
2. D. Arias, L. A. Cisternas, C. Miranda, M. Rivas, *Front. Bioeng. Biotechnol.* **6** (2018) 209 (https://doi.org/10.3389/fbioe.2018.00209)
3. S. Bibi, M. Oualha, M. Y. Ashfa, M. T. Suleiman, N. Zouari, *RSC Adv.* **8** (2018) 5854 (https://doi.org/10.1039/C7RA12758H)
4. R. Siddique, R. N. K. Chahal, *Constr. Build. Mater.* 25 (2011) 3791 (https://doi.org/10.1016/j.conbuildmat.2011.04.010)
5. H. Min Son, H. Y. Kim, S. M. Park, H. K. Lee, *Mater.* **11** (2018) 782 (https://doi.org/10.3390/ma11050782)
6. H. Pang, G. Wang, H. Yang, H. Wu, X. Wang, Y. Chen, *IOP Conf. Ser.: Earth Environ. Sci.* **252** (2019) 052131 (https://doi.org/10.1088/1755-1315/252/5/052131)
7. J. M. van der Bergh, B. Miljevic, O. Šovljanski, S. Vučetić, S. Markov, J. Ranogajec, A. Bras, *Constr. Buil. Mater.* 248 (2020) 118557 (https://doi.org/10.1016/j.conbuildmat.2020.118557)
8. A. Krasowska, K. Sigler, *Front Cell Infect. Microbiol.* **4** (2014) 112 (https://doi.org/10.3389/fcimb.2014.00112)

9. A. Vidaković, *Denitrifier PhD Thesis*, University of Novi Sad, Novi Sad, 2019 (in Serbian)
10. C. O. Obuekwe, Z. K. Al-Jadi, E. Al-Saleh, *FEMS Microbiol. Lett.* **270** (2009) 214 (https://doi.org/10.1111/j.1574-6968.2007.00685.x)
11. G. Saini, *PhD Thesis*, Oregon State University, Corvallis, OR, 2010
12. L. Hall-Stoodley, J. W. Costerton, P. Stoodle, *Nat. Rev. Microbiol.* **2** (2004) 95 (https://doi.org/10.1038/nrmicro821)
13. Z. A. Mirani, A. Fatima, S. Urooj, M. Aziz, M. N. Khan, T. Abbas, *Iran. J. Basic. Med. Sci.* **21**(2018) 760 (https://doi.org/10.22038/IJBMS.2018.28525.6917)
14. C. H. Bolster, S. L. Walker, K. L. Cook, *J. Environ. Qual.* **35** (2006) 1018 (https://doi.org/10.2134/jeq2005.0224)
15. P. Tribedi, A. K. Sil, *J. App. Microbiol.* **116** (2013) 295 (https://doi.org/10.1111/jam.12375)
16. P. Lather, A. K. Mohanty, P. Jha, A. K. Garsa, *Biochem. Res. Intern.* **60** (2016) 1091290 https://doi.org/10.1155/2016/1091290
17. Y. N. Sardessai, S. Bhosle, *Biotechnol. Prog.* **20** (2008) 655 (https://doi.org/10.1021/bp0200595)
18. K. Hori, H. Watanabe, S. I. Ishii, Y. Tanji, H. Unno, *Appl. Environ. Microbiol.* **74** (2008) 2511 (https://doi.org/10.1128/AEM.02229-07)
19. S. Torres, A. Pandey, G. R. Castro, *Biotech. Adv.* **29** (2011) 442 (https://doi.org/10.1016/j.biotechadv.2011.04.002)
20. M. H. Ly, M. Aguedo, S. Goudot, M. L. Le, P. Cayot, J. A. Teixeira, T. M. Le, J. M. Belin, Y. Wache, *Food Hydrocolloids* **22** (2008) 742 (https://doi.org/10.1016/j.foodhyd.2007.03.001)
21. F. Gaboriaud, E. Dague, S. Bailet, F. Jorand, J. Duval, F. Thomas, *Colloids Surf., B* **52** (2006) 108 (https://doi.org/10.1016/j.colsurfb.2006.04.017)
22. C. O. Obuekwe, Z. K. Al-Jadi, E. S. Al-Saleh, *Can. J. Microbiol.* **53** (2007) 252 (https://doi.org/10.1111/j.1365-2672.2008.03887.x)
23. C.R. Bunt, D.S. Jones, I.G. Tucker, I.G., *Int. J. Pharm.* **113** (1995) 257 (https://doi.org/10.1016/0378-5173(94)00205-J)
24. B. M. Hsu, C. Huang, *Colloids Surf.* **201** (2002) 201 (https://doi.org/10.1016/S0927-7757(01)01009-3)
25. S. L. Walker, J. E. Hill, J. A. Redman, M. Elimelech, *Appl. Environ. Microbiol.* **71** (2005) 3093 (https://doi.org/10.1128/AEM.71.6.3093-3099.2005)
26. K. Myszka, K. Czaczyk, *Pol. J. Food. Nutr. Sci.* **61** (2007) 173 (http://dx.doi.org/10.2478/v10222-011-0018-4)
27. O. Šovljanski, A. Tomić, L. Pezo, S. Markov, *J. Sci. Food Agric.* **100** (2020) 1155 (https://doi.org/10.1002/jsfa.10124)
28. R. L. Prior, X. Wu, K. Shaish, *J. Agric. Food Chem.* **53** (2005) 4290 (https://doi.org/10.1021/jf0502698)
29. T. A. Shpiruk, M. Khajehpour, *Phys. Chem. Phys.* **15** (2013) 213 (https://doi.org/10.1039/C2CP42759A).